

Polyanion-type electrode materials for advanced sodium-ion batteries

L.N. Zhao ^{a, b, c, 1}, T. Zhang ^{a, c, 1}, H.L. Zhao ^{d, **}, Y.L. Hou ^{a, b, c, *}

^a Department of Materials Science and Engineering, College of Engineering, Peking University, Beijing 100871, China

^b Beijing Innovation Centre for Engineering Science and Advanced Technology (BIC-ESAT), China

^c Beijing Key Laboratory for Magnetoelectric Materials and Devices (BKLMMD), China

^d School of Materials Science and Engineering, University of Science and Technology Beijing, Beijing 100083, China



ARTICLE INFO

Article history:

Received 15 November 2019

Received in revised form

27 December 2019

Accepted 8 January 2020

Available online 17 January 2020

Keywords:

Sodium-ion batteries

Polyanion

NASICON

Cathode materials

Anode materials

ABSTRACT

Electrical energy storage (EES) exploiting secondary battery technologies is ideal for large-scale energy storage needs due to the rapid growth in proliferation of renewable energy sources and the emerging markets of grid-scale battery applications. Sodium-ion batteries (SIBs), a more sustainable EES option alternative to lithium-ion batteries (LIBs), have attracted intensive interests over the past decade, because of the natural abundance, evenly geographical-distributed Na-source, significantly low cost, and environmental benignity. Polyanionic compounds offer an appealing combination of rich structural diversity, superior ionic conductivity, high structural and thermal stability, and convenient storage/handling, making them competitive and attractive candidate electrode materials for next generation energy storage systems. In this review, recent advancements made regarding polyanion-type electrodes used for SIBs are summarized, elaborating their intrinsic structural characteristics, electrochemical properties, and corresponding sodium-storage mechanisms. Furthermore, we highlight the recent achievements in the lab-scale Na-ion full-cell prototypes that consist of polyanion-type compounds as one or both working electrodes. Last but not least, challenges and outlooks on further optimization of the structure and the electrochemical performance of polyanion-type electrode materials for SIBs are also presented to provide some insights to facilitate the practical realization of sodium-ion technologies.

© 2020 Elsevier Ltd. All rights reserved.

1. Introduction

Due to the economic and environmental vulnerability of fossil fuels combustion, effectively exploiting renewable, sustainable, and clean energy sources becomes especially urgent to address the worldwide shortage of resources and global warming concerns. In order to curb the renewable energy sources intermittency and obtain stable and continuous generation of electricity for power grid operations, developing performance- and cost-effective energy storage systems is of the prime necessity [1]. In the past decades, electrical energy storage (EES) exploiting secondary battery technologies revealed to be one of the most feasible options because of their high energy round-trip efficiency, versatile power, and suitable energy characteristics to meet various grid functions and scalable productions [2,3]. Particularly, successful

commercialization of lithium-ion batteries (LIBs) in 1990 is a great milestone, which not only catalyzes unprecedented applications of electronics information industry, but also offers new opportunities for better integration and penetration of renewable energy sources [4]. Intrinsic flexibility of battery storage technologies coupled to renewable electricity sources will usher in revolution of our electric infrastructure systems, even the entire ecology-economy model of modern civilization [5]. It is called Smart Grid (Fig. 1), which works as an enabling engine to transform the current energy industry into a new era of reliability, availability, and efficiency that will contribute to our economic and environmental health [6].

Apparently, the ultimate success of the Smart Grid is inseparable from the effectiveness of large-scale energy storage. Nowadays, LIBs are ubiquitous in the sector of small-scale consumer electronics and gradually increasing the market share in battery electric vehicles. LIBs have the ability to respond quickly to match the rapid growth in renewable energy sources, due to the high energy density and stable cycling properties of the already commercialized designs and the potentials of different shapes and sizes. Yet, facing the steep price rise and resource constraints from the scarcity and non-

* Corresponding author.

** Corresponding author.

E-mail addresses: hlzhao@ustb.edu.cn (H.L. Zhao), hou@pku.edu.cn (Y.L. Hou).

¹ These authors contributed equally to this work.

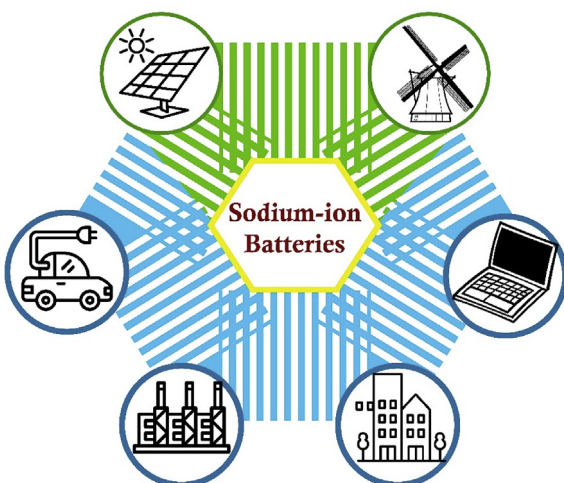


Fig. 1. Schematic illustration of the Smart Grid.

uniform distribution of lithium resource, LIBs are believed to be not the best choice for stationary, large-scale EES applications and, in addition, there are growing concerns on adverse ecological hazards upon disposal of toxic elements [7]. The challenges and demands outlined above have motivated the researchers to pursue various alternative battery chemistries (termed as “post-LIBs”), featuring as low cost, widespread availability, and environmentally friendly, to replace LIBs especially in applications unrestricted by high gravimetric and/or volumetric energy density [8].

Given the abundance of sodium-based resources and the similar performance characteristics with LIBs, room-temperature sodium-ion batteries (SIBs) hold great promise to meet large-scale EES demands [9,10]. Comparing with Li, however, the large ionic size of Na (1.02 Å vs. 0.76 Å) and its low standard electrochemical potential vs. SHE (~2.71 V vs. Na⁺/Na and 3.04 V vs. Li⁺/Li) as a consequence of sluggish redox kinetics, huge volume variations, and low redox potentials resulted in less favorable power and energy densities of SIBs and thus limiting their further applications for grid-scale energy storage [11–13]. Tremendous efforts have been geared to explore suitable electrode materials for SIBs to match the performance and characteristics of modern LIBs [14–18].

A large variety of compounds have been unveiled with considerable sodium-storage capacities for SIBs. Layered metal oxides [19–23], polyanion compounds [21,24,25], and metal hexacyanometalates [26–30] have been extensively investigated as cathode materials, whereas hard carbon [31–34], metal alloys [35–38], and transition-metal chalcogenides [39–42] have been studied as anode materials. However, most of them suffer from poor cycling performance owing to the structural instability during Na-ions insertion/extraction processes. For example, layered transition-metal oxides possess high theoretical capacity, but undergo very complicated multiphase transitions during Na-(de) intercalation reactions, leading to rapid structural degradation of the host materials [43,44]. In addition, Prussian blue analogues synthesized by a conventional coprecipitation method always contain a certain amount of lattice defects and coordinate water, resulting in a huge loss of active sites and causing a severe problem with electrolyte [45,46]. In the case of anode materials, huge volumetric change, such as 400%–490% volume expansion from Sn or P reacting with Na to form Na_{3.75}Sn or Na₃P, results in the pulverization of the active materials and rapid deteriorations of cycling performances [47–49].

This problem can be circumvented by implementing polyanion-type electrode materials with open framework providing pronounced structural stability. Polyanionic compounds have become in the last two decades the subject of very attractive research since the discovery of electrochemically active LiFePO₄ [16,21,75]. Polyanionic framework materials possess versatile and adjustable structures, built on polyanionic groups [(XO₄)_mⁿ⁻: X = B, C, S, P, Si, As, Mo, W, V, or Ti, etc.] strongly covalent-bonded with [(MO_x)ⁿ⁻: M = transition-metal] [76]. The “mixed-polyanionic units” can also be realized by designing the joint with other anions, such as [Y⁻, e.g. F⁻, OH⁻, O²⁻, N³⁻, etc.] [X₂O_m: e.g. PO₄–P₂O₇, SO₄–S₂O₃, etc.], and [(XO₄)_mⁿ⁻, e.g. PO₄–CO₃, PO₄–SO₄, PO₄–NO₃, etc.] [14,77]. Fig. 2 shows the crystal structures of the representative polyanionic compounds, and the corresponding crystal structural parameters are summarized in Table 1. Polyanion-type electrode materials are particularly attractive and widely considered as futuristic Na-host electrodes due to the following considerations: (1) robust covalent-bonded framework provides high structural and thermal stability, essential for extensive cycling life and safety issues. (2) A large interstitial space generated from the open network structure of interconnected conduction pathways leads to fast ionic conduction and low volumetric expansion during Na-ions sodiation/desodiation processes. (3) Rich structural diversity allows the monitoring of the given Mⁿ⁺/M⁽ⁿ⁻¹⁾⁺ redox couples and achieves higher values of redox potentials than that of layer oxides through the inductive effects introduced by Goodenough [78]. However, the “weight penalty” from the presence of polyanion units and no direct M–OM– electronic delocalization result in quite poor intrinsic electronic conductivity in this class of material. To compact this issue, coating with various conductive materials, constructing special micro/nano structures, as well as lattice doping are effective strategies to achieve high electrochemical performance of polyanion-type electrode materials.

In this review, the recent research progress and prospective future in the broad class of polyanion-type electrode materials for SIBs are summarized. A detailed account of various sodium-based polyanionic compounds is given, focusing especially on intrinsic structural features, sodium-storage mechanisms, and electrochemical performance. We highlight the descriptions of the most promising sodium-ion full-cells proposed so far on the use of polyanion-type electrodes and the various architectures and strategies to enhance the electrochemical performances with regard to full-cell characteristics and electrochemistry considerations. In addition, some of the practical challenges and future prospects toward the commercialization of polyanion-type compounds for SIBs are also included. The polyanion-type compounds are proposed to be potential systems for large-scale energy storage applications.

2. Structures and sodium-storage mechanisms

2.1. Polyanion compounds as cathode materials

2.1.1. Olivine and maricite NaFePO₄

Because olivine-type LiFePO₄ gains great commercial success in LIBs owing to its low cost and high energy density, the sodium counterpart, NaFePO₄, is one of the earliest and most widely studied polyanionic compounds as cathode material for SIBs. Two main types of structures of NaFePO₄, olivine and maricite, have thus far been reported to be Na insertion hosts for rechargeable batteries.

Olivine NaFePO₄ (Fig. 2a) crystallizes into an orthorhombic structure (space group of *Pnma*), in which the Na and Fe atoms occupy half of the octahedral sites, while the P atoms are confined into the one-eighth of the tetrahedral sites in a distorted

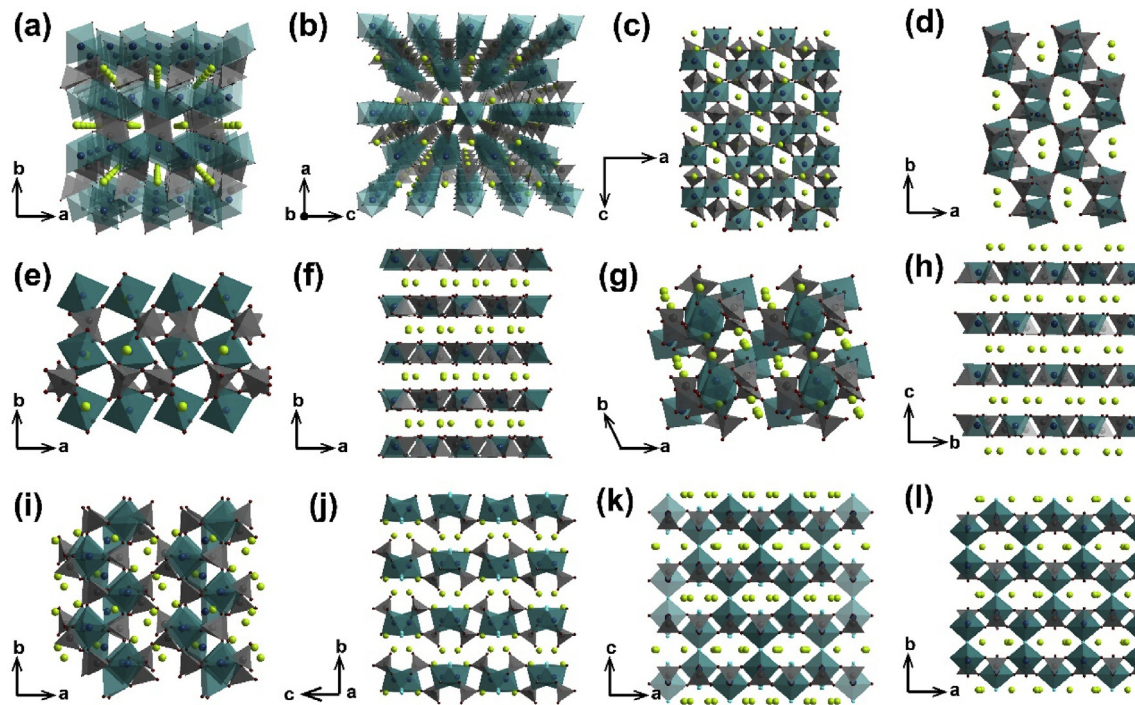


Fig. 2. Crystal structure of representative polyanion-type compounds: (a) NaFePO₄-olivine, (b) NaFePO₄-maricite, (c) NASICON-type Na₃V₂(PO₄)₃, (d) NaFeP₂O₇-I, (e) NaFeP₂O₇-II, (f) Na₂CoP₂O₇-I, (g) Na₂CoP₂O₇-II, (h) Na₂CoP₂O₇-III, (i) Na₄Fe₃(PO₄)₂P₂O₇, (j) Na₂FePO₄F, (k) Na₃V₂(PO₄)₂F₃, and (l) Na₃V₂(PO₄)₂O₂F.

Table 1
Lattice parameters of representative polyanion-type electrode materials for Na-ion batteries.

Materials	Structure	a/Å	b/Å	c/Å	Vol/Å ³	Ref.
NaFePO ₄	Orthorhombic/Pnma	10.406	6.218	4.946	320.14	[50]
NaFePO ₄	Orthorhombic/Pnma	8.990	6.862	5.047	311.3	[51]
Na ₃ V ₂ (PO ₄) ₃	Rhombohedral/R $\bar{3}$ c	8.7288	8.7288	21.8042	1438.73	[52]
NaFeP ₂ O ₇	Monoclinic/P2 ₁ /c	7.324	7.904	9.574	514.5	[53]
NaFeP ₂ O ₇	Monoclinic/P2 ₁ /c	7.298	7.874	9.536	508.62	[54]
NaTiP ₂ O ₇	Monoclinic/P2 ₁ /c	8.697	5.239	13.293	541.85	[55]
NaTiP ₂ O ₇	Monoclinic/P2 ₁ /c	7.394	7.936	9.726	529.71	[55]
NaVP ₂ O ₇	Monoclinic/P2 ₁ /c	7.324	7.930	9.586	516.35	[56]
Na ₂ CoP ₂ O ₇	Orthorhombic/P2 ₁ /c	7.713	10.271	15.378	1218.25	[57]
Na ₂ CoP ₂ O ₇	Triclinic/P $\bar{1}$	9.735	10.940	12.289	566.81	[57]
Na ₂ CoP ₂ O ₇	Tetragonal/P42/mmm	7.706	7.706	10.301	611.66	[58]
Na ₂ FeP ₂ O ₇	Triclinic/P $\bar{1}$	6.4338	9.4158	11.0180	574.16	[59]
Na ₂ MnP ₂ O ₇	Triclinic/P $\bar{1}$	5.316	6.580	9.409	290.98	[60]
Na ₂ CuP ₂ O ₇	Monoclinic/C2/c	14.715	5.704	8.066	612.88	[61]
Na ₂ CuP ₂ O ₇	Monoclinic/P2 ₁ /n	8.823	13.494	5.108	607.44	[62]
Na ₂ ZnP ₂ O ₇	Tetragonal/P42/mmm	7.656	7.656	10.233	599.80	[63]
Na ₂ VOP ₂ O ₇	Monoclinic/P2 ₁ /c	7.718	13.323	6.287	637.62	[64]
Na ₂ VOP ₂ O ₇	Tetragonal/P4mb	8.108	8.108	4.943	324.95	[65]
Na ₄ Fe ₃ (PO ₄) ₂ P ₂ O ₇	Orthorhombic/Pn2 ₁ a	18.075	6.532	10.647	1257.204	[66]
Na ₄ Co ₃ (PO ₄) ₂ P ₂ O ₇	Orthorhombic/Pn2 ₁ a	18.046	6.533	10.536	1242.1	[67]
Na ₄ Mn ₃ (PO ₄) ₂ P ₂ O ₇	Orthorhombic/Pn2 ₁ a	17.991	6.648	10.765	1287.6	[68]
Na ₄ Ni ₃ (PO ₄) ₂ P ₂ O ₇	Orthorhombic/Pn2 ₁ a	17.999	6.4986	10.4200	1218.9	[68]
Na ₂ VPO ₄ F	Tetragonal/I4/mmm	6.387	6.387	10.734	—	[69]
Na ₂ FePO ₄ F	Orthorhombic/Pbcn	5.2810	14.0417	11.9542	886.45	[70]
Na ₃ V ₂ (PO ₄) ₂ F ₃	Tetragonal/P4 ₂ /mnm	9.047	9.047	10.705	876.2	[71]
Na ₃ V ₂ (PO ₄) ₂ O ₂ F	Tetragonal/I4/mmm	6.3702	6.3702	10.6365	431.63	[72]
Na ₃ V ₂ (PO ₄) ₂ O ₂ F	Tetragonal/P4 ₂ /mnm	9.0305	9.0305	10.6200	—	[73]
NaTi ₂ (PO ₄) ₃	Trigonal/R $\bar{3}$ c	8.48	8.48	21.77	1355.75	[74]

hexagonal-close-packed oxygen lattice [79,80]. Due to the different sizes of ionic radii and the charges between Na and Fe cations, two crystallographically distinct octahedral sites (FeO₆ octahedra and NaO₆ octahedra) locate in the olivine NaFePO₄ phase. The FeO₆ units, linked to each other by corner sharing, form linear 1D zigzag chains parallel to the c-axis, while the NaO₆ octahedra are ordered

as linear chains along the [010] direction through edge sharing. Phosphate ions, PO₄ tetrahedra, share one edge and four corners with each FeO₆ octahedra, constructing the main framework structure of olivine-type NaFePO₄. In the olivine NaFePO₄ phase, the edge-shared NaO₆ octahedra provide one-dimensional (1D) sodium-ion migration channels along the b-axis with a low

diffusion barrier. The energy of $\text{Fe}^{3+}/\text{Fe}^{2+}$ redox couple can be relatively stabilized by the polyanionic framework structure through the inductive effect, leading to a decent voltage plateau (~ 2.8 V vs. Na^+/Na) and high theoretical capacity (154 mAh g^{-1}) of iron-based cathode materials based on the $\text{Fe}^{3+}/\text{Fe}^{2+}$ redox couple [81].

Unlike LiFePO_4 , the olivine-type NaFePO_4 is the metastable polymorph of NaFePO_4 that undergoes irreversible phase transition to form a thermodynamically stable maricite phase over 480°C [86]. Therefore, conventional solid-phase transition reactions under high temperature are no longer suitable for the synthesis of olivine-type NaFePO_4 , which is commonly obtained by chemical/electrochemical ion-exchange from olivine-type LiFePO_4 [86–88]. Approximately one mole of Na^+ ions are involved in the reversible redox reaction process in olivine-type NaFePO_4 based on the $\text{Fe}^{3+}/\text{Fe}^{2+}$ redox couple. Oh et al. firstly studied the electrochemical performance of the olivine-type NaFePO_4 material prepared through electrochemical Li–Na ion-exchange strategy, which delivered a high reversible capacity of 125 mAh g^{-1} and an average potential of ≈ 2.8 V vs. Na/Na^+ , indicating a promising candidate as an electrode material for large-scale energy storage applications [89]. Because of a large volumetric mismatch between the two end phases of NaFePO_4 and FePO_4 (difference in unit volume of 17.58%), a stage transformation process happens to buffer the mechanical strain. The olivine- NaFePO_4 electrode was often characterized by two separate charge plateaus by a voltage drop and one discharge plateau (Fig. 3a). The asymmetric Na ion insertion/deinsertion into/from the olivine NaFePO_4 electrode was reported under different mechanisms. Moreau and Casas-Cabanas et al. revealed the

existence of a stable intermediate phase with the composition of $\text{Na}_{2/3}\text{FePO}_4$ (a sodium ion ordered phase) during the sodium-ion intercalation/deintercalation process [50,81,90,91]. Olivine-type NaFePO_4 transformed into the intermediate $\text{Na}_{2/3}\text{FePO}_4$ phase through a solid solution domain, which followed subsequently a two-phase transformation reaction process to form olivine- FePO_4 . The presence of a $\text{Na}_{2/3}\text{FePO}_4$ intermediate phase during the Na ion deintercalation process was first observed by Cao's group through conventional electrochemical techniques, corroborating an identical two-step phase transition reaction both upon sodium insertion and extraction processes (Fig. 3b) [82]. Yamada and co-workers determined the composition-temperature phase diagram of olivine Na_xFePO_4 ($0 < x < 1$) through Mössbauer spectroscopy and high-temperature *in situ* X-ray diffraction [83]. In the range of $0 < x < 2/3$, Na_xFePO_4 was found to be in a two-phase region, while Na_xFePO_4 ($2/3 < x < 1$) was in the solid-solution phase. The intermediate phase $\text{Na}_{2/3}\text{FePO}_4$ exists to buffer the large volume expansion during the redox reaction (Fig. 3c). A detailed combined density functional theory (DFT) calculations and high-resolution synchrotron X-ray diffraction study has allowed elucidation of the co-existence of two intermediate structures with compositions of $\text{Na}_{2/3}\text{FePO}_4$ and $\text{Na}_{5/6}\text{FePO}_4$ [92]. Sodium ordering and electron mobility as well as the variation of local magnetic environments in olivine-type NaFePO_4 have also been investigated (Fig. 3d) [84,93,94].

In contrast, the thermodynamically favored maricite- NaFePO_4 is usually regarded as electrochemically inactive due to the blocked ionic pathways. In the maricite- NaFePO_4 lattice, as shown in Figs. 2b and 1D, chain structures built up by edge-shared FeO_6

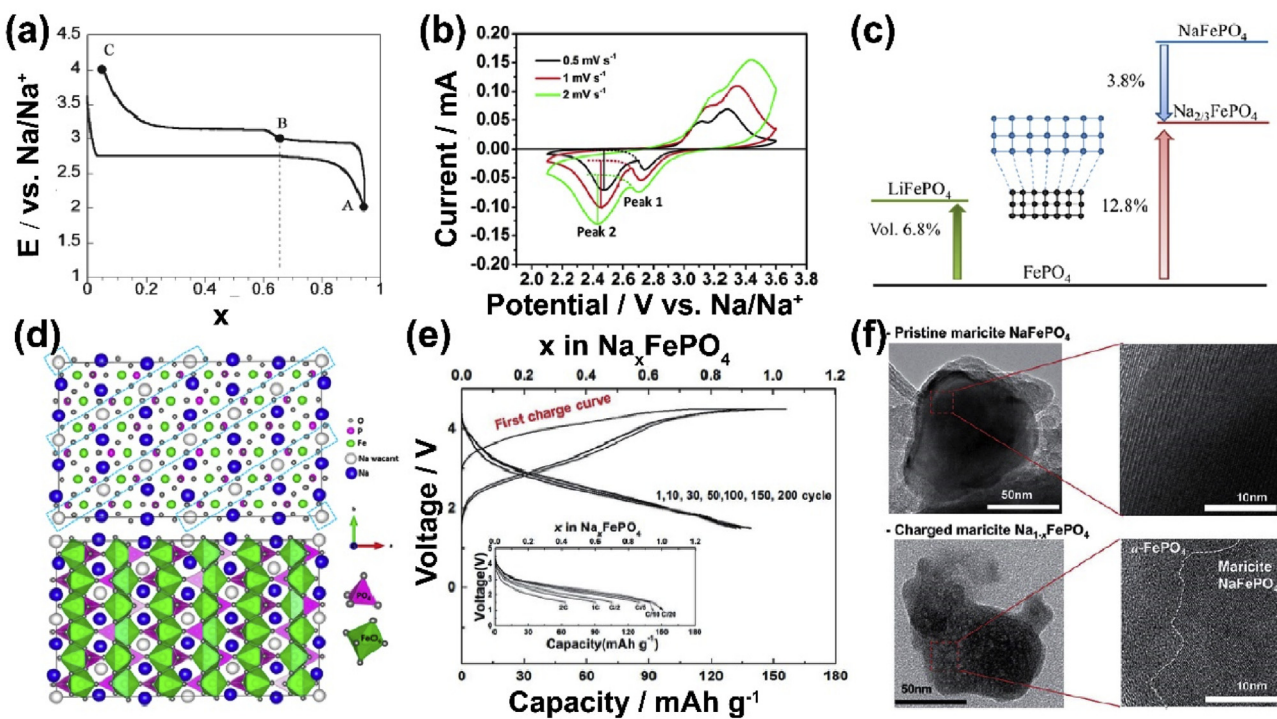


Fig. 3. (a) Typical charge and discharge profiles of the olivine-type NaFePO_4 electrode. Reproduced with permission [50]. Copyright 2010, American Chemical Society. (b) Cyclic voltammogram (CV) curves of olivine-type NaFePO_4/C electrode within the voltage range of 2.0–3.8 V at different scan rates of 0.5, 1, and 2 mV s^{-1} . Reproduced with permission [82]. Copyright 2015, American Chemical Society. (c) Schematic illustration of the comparison of the volume expansion of FePO_4 upon Li^+ and Na^+ insertion. A stable intermediate phase with the composition of $\text{Na}_{2/3}\text{FePO}_4$ to buffer the large volume expansion is found in the sodium intercalation process, which is not generally found for Li_xFePO_4 . Reproduced with permission [83]. Copyright 2013, American Chemical Society. (d) Schematic illustration of the refined crystal structure with Na^+ vacancies and polyhedral representation. Reproduced with permission [84]. Copyright 2014, American Chemical Society. (e) Galvanostatic charge–discharge profiles of the maricite- NaFePO_4 electrode vs. cycle number at 0.05 C for SIBs, inset: discharge curves as a function of the C rate from 0.05 C to 3 C. (f) TEM observations of pristine maricite- NaFePO_4 with comparison of partially charged maricite- $\text{Na}_{1-x}\text{FePO}_4$. Maricite- FePO_4 simultaneously transforming into amorphous FePO_4 through a two-phase reaction is confirmed. Reproduced with permission [85]. Copyright 2015, American Chemical Society.

octahedra are abridged to PO_4 tetrahedra by a corner-sharing manner. Sodium cations, occupying the large tetrahedral sites, are thus isolated by PO_4 tetrahedra throughout the lattice, resulting in a “closed” framework with limited transmission channels for the Na^+ diffusion. Until 2015, Kang et al. reported the pioneering discovery that maricite-type NaFePO_4 can function as the cathode material for SIBs [85]. Quantum mechanics calculations combined with electrochemical experiments revealed all Na ions can be extracted from nanosized maricite- NaFePO_4 , delivering a capacity of 142 mAh g⁻¹ at 0.05 C and good cycling stability (Fig. 3e). The analyses of X-ray diffraction (XRD) and extended X-ray absorption fine structure (EXAFS) showed that the first desodiation for maricite- NaFePO_4 induced the maricite- FePO_4 transformed into amorphous FePO_4 , which significantly enhanced Na mobility in the transformed phase with small hopping activation barrier (Fig. 3f). The understanding of the underlying reaction mechanism and the outstanding electrochemical performance have raised great interests of particle nanosizing engineering of maricite- NaFePO_4 and researching on amorphous NaFePO_4 [95–103].

2.1.2. NASICON $\text{Na}_3\text{V}_2(\text{PO}_4)_3$

NASICON (Na^+ -Super-Ionic-Conductor) structure was first identified from the typical solid electrolyte $\text{Na}_{1+x}\text{Zr}_2\text{P}_{3-x}\text{Si}_x\text{O}_{12}$ ($0 \leq x \leq 3$) material used for high temperature Na-S batteries [78,104]. Indebted to the pioneering work of Delmas and co-workers in 1988 [105], NASICON-based materials have been intensively investigated as ideal insertion hosts for alkali ions owing to the pronounced structural stability and the fast-ionic conductivity. $\text{Na}_3\text{V}_2(\text{PO}_4)_3$, as the most representative compound of this family, is widely considered to be a promising cathode candidate for SIBs. The thermodynamically stable phase of $\text{Na}_3\text{V}_2(\text{PO}_4)_3$ is a rhombohedral structure with a space group of $R\bar{3}c$ [106], which is different to the monoclinic phase of its lithium counterpart $\text{Li}_3\text{V}_2(\text{PO}_4)_3$ [107]. In the $\text{Na}_3\text{V}_2(\text{PO}_4)_3$ framework, each VO_6 octahedra share corners with three PO_4 tetrahedra to establish a “lantern” structural unit of $[\text{V}_2(\text{PO}_4)_3]^{3-}$ polyanion (Fig. 2c). All the lantern units align into $[\text{V}_2(\text{PO}_4)_3]_\infty$ ribbons along the c -axis and the neighboring $[\text{V}_2(\text{PO}_4)_3]_\infty$ ribbons are interconnected by PO_4 tetrahedra along the a -axis, creating a three-dimensional (3D) open covalent framework with large interstitial space facilitating sodium ion transport. It should be noted that there are two kinds of crystallographic sites to accommodate sodium ions in the $\text{Na}_3\text{V}_2(\text{PO}_4)_3$ framework, namely Na(1) sites with Wyckoff position 6b and Na(2) sites with Wyckoff position 18e, according to two different oxygen environments. Na(1) ions possess six-fold oxygen coordination and are located between two adjacent $[\text{V}_2(\text{PO}_4)_3]$ units in the c -axis direction, while the Na(2) ions have eight-fold coordination and are situated between two PO_4 tetrahedrons with the same c -ordinate level as P atoms. The corresponding occupations of the Na(1) and Na(2) sites are 1 and 2/3, respectively, implying that numerous vacancies lie in this NASICON framework offering facile channels for sodium ions diffusion.

Electrochemical properties of NASICON $\text{Na}_3\text{V}_2(\text{PO}_4)_3$ were firstly investigated by Uebou et al. in 2002 [113]. As the cathode material for SIBs, $\text{Na}_3\text{V}_2(\text{PO}_4)_3$ exhibits a flat operation potential of 3.4 V vs. Na^+/Na (Fig. 4a) and a high theoretical capacity of 117.6 mAh g⁻¹ (gravimetric energy density of 401 Wh kg⁻¹). Two Na cations can be reversibly inserted/extracted into/from $\text{Na}_3\text{V}_2(\text{PO}_4)_3$ based on the $\text{V}^{3+}/\text{V}^{4+}$ redox couple [114]. The sodium storage mechanism and structural evolution of the $\text{Na}_3\text{V}_2(\text{PO}_4)_3$ electrode were investigated by in-situ XRD (Fig. 4b) and spherical-aberration-corrected annular-bright-field scanning transmission electron microscopy (ABF-STEM) (Fig. 4c), whose results revealed a typical two-phase transition reaction from the $\text{Na}_3\text{V}_2(\text{PO}_4)_3$ phase to the $\text{NaV}_2(\text{PO}_4)_3$ phase with a small volume variation of 8.26% [109,110]. During the

electrochemical reaction process, only Na ions located at Na(2) sites can be reversibly extracted whereas Na(1) ions are immobile due to the relatively weaker Na(2)-O bonding. The sodium-ion migration pathways were carefully examined by first-principles calculations [111,115]. By evaluating the activation energies for possible mechanisms toward $\text{Na}_3\text{V}_2(\text{PO}_4)_3$, two pathways along x and y directions and one possible curved route were proposed for ion diffusion, confirming the 3D transport characteristics of NASICON $\text{NaV}_2(\text{PO}_4)_3$ (Fig. 4d) [111]. As shown in Fig. 4e, Ohno et al. introduced for the first time a polaron–Na vacancy complex model using the hybrid density function Heyd–Scuseria–Ernzerhof (HSE06) method, revealing the intra-layer pathway from Na(1) sites to Na(2) sites passing through the hexagonal bottleneck composed of VO_6 octahedra and PO_4 tetrahedra is preferred due to the lower migration barrier energy [112].

2.1.3. Pyrophosphates

Inspired by the success of lithium iron(II) pyrophosphate ($\text{Li}_2\text{FeP}_2\text{O}_7$) as a cathode material for LIBs [116,117], Na-based pyrophosphates arose as attractive intercalation hosts for SIBs over the last few years [118]. The most studied pyrophosphates contain single-sodium metal pyrophosphates NaMP_2O_7 ($M = \text{Fe}, \text{V}, \text{Ti}$) [55,56,119–121], two-sodium metal pyrophosphates $\text{Na}_2\text{MP}_2\text{O}_7$ ($M = \text{Fe}, \text{Co}, \text{Mn}$) [58,122–125], and the mixed pyrophosphates $\text{Na}_4\text{M}_3(\text{PO}_4)_2\text{P}_2\text{O}_7$ ($M = \text{Fe}, \text{Co}, \text{Mn}, \text{Ni}$) [66,126–129]. Pyrophosphates, easily obtained from the thermal decomposition of phosphates with oxygen evolution, show thermodynamical stability by far exceeding those of the layered oxides and being comparable to those of other polyanion compounds [14]. The high intrinsic stability is benefited from the stable pyrophosphate $\text{P}_2\text{O}_7^{4-}$ anions, representing an added value to safety for large-scale economic SIB applications.

2.1.3.1. Single-sodium metal pyrophosphates NaMP_2O_7 ($M = \text{Fe}, \text{V}, \text{Ti}$)

The study of Na-based pyrophosphate systems started with the unveiling of the single-sodium metal pyrophosphate NaFeP_2O_7 as early as 1982 [119]. NaFeP_2O_7 crystallizes as monoclinic crystals with the $P2_1/c$ space group, which can be categorized into two different types of crystal structures due to the irreversible phase transition at different temperatures: I-type and II-type. The crystal structure of NaFeP_2O_7 -I was identified as isostructural to KAlP_2O_7 , firstly reported by Calvo et al. [130]. In the NaFeP_2O_7 -I host framework (Fig. 2d), the $\text{P}_2\text{O}_7^{4-}$ polyanion, consisting of a pair of corner-sharing PO_4 tetrahedra in a nearly staggered configuration, is propagated parallel to the ab plane by the two-fold screw axes. Each FeO_6 octahedra corner shares oxygen atoms contributed from three layers of the $\text{P}_2\text{O}_7^{4-}$ group, forming the basic network for the entire structure. It makes an open 1D channel along the c -axis direction for Na^+ migration, hence offering possibility for applications as an insertion-type electrode material. Moreover, NaFeP_2O_7 -I, the thermodynamically unstable phase, undergoes an irreversible phase transition into its polymorph NaFeP_2O_7 -II when the temperature is above 750 °C. Its crystal structure is closely related to the I-type structure with distorted hcp oxygen lattice (Fig. 2e). NaFeP_2O_7 -II can be described as a cage structure built up by alternately stacking two sorts of layers parallel to the [001] direction: layers of the FeO_6 octahedra with composition of Fe_3O_6 and layers of pyro $\text{P}_2\text{O}_7^{4-}$ groups [119]. Each $\text{P}_2\text{O}_7^{4-}$ group shares four corners with one octahedra layer and the other two with another octahedra layer, resulting in the host structural unit $[\text{FeP}_2\text{O}_11]$ of this compound. This framework delimits elongated cages where two Na ions are enclosed. Nevertheless, it also provides paths along the [001] direction for Na^+ migration, indicating the possibility for Na (de)intercalation reaction activity.

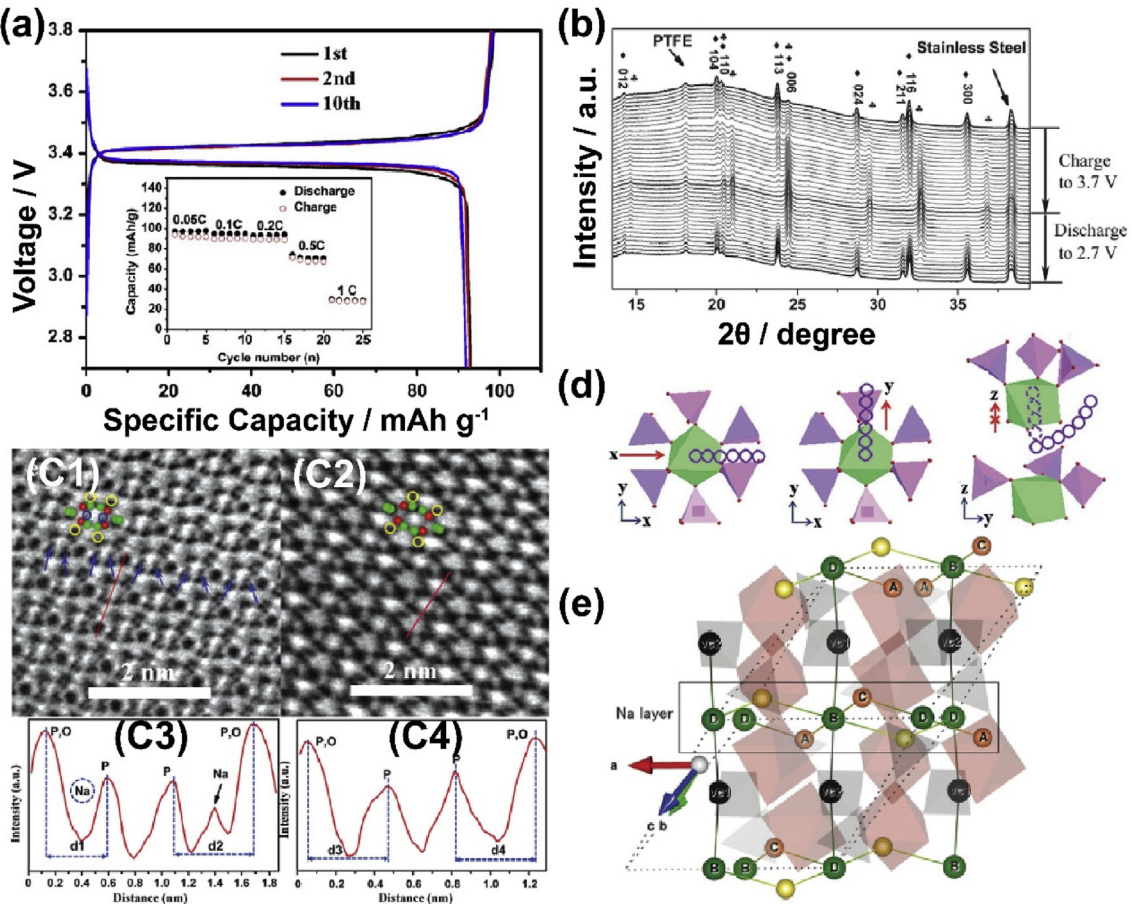


Fig. 4. (a) Charge–discharge curves for carbon-coated $\text{Na}_3\text{V}_2(\text{PO}_4)_3$ electrode in the voltage window of 2.7–3.8 V (inset of the rate capability). Reproduced with permission [108]. Copyright 2012, Elsevier. (b) In-situ XRD patterns during Na-insertion/extraction of the $\text{Na}_3\text{V}_2(\text{PO}_4)_3/\text{C}$ electrode at 0.1 C in the voltage range of 2.7–3.7 V. ◆ represents $\text{Na}_3\text{V}_2(\text{PO}_4)_3$ and ♦ represents $\text{NaV}_2(\text{PO}_4)_3$. Reproduced with permission [109]. Copyright 2013, Wiley-VCH. STEM-ABF images of (c1) $\text{Na}_3\text{V}_2(\text{PO}_4)_3$, and (c2) $\text{NaV}_2(\text{PO}_4)_3$ in the [111] projection (blue circles represent Na atoms located at Na(1) sites, yellow circles and blue arrows stand for Na atoms at Na(2) sites). Line files along ABF images of (c3) $\text{Na}_3\text{V}_2(\text{PO}_4)_3$ and (c4) $\text{NaV}_2(\text{PO}_4)_3$. Reproduced with permission [110]. Copyright 2014, Wiley-VCH. (d) Three possible sodium-ion diffusion pathways along x, y, and curved z directions. Reproduced with permission [111]. Copyright 2014, Royal Society of Chemistry. (e) Schematic depiction of three favorable migration routes in $\text{Na}_3\text{V}_2(\text{PO}_4)_3$: two intra-layer pathways (pathway 1 and pathway 2) and one inter-layer pathway (pathway 3). The orange-green lines and the yellow-green lines represent pathway 1 and pathway 2, respectively, the black-green lines indicate pathway 3. Reproduced with permission [112]. Copyright 2015, Royal Society of Chemistry.

Apart from NaFeP_2O_7 , other alternatives have also been developed to achieve high electrochemical activities for SIBs, such as NaTiP_2O_7 and NaVP_2O_7 [55,56,121,135]. Two forms of sodium titanium (III) diphosphate are unveiled: α - NaTiP_2O_7 (closely related to the structure of β -cristobalite) and β - NaTiP_2O_7 (isostructural to NaFeP_2O_7 -II). The presence of open tunnels in the host lattice is considered to be available for Na^+ mobility. Interestingly, in KAlP_2O_7 -type NaVP_2O_7 compound (β - NaVP_2O_7), reversible Na^+ insertion/extraction corresponding to partial $\text{V}^{3+}/\text{V}^{4+}$ redox activity at around 3.4 V vs. Na/Na^+ was observed for the first time by Okada et al. [121]. Despite the theoretical capacity of 108 mAh g⁻¹, it only delivered an initial capacity of 38 mAh g⁻¹ at 0.05 C within the electrochemical window of 2.5–4.0 V [122]. The limited Na^+ reaction activity of NaVP_2O_7 is not merely attributed to the sluggish ionic diffusion kinetics, but also to high intrinsic resistance induced by Na-extraction from the initial framework lattice, which restricts the two-phase transition kinetics between NaVP_2O_7 ($P2_1/c$) and $\text{Na}_{1-x}\text{VP}_2\text{O}_7$ ($P2_1$) symmetries. Very recently, Drozhzhin et al. introduced a carbon-coated NaVP_2O_7 electrode material fabricated via the hydrothermal-assisted post-calcination method [131]. It achieved a reversible capacity as high as 104 mAh g⁻¹ at the current density of 0.1 C with the average operating potential of 3.9 V vs. $\text{Na}/$

Na^+ , and outstanding rate performance of 90 mAh g⁻¹ capacity retention even at a high rate of 20 C (Fig. 5a). DFT calculations suggested that the low migration energy barrier of 0.25 eV for Na hop from site to site was account for its high-rate performance (Fig. 5b and c).

2.1.3.2. Two-sodium metal pyrophosphates $\text{Na}_2\text{MP}_2\text{O}_7$ ($M = \text{co, Fe, Mn, cu, Zn}$). Two-sodium metal pyrophosphates can be classified into three distinct polymorphs owing to the possible tetrahedral (MO_4) or octahedral (MO_6) coordination of the metal (M): (I) orthorhombic [$P2_1/cn$], (II) triclinic [$\bar{P}\bar{1}$], and (III) tetragonal [$P42/mnm$] [57,58,136]. The order of the thermodynamic stability follows the trend of I > II > III. Fig. 2f–h show the polymorphism, take a sample of $\text{Na}_2\text{CoP}_2\text{O}_7$, exhibiting their layered and three-dimensional structure with tunnels accommodating Na atoms. So, one could expect effective Na-ion transport in two-sodium metal pyrophosphates leading to good electrochemical performance.

Orthorhombic $\text{Na}_2\text{CoP}_2\text{O}_7$ possess a layered structure with slabs of $[\text{CoP}_2\text{O}_7]_\infty$ interconnected by oxygen-linked Co and P tetrahedral parallel to the [001] direction, stacked with alternating Na layers (Fig. 2f). The cobalt species are arranged in a tetrahedra fashion with oxygen atoms from four surrounding P_2O_7 units, while Na

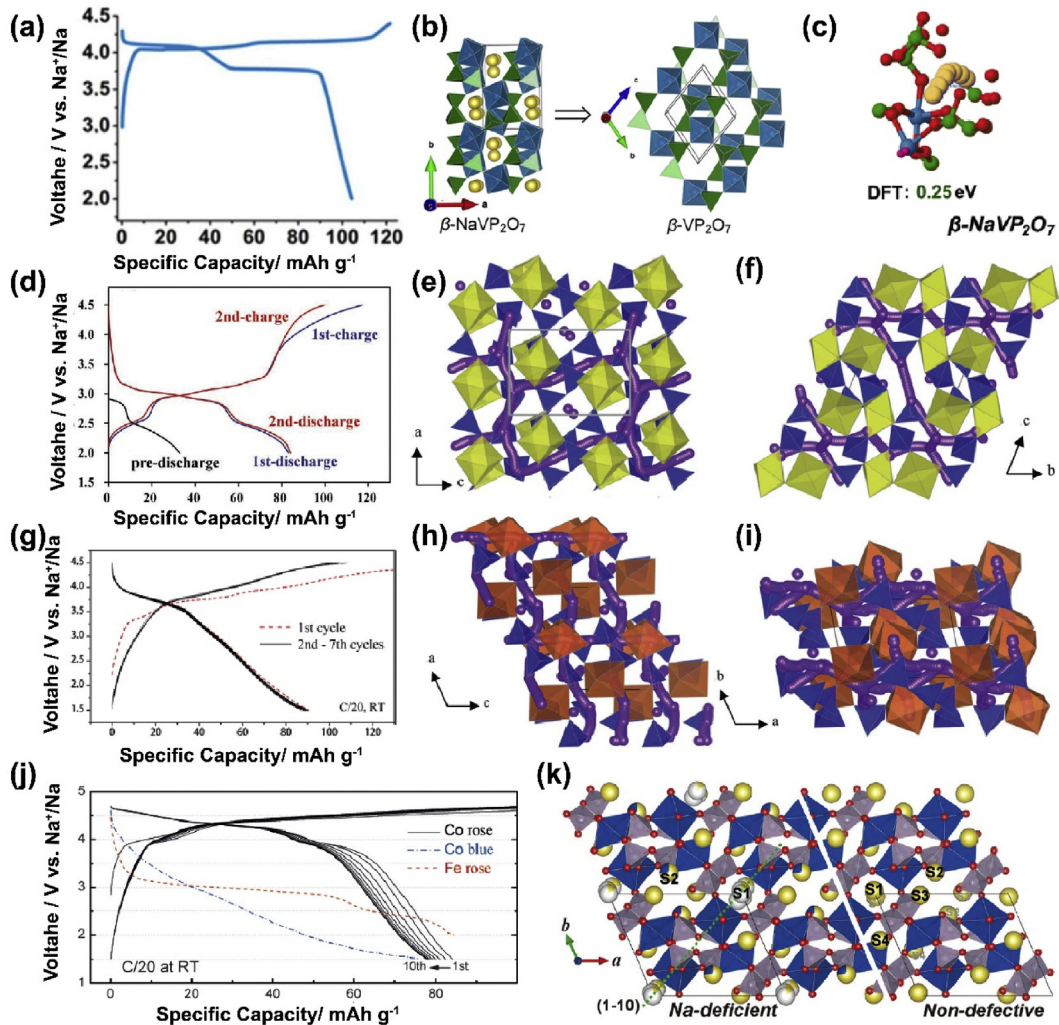


Fig. 5. (a) The voltage-capacity profile for KAlP₂O₇-type NaVP₂O₇ compound at a rate density of 10 mAh g⁻¹ between 2.0 and 4.4 V vs. Na/Na⁺. (b) Structural transformation from initial β -NaVP₂O₇ to the desodiated β -VP₂O₇ phase. (c) Na⁺ diffusion trajectory along the shorted migration pathways in β -NaVP₂O₇ with low migration energy barrier on the basis of first-principles calculations. Reproduced with permission [131]. Copyright 2019, American Chemical Society (ChemRxiv). (d) Galvanostatic charge/discharge curves of triclinic-Na₂FeP₂O₇ at 0.05 C in the voltage range of 2.0–4.5 V vs. Na/Na⁺. Reproduced with permission [132]. Copyright 2013, Wiley-VCH. The calculated pathways for long-range Na⁺ migration in triclinic-Na₂FeP₂O₇ along three axis directions viewing from the (e) ac-plane and (f) bc-plane. Reproduced with permission [122]. Copyright 2014, The Royal Society of Chemistry. (g) The typical charge–discharge profiles of Na₂MnP₂O₇ measured at 0.05 C in the voltage range of 1.5–4.5 V vs. Na/Na⁺. Reproduced with permission [133]. Copyright 2013, American Chemical Society. The calculated pathways for long-range Na⁺ migration in triclinic-Na₂MnP₂O₇ along three axis directions viewing from the (h) ac-plane and (i) ab-plane. Reproduced with permission [122]. Copyright 2014, The Royal Society of Chemistry. (j) Galvanostatic charge–discharge curves of triclinic Na₂CoP₂O₇ (rose), triclinic Na₂FeP₂O₇ (blue), and orthorhombic Na₂CoP₂O₇ (blue) polymorphs at 0.1 C. (k) Illustration scheme for the refined sodium-deficient crystal structure of the Na₂CoP₂O₇-rose (left) and the hypothetical Na₂CoP₂O₇-rose without defects (right). Reproduced with permission [134]. Copyright 2016, Wiley-VCH.

atoms enjoy a distorted octahedral configuration with six oxygen atoms around them. This structure generates two distinct organizations of Co and Na channels, in which four Na channels surround one each Co channel when viewing from the [010] projection, indicating 1D pathways for Na-ion migration in orthorhombic Na₂CoP₂O₇. Contrary to that, the triclinic Na₂CoP₂O₇ has a three-dimensional framework consisting of [CoP₂O₇]_∞ units built by CoO₆ octahedra corner-sharing PO₄ tetrahedra arranging in a staggered manner (Fig. 2g). It results in the formation of tunnels running along the [001] direction where Na atoms distribute, making a promising situation favorable for Na⁺ diffusion. Moreover, in the case of tetragonal Na₂CoP₂O₇, the layer-like nature is quite evident shown in Fig. 2h. Co atoms adopt a tetrahedral coordination geometry, and the isolated CoO₄ tetrahedra corner shares four oxygens from bridging P₂O₇ groups to form continuous [[CoP₂O₇]_∞]²⁻ sheets in the ab plane. The Na⁺ cations in a NaO₆

quadrangular prismatic coordination geometry are sandwiched between the [[CoP₂O₇]_∞]²⁻ layers, not only maintaining the charge neutrality but also keeping the structural stability from any bending or collapsing.

In the family of pyrophosphates, Na₂FeP₂O₇ was the first compound ever reported as the possible cathode material for SIBs [59]. It was found to be the isostructural to Na₂CoP₂O₇-II with a triclinic framework, providing 3D diffusing channels along [100], [110], and [011] directions [58]. As the transition metal changes from Co to Fe, slight variations in the lattice parameters can be observed (Table 1). Furthermore, triclinic Na₂FeP₂O₇ ($P\bar{1}$) shows excellent thermal stability and transforms into monoclinic $P2_1/c$ symmetry by further heating up to 560 °C with no oxygen evolution or structural rupture, indicating a safe electrode candidate for practical SIB applications [137]. One mole of Na ion can be reversibly inserted/extracted for each formula unit of triclinic-Na₂FeP₂O₇ based on the

$\text{Fe}^{2+}/\text{Fe}^{3+}$ redox reaction, resulting in a theoretical capacity of 97 mAh g^{-1} . Typical galvanostatic voltage-capacity curves of triclinic- $\text{Na}_2\text{FeP}_2\text{O}_7$ in a Na-cell is shown in Fig. 5d. $\text{Na}_2\text{FeP}_2\text{O}_7$ showed a reversible capacity of ~84 mAh g^{-1} while exhibiting two distinct plateaus in the total potential range of 2.0–4.5 V vs. Na/Na^+ , with large overpotentials [132]. Based on the quasi-equilibrium measurements and DFT calculations, it has been demonstrated that $\text{Na}_2\text{FeP}_2\text{O}_7$ underwent a single-phased transition reaction at ~2.5 V, during a series of consecutive two-phase reactions in the voltage range of 3–3.25 V. The Na-ion diffusion properties in all crystallographic directions in $\text{Na}_2\text{FeP}_2\text{O}_7$ were also considered, as depicted in Fig. 5e and f. The resulted migration energies for Na^+ diffusion along the three axes in $\text{Na}_2\text{FeP}_2\text{O}_7$ were all lower than 0.49 eV, indicating the high Na^+ mobility rooted in the 3D pyrophosphate $\text{Na}_2\text{FeP}_2\text{O}_7$ framework.

To date, a variety of polymorphs and analogues of $\text{Na}_2\text{MP}_2\text{O}_7$ have been investigated, including $\text{Na}_2\text{CoP}_2\text{O}_7$ [134,138], $\text{Na}_2\text{MnP}_2\text{O}_7$ [60], $\text{Na}_2\text{CuP}_2\text{O}_7$ [139,140], and $\text{Na}_2\text{ZnP}_2\text{O}_7$ [63,141], $\text{Na}_2\text{MnP}_2\text{O}_7$, as the isostructural to $\text{Na}_2\text{FeP}_2\text{O}_7$, was discovered in 1998 [60]. The possibility for realizing the reversible redox activity of $\text{Mn}^{2+}/\text{Mn}^{3+}$ makes this compound attractive for cathode material for SIBs. At a rate of 0.05 C, a reversible capacity of ~90 mAh g^{-1} (theoretical capacity of 97.5 mAh g^{-1}) in the voltage range of 1.5–4.5 V (vs. Na/Na^+) and a high operating potential at ~3.8 V were obtained (Fig. 5g). $\text{Na}_2\text{MnP}_2\text{O}_7$ exhibited good rate capability (69% capacity retention with the current rate increasing from 0.05 C to 1 C) and cycling performance (96% of the initial capacity retained after 30 cycles at 0.05 C) [133]. According to the DFT results and detailed atomic structural analysis, the enhanced kinetics of $\text{Na}_2\text{MnP}_2\text{O}_7$, superior to that of the Li-counterpart $\text{Li}_2\text{MnP}_2\text{O}_7$ and being comparable to that of $\text{Na}_2\text{FeP}_2\text{O}_7$, was mainly due to the locally flexible accommodation of Jahn-Teller distortions aided by the corner-sharing crystal structure in triclinic $\text{Na}_2\text{MnP}_2\text{O}_7$. It was proven that a small degree of atomic rearrangement in the positions of metal and oxygen atoms as well as resultant changes in their bond lengths between the sodiation and desodiation states lower the energy barriers of electron conduction and phase boundary migration. 3D Na-ion channels with low migration barrier of 0.58 eV were consisted with the good electrochemical behavior observed for triclinic $\text{Na}_2\text{MnP}_2\text{O}_7$ (Fig. 5h and i) [122]. In order to further improve the rate capability of $\text{Na}_2\text{MnP}_2\text{O}_7$, mix metal pyrophosphates, such as $\text{Na}_2\text{Mn}_{0.5}\text{Fe}_{0.5}\text{P}_2\text{O}_7$ [142] and $\text{Na}_2\text{Mn}_{0.5}\text{Zn}_{0.5}\text{P}_2\text{O}_7$ [143], were developed through lattice substitution of Mn with other metals. Later, to further increase the energy density of $\text{Na}_2\text{MP}_2\text{O}_7$, the redox center was shifted from Mn to Co. Orthorhombic $\text{Na}_2\text{CoP}_2\text{O}_7$ achieved a reversible capacity of 90 mAh g^{-1} at 20/C with an average potential of 3 V involving $\text{Co}^{3+}/\text{Co}^{2+}$ redox reaction [144]. Kim et al. demonstrated a 4.3 V triclinic $\text{Na}_2\text{CoP}_2\text{O}_7$ (rose form) cathode material for SIBs, which can be easily realized by simple introduction of sodium deficiencies to its stoichiometric polymorph (orthorhombic $\text{Na}_2\text{CoP}_2\text{O}_7$, blue form) [134]. In the voltage profiles shown in Fig. 5j, an average voltage of only 3.0 V was observed in blue- $\text{Na}_2\text{CoP}_2\text{O}_7$. In remarkable contrast, rose- $\text{Na}_2\text{CoP}_2\text{O}_7$ exhibited a significant increase in energy density of more than 40% compared to the blue polymorph (344 vs. 240 Wh kg^{-1}). It showed stable cycling behavior with two types of voltage plateaus, one relatively low voltage plateau at ~3.95 V and two high voltage plateaus at 4.33 and 4.43 V, respectively. Fig. 5k describes the refined sodium-deficient crystal structure of the obtained rose- $\text{Na}_2\text{CoP}_2\text{O}_7$ polymorph with comparison of the hypothetical rose- $\text{Na}_2\text{CoP}_2\text{O}_7$ phase without sodium defects. Such non-stoichiometric-driven control of polymorphism may pave a way for developing high-performance electrode materials for both LIBs and SIB applications.

2.1.3.3. The mixed pyrophosphates $\text{Na}_4\text{M}_3(\text{PO}_4)_2\text{P}_2\text{O}_7$ ($\text{M} = \text{Fe}, \text{Co}, \text{Mn}, \text{Ni}, \text{Mg}$). Similarly, a unique framework structure providing robust structural stability during the electrochemical reaction process and the mixed pyrophosphates $\text{Na}_4\text{M}_3(\text{PO}_4)_2\text{P}_2\text{O}_7$ ($\text{M} = \text{Fe}, \text{Co}, \text{Mn}, \text{Ni}, \text{Mg}$) as a fascinating new class of polyanion materials are of considerable current research interests [126]. After the pioneering work of Goodenough et al. [145,146], the mixed polyanion groups of phosphate PO_4^{3-} and pyrophosphate $\text{P}_2\text{O}_7^{4-}$ can be stabilized in the Na system (not found in the Li system), which show promising electrochemical properties for both LIBs and SIBs [66,68].

Considering the electrode material design for large-scale electrical energy storage, the earth-abounded and low-cost $\text{Na}-\text{Fe}-\text{P}-\text{O}$ system seems to be very attractive. Iron-based $\text{Na}_4\text{Fe}_3(\text{PO}_4)_2\text{P}_2\text{O}_7$, as the first compound ever reported in this class, was proven to be one of the promising candidates for cathode materials for both LIBs and SIBs [66,147]. The neutron diffraction results confirmed that the crystal structure of $\text{Na}_4\text{Fe}_3(\text{PO}_4)_2\text{P}_2\text{O}_7$ is isostructural to $\text{Na}_4\text{M}_3(\text{PO}_4)_2\text{P}_2\text{O}_7$ ($\text{M} = \text{Co}, \text{Mn}, \text{Ni}$) with a space group of $Pn2_1a$ [66,68]. As shown in Fig. 2i, the structure of $\text{Na}_4\text{Fe}_3(\text{PO}_4)_2\text{P}_2\text{O}_7$ can be described as a 3D network of $[\text{Fe}_3\text{P}_2\text{O}_{13}]_\infty$ layers parallel to the bc plane built by FeO_6 octahedra and PO_4 tetrahedra. Each FeO_6 octahedron shares one edge and four corners with each other, and PO_4 tetrahedron shares one edge and two corners with FeO_6 octahedra, forming the infinite $[\text{Fe}_3\text{P}_2\text{O}_{13}]_\infty$ layer. The diphosphate P_2O_7 groups bridging connects the $[\text{Fe}_3\text{P}_2\text{O}_{13}]_\infty$ layer along the a axis, generating large 1D Na-diffusion channels along the [010] direction. $\text{Na}_4\text{Fe}_3(\text{PO}_4)_2\text{P}_2\text{O}_7$ exhibited stable and fast electrochemical activity in sodium batteries, delivering nearly 82% of the theoretical capacity (129 mAh g^{-1}) at ~3.2 V (vs. Na/Na^+) under the rate of 0.05 C in the first cycle with relatively stable cycle retention, competitive with other cathode materials for SIBs (Fig. 6a) [147]. By using a combination of electrochemical experiments and first-principles calculations, Kang et al. clarified that the (de)sodiation of the $\text{Na}_4\text{Fe}_3(\text{PO}_4)_2\text{P}_2\text{O}_7$ electrode was governed mainly via a single-phase reaction based on one electron $\text{Fe}^{3+}/\text{Fe}^{2+}$ redox couple with an exceptionally small volume change of less than 4% during the electrochemical cycling (Fig. 6b). Furthermore, to better understand the sodium storage mechanism in the class of the mixed phosphates $\text{Na}_4\text{M}_3(\text{PO}_4)_2\text{P}_2\text{O}_7$ ($\text{M} = \text{Fe}, \text{Co}, \text{Mn}, \text{Ni}$), a combination of atomistic energy minimization, molecular dynamics (MD), and DFT simulations was brought out to examine key issues including intrinsic defects, Na-diffusion mechanisms, and voltage trends [126]. Firstly, the results of atomistic energy minimization demonstrated that the most energetically favorable type of intrinsic defect was predicted to be the Na/M anti-site pair for all compositions. Secondly, long-scale MD simulations suggested Na atoms tend to diffuse across 3D migration pathways with relatively high Na^+ -diffusion coefficients and low activation barriers that were comparable to those of the Li-ion cathodes. Finally, the DFT method predicted that doping Ni in $\text{Na}_4\text{Fe}_3(\text{PO}_4)_2\text{P}_2\text{O}_7$ could lead to an increased value of the operation voltage.

Following the study of $\text{Na}_4\text{Fe}_3(\text{PO}_4)_2\text{P}_2\text{O}_7$, $\text{Na}_4\text{Co}_3(\text{PO}_4)_2\text{P}_2\text{O}_7$ has also shown its electrochemical activity for SIBs [128]. Reversible capacity of $\text{Na}_4\text{Co}_3(\text{PO}_4)_2\text{P}_2\text{O}_7$ reached ~95 mAh g^{-1} (around 50% of its theoretical capacity of 170 mAh g^{-1}) at 0.2 C between 3.0 V and 4.7 V, corresponding to 2.2 Na^+ cations reversibly (de)intercalating into/from the $\text{Na}_4\text{Co}_3(\text{PO}_4)_2\text{P}_2\text{O}_7$ electrode. Very recently, the structure evolution in $\text{Na}_4\text{Co}_3(\text{PO}_4)_2\text{P}_2\text{O}_7$ upon electrochemical cycling was carefully examined by Cabanas's group [148]. Coupling *operando* X-ray diffraction and electrochemical impedance spectroscopy (EIS) measurements demonstrated that $\text{Na}_4\text{Co}_3(\text{PO}_4)_2\text{P}_2\text{O}_7$ proceeded a complex reaction mechanism consisting of four consecutive biphasic reactions followed by a single-phase process at the end of charge. The incomplete Na^+ intercalation in the first

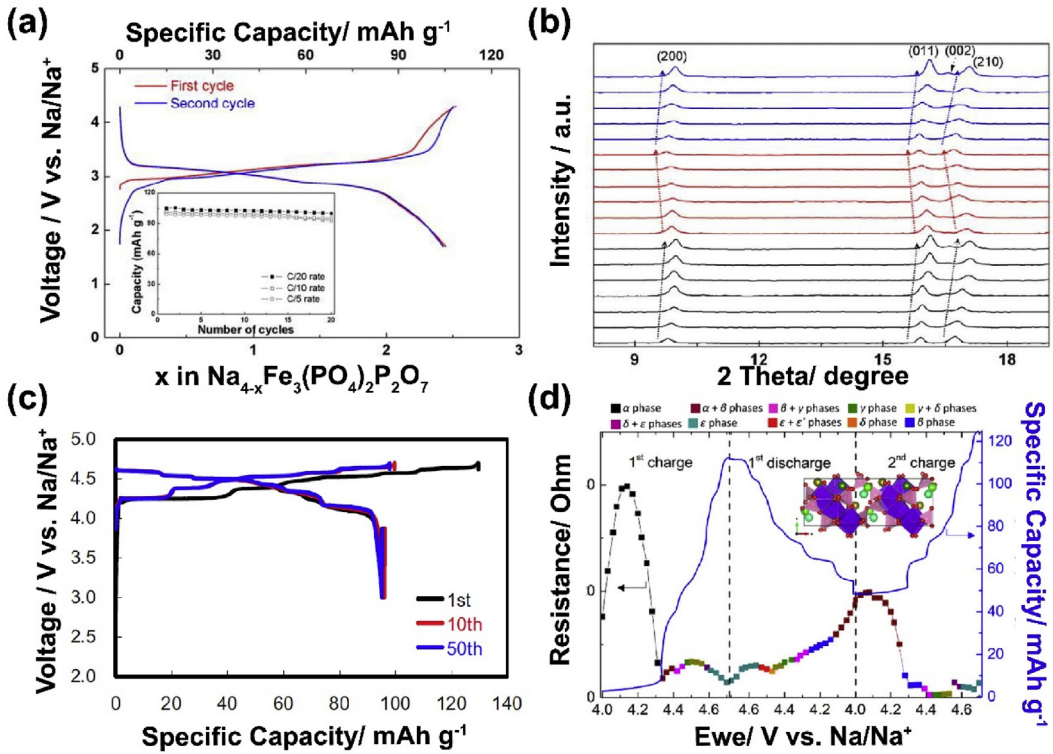


Fig. 6. (a) Galvanostatic charge–discharge curves of $\text{Na}_4\text{Fe}_3(\text{PO}_4)_2\text{P}_2\text{O}_7$ for the first two cycles at the rate of 0.05 C in a Na-ion cell. The inset demonstrates the cycling properties at 0.05, 0.1, and 0.2 C, respectively. (b) Amplified *ex situ* XRD patterns in the 2θ range of 8–19° of $\text{Na}_4\text{Fe}_3(\text{PO}_4)_2\text{P}_2\text{O}_7$ upon electrochemical cycling, demonstrating the one-phase reaction mechanism for sodium storage. Reproduced with permission [147]. Copyright 2013, American Chemical Society. (c) Galvanostatic charge–discharge curves of $\text{Na}_4\text{Co}_3(-\text{PO}_4)_2\text{P}_2\text{O}_7$ for the 1st, 10th, and 50th cycles at 0.2 C between 3.0 V and 4.7 V vs. Na/Na^+ . Reproduced with permission [128]. Copyright 2013, Elsevier. (d) Schematic illustration of the sodium storage reaction mechanism of $\text{Na}_4\text{Co}_3(\text{PO}_4)_2\text{P}_2\text{O}_7$. Reproduced with permission [148]. Copyright 2019, American Chemical Society.

cycle was found to be beneficial for the transport kinetics and cycling stability, owing to that it effectively avoided a huge increasement in the values of charge-transfer resistance (R_{ct}) for the following cycle.

2.1.4. Fluorophosphates

Introduction of electronegative fluorine F^- anions into sodium-based phosphates produces a new class of host structures and compositions, namely, fluorophosphates, because it alters the charge balance or the dimensionality of the structure in relation to phosphates. The fluorophosphates saga started with the first demonstration of $\text{Na}_2\text{VPO}_4\text{F}$ by Barker et al. in 2003 [149], which triggered the exploration of various fluorophosphates serving as the electrode materials for SIBs and extended fluorophosphates chemistry to other transition metals. The presence of high ionic F^- in the anion sublattice structure with strong bond covalency stabilizes the antibonding $\text{M}^{n+1}/\text{M}^{n+}$ state though strong inductive effect, thereby increasing the redox voltage. Fluorophosphates with a chemical composition of $\text{Na}_2\text{MPO}_4\text{F}$ ($\text{M} = \text{V}, \text{Fe}, \text{Mn}, \text{Ni}$) and $\text{Na}_3\text{V}_2\text{O}_2(\text{PO}_4)_2\text{F}_{3-X}$ ($0 \leq X \leq 1$) have been widely regarded as attractive candidates for SIBs.

2.1.4.1. $\text{Na}_2\text{MPO}_4\text{F}$ ($\text{M} = \text{V}, \text{Fe}, \text{Mn}, \text{Ni}$). $\text{Na}_2\text{VPO}_4\text{F}$, one of the earliest fluorophosphate-type electrode materials for SIBs, can be crystallized into two polymorphs: high-temperature tetragonal symmetry with the $I4/mmm$ space group and low-temperature monoclinic phase with a space group of $C2/c$ [69]. The tetragonal- $\text{Na}_2\text{VPO}_4\text{F}$ demonstrates facile sodium-ion diffusion through an extended 3D framework built up from $[\text{VO}_4\text{F}_2]$ octahedra connected with $[\text{PO}_4]$ tetrahedra producing cavities where Na^+ ions statistically distributed. Tetragonal- $\text{Na}_2\text{VPO}_4\text{F}$ has a high theoretical capacity of 143

mAh g^{-1} based on the $\text{V}^{4+}/\text{V}^{3+}$ redox reaction, according to reversible (de)insertion of one Na^+ per $\text{Na}_2\text{VPO}_4\text{F}$ formula unit. Employing the highly ionic bands and inductive effect from both PO_4^{3-} and F^- , it leads to a high operating plateau of around 3.7 V in a Na-ion full-cell assembled with commercially available hard carbon as the anode [149]. The exciting results provoked numerous research interests in the scientific community [150–154]. Zhou et al. reported another polymorph $\text{Na}_2\text{VPO}_4\text{F}$ with $C2/c$ symmetry [155]. The monoclinic- $\text{Na}_2\text{VPO}_4\text{F}$ synthesized by the one-step soft template method delivered a high initial discharge capacity of 133 mAh g^{-1} at 0.1 C with a flat voltage plateau at ~3.3 V vs. Na/Na^+ and excellent high rate cycling stability (capacity retention of 81% and 77% of 10000 cycles at 10 C and 20 C, respectively). It should be mentioned that the clear clarifications of the crystal structure of monoclinic- $\text{Na}_2\text{VPO}_4\text{F}$ is yet to be reported.

$\text{Na}_2\text{FePO}_4\text{F}$ is considered an excellent candidate of low-cost and environmentally friendly ion-based positive electrode materials that operates on $\text{Fe}^{2+}/\text{Fe}^{3+}$ redox. $\text{Na}_2\text{FePO}_4\text{F}$ crystallizes into orthorhombic structure with $Pbcn$ space group, isostructural to $\text{Na}_2\text{FePO}_4\text{OH}$ [70]. Compared to the V-based fluorophosphate $\text{Na}_2\text{VPO}_4\text{F}$, $\text{Na}_2\text{FePO}_4\text{F}$ has a 2D layered framework composed by $[\text{FePO}_4\text{F}]$ infinite slabs stacking with sodium ions in the interlayer (Fig. 2g). The $\text{Fe}_2\text{O}_7\text{F}_2$ bi-octahedra units, consisting of face-sharing FeO_4F_2 octahedral subunits abridged with F atoms, are corner-sharing with PO_4 tetrahedral, forming the layer-like unit along the $a-c$ directions. There are two different crystallographic sodium sites to accommodate sodium ions. Nazar et al. in 2007 used $\text{Na}_2\text{FePO}_4\text{F}$ directly as the cathode material in a Li-ion cell, demonstrating the extraction possibility of sodium ions with solid-solution-like electrochemical behavior in $\text{Na}_2\text{FePO}_4\text{F}$ [158]. The sodium-storage performance of $\text{Na}_2\text{FePO}_4\text{F}$ in a Na-ion cell was first

reported by Recham et al., exhibiting a reversible capacity of 120 mAh g⁻¹ (theoretical capacity of 124 mAh g⁻¹) in the first cycle [159]. Various modification methods were applied to improve the electrochemical performance in Na₂FePO₄F for SIBs [160–166]. The sodium mobility in the Na₂FePO₄F lattice was demonstrated to be 2D pathways along the *a*–*c* planes with a similar low activation energy [167]. *In operando* XRD analysis was performed to investigate the structural evolution of Na₂FePO₄F during the Na-ions insertion/extraction process, indicating two two-phase reaction behaviors between three structures corresponding to the Na₂FePO₄F ↔ Na_{1.5}FePO₄F ↔ Na₁FePO₄F phase transition process (Fig. 7a and b) [156]. According to the *ex situ* solid-state nuclear magnetic resonance (²³Na ssNMR) and DFT calculation results, the intermediate phase Na_{1.5}FePO₄F adopted the P2₁/c space group, whereas both the starting Na₂FePO₄F and ending Na₁FePO₄F adopt the Pbcn space group (Fig. 7c and d) [157]. Furthermore, it was proven that Na ions at Na2 sites were electrochemically active whereas those on Na1 sites are immobile upon electrochemical cycling.

2.1.4.2. $\text{Na}_3\text{V}_{2-2x}(\text{PO}_4)_{2}\text{F}_{1+2x}$ ($0 \leq x \leq 1$). For most interesting composition in terms of energy density, vanadium-based fluorophosphates with general formula Na₃V_{2-2x}(PO₄)₂F_{1+2x} ($0 \leq x \leq 1$) have received significant attention as alternatives to traditional layered metal oxides as positive electrodes for both LIBs

and SIBs [168–172]. Depending on *x*, the oxidation state of vanadium (between +3 and +4) varies with concomitant changes of the crystal/electronic structure as well as the electrochemical behavior of the materials. Of particular interests are the two extreme members: Na₃V₂(PO₄)₂F₃, where *x* = 1; and Na₃V₂(PO₄)₂O₂F, where *x* = 0.

Replacing one-third of PO₄³⁻ anion from Na₃V₂(PO₄)₃ by three F⁻ anions, Na₃V₂(PO₄)₂F₃ crystallizes in rhombohedral NASICON structure with P4₂/mm space group, which was determined from the single-crystal XRD in 1999 by Le Meins et al. [71]. Although Croguennec and his co-workers argued that Na₃V₂(PO₄)₂F₃ has a subtle orthorhombic distortion in *Amam* space group by using high angular resolution synchrotron radiation diffraction [173], most of the literature report Na₃V₂(PO₄)₂F₃ adopting a P4₂/mm space group. Fig. 2k displays the crystal structure of rhombohedral Na₃V₂(PO₄)₂F₃, with a 3D framework that is built up with [V₂O₈F₃] bi-octahedra abridged by [PO₄] tetrahedral via O atoms that lead to the formation of large channels along *a* and *b*-axes with Na located in the tunnel sites. Two distinct crystallographic Na sites exist in this open framework with an occupancy ratio of 2:1, namely Na1 sites (fully occupied) and Na2 sites (half occupied). Na₃V₂(PO₄)₂F₃ was first reported as an alkali ion insertion host material by Barker et al., in 2006, exhibiting a specific capacity of ~120 mAh g⁻¹ at a high average voltage plateau of 4.1 V vs. Li/Li⁺ in a Li-ion cell [174,175].

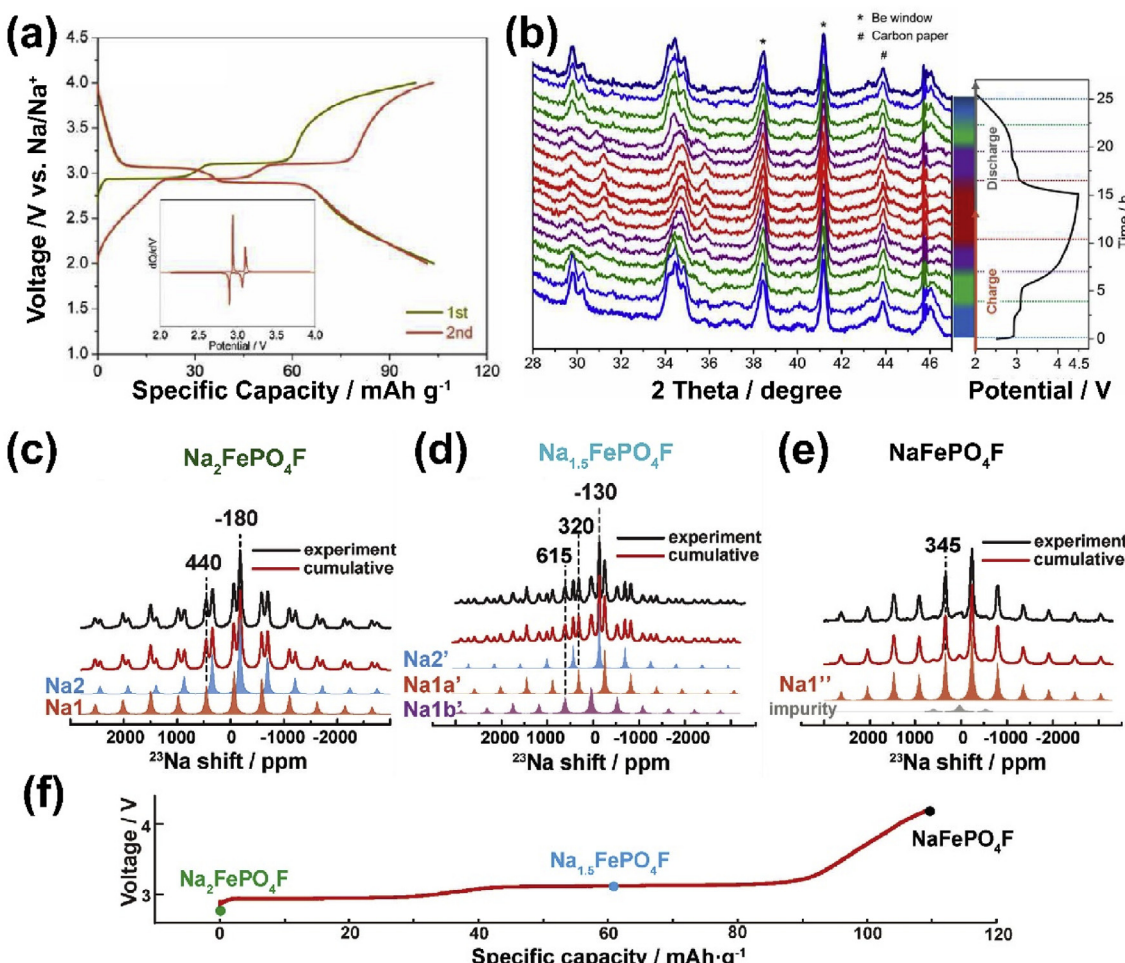


Fig. 7. (a) Charge–discharge curves for the carbon-coated Na₂FePO₄F sample with LA132 binder at 0.1 C. Inset is the corresponding dQ/dV plots. (b) *In situ* XRD patterns for Na₂FePO₄F during the electrochemical cycling under 0.1 C between 2.0 and 4.5 V vs. Na/Na⁺. Reproduced with permission [156]. Copyright 2017, American Chemical Society. ²³Na ssNMR spectra of Na₂FePO₄F (c), Na_{1.5}FePO₄F (d), and Na₁FePO₄F (e), respectively, with their corresponding cumulative spectra. (f) The first charge profile of Na₂FePO₄F with corresponding marks for three different phases. Reproduced with permission [157]. Copyright 2018, Wiley-VCH.

The Na-ion (de)intercalating properties of $\text{Na}_3\text{V}_2(\text{PO}_4)_2\text{F}_3$ was first demonstrated by Kang et al., with a decent theoretical capacity of 192 mAh g⁻¹ calculated for (de)intercalation of three Na ions per formula unit [176]. In spite of this, until now, only the reversible extraction of 2 Na⁺ has been experimentally achieved in a Na-ion cell, corresponding to the theoretical energy density as high as ~507 Wh kg⁻¹, which is comparable to those of the commercial LiFePO₄ (~580 Wh kg⁻¹) and LiMn₂O₄ (~480 Wh kg⁻¹) [174,175,177]. Furthermore, it is worth to note that the chemically desodiated phase shows high thermally stability up to 550 °C, implying the excellent safety characteristic of this electrode compound.

Various *in situ* and *ex situ* techniques including XRD, synchrotron XRD, and X-ray absorption spectroscopy (XAS) as well as ssNMR were employed to investigate the sodium storage mechanism in $\text{Na}_3\text{V}_2(\text{PO}_4)_2\text{F}_3$. Fig. 8a displays a typical voltage–composition profile of $\text{Na}_3\text{V}_2(\text{PO}_4)_2\text{F}_3$, showing two main voltage domains at around 3.7 and 4.2 V vs. Na/Na⁺. High angular resolution synchrotron radiation diffraction results (Fig. 8b) revealed a complicated phase transformations sequence. It was found that three biphasic reactions involving two distinct intermediate phases $\text{Na}_{2.4}\text{V}_2(\text{PO}_4)_2\text{F}_3$ and $\text{Na}_{2.2}\text{V}_2(\text{PO}_4)_2\text{F}_3$ formed in the lower voltage region, subsequently a wide solid-solution process of composition $\text{Na}_x\text{V}_2(\text{PO}_4)_2\text{F}_3$ ($1.3 \leq x \leq 1.8$) with $I4/mmm$ symmetry was observed. The end-member $\text{NaV}_2(\text{PO}_4)_2\text{F}_3$ belonging to Cmc_2_1 space group and two dissimilar vanadium environments (a V³⁺–V⁵⁺ couple in every biotahedron) is finally attained through another biphasic transition reaction (Fig. 8c). The local structural and dynamical evolutions during cycling in $\text{Na}_3\text{V}_2(\text{PO}_4)_2\text{F}_3$ were further investigated by detailed *in situ* XRD and high-resolution ²³Na and ³¹P ssNMR, revealing Na ions were removed non-selectively from Na1 and Na2 sites at least at the beginning of charge (Fig. 8d and e) [179]. By utilizing DFT simulations, ion reorganization during electrochemical cycling was proposed to be

involved. Different designed Na-ion pathways along three axes exhibiting low activation energies demonstrated the 3D characteristics in $\text{Na}_3\text{V}_2(\text{PO}_4)_2\text{F}_3$ for Na⁺ migration feasibilities (Fig. 8f).

Recently, $\text{Na}_3\text{V}_2\text{O}_2(\text{PO}_4)_2\text{F}$ with lower F content becomes to be a new fashion electrode material for SIBs. With the substitution of O²⁻ for F⁻, $\text{Na}_3\text{V}_2\text{O}_2(\text{PO}_4)_2\text{F}$ equips with higher and single oxidation state (+4) for vanadium. Furthermore, low F content provides weaker inductive effect and electronegativity as well as lower attraction interaction between Na(2) and F, which could facilitate Na-ions diffusion in the lattice and lower the electrochemical polarization [181,182]. As suggested by Baudrin's [72] and Massa's group [183], $\text{Na}_3\text{V}_2\text{O}_2(\text{PO}_4)_2\text{F}$ crystallized to a tetragonal framework with $I4/mmm$ symmetry. After that, Tsirlin et al. proposed another $\text{Na}_3\text{V}_2\text{O}_2(\text{PO}_4)_2\text{F}$ polymorph with $P4_2/mnm$ space group as the room-temperature phase [73]. $\text{Na}_3\text{V}_2\text{O}_2(\text{PO}_4)_2\text{F}$ has similar framework with $\text{Na}_3\text{V}_2(\text{PO}_4)_2\text{F}_3$, as shown in Fig. 2l, excepting one O in $\text{Na}_3\text{V}_2\text{O}_2(\text{PO}_4)_2\text{F}$ replacing one F in $\text{Na}_3\text{V}_2(\text{PO}_4)_2\text{F}_3$. Sauvage et al. in 2006 first demonstrated the feasibility of Na-ion extraction in $\text{Na}_3\text{V}_2\text{O}_2(\text{PO}_4)_2\text{F}$ for SIBs [72]. Two-step voltage plateaus found at 3.6 and 4.0 V were clear characteristics of two bi-phasic transition reactions. Deep studies on the reaction mechanisms and structural evolutions of the $\text{Na}_3\text{V}_2\text{O}_2(\text{PO}_4)_2\text{F}$ electrode during use in a Na-ion cell were proceeded by *in situ* synchrotron XRD combined X-ray absorption near-edge spectroscopy (XANES) [184]. A complex reaction mechanism including both solid-solution and two-phase behavior during charge and discharge was proposed.

It should be noted that the multi-electron transfer behavior based on the various vanadium redox reactions can be easily realized by tuning the F contents in $\text{Na}_3\text{V}_2\text{O}_{2-x}(\text{PO}_4)_2\text{F}_{1+2x}$. Park et al. for the first time successfully synthesized a series of the isostructural $\text{Na}_3\text{V}_2\text{O}_{2-x}(\text{PO}_4)_2\text{F}_{1+2x}$ ($0 \leq x \leq 1$) compounds via a solid-state reaction and demonstrated all compositions in this family showing potentials as high-perform cathode materials for SIBs [185]. The combination of various redox reaction transitions

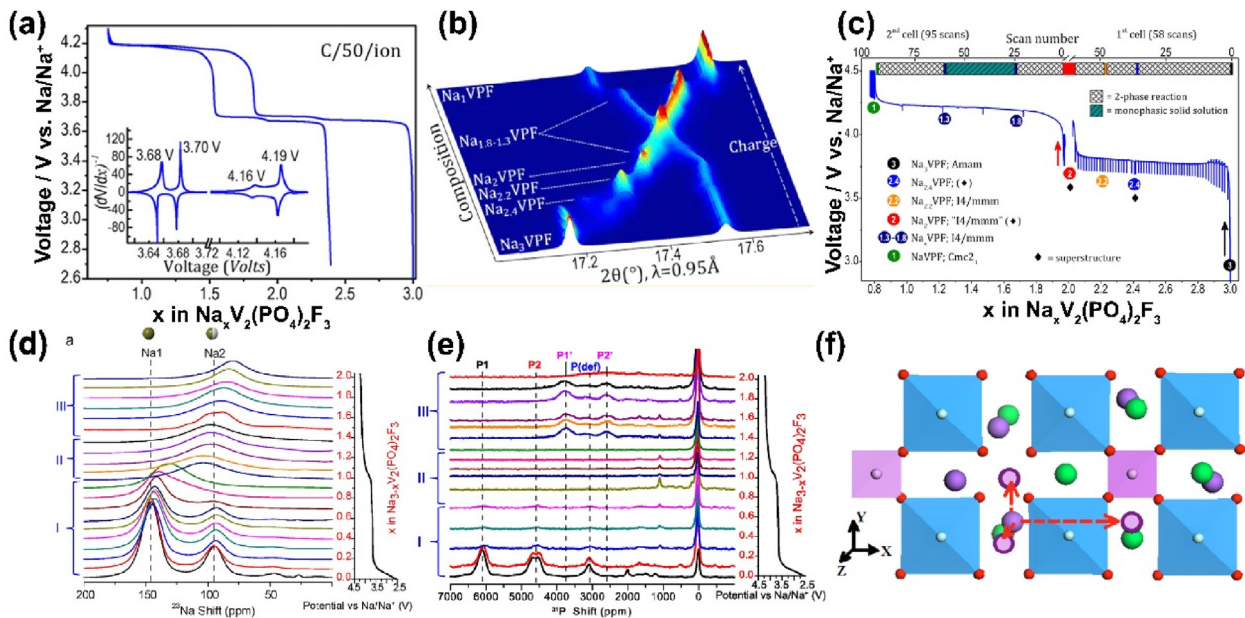


Fig. 8. (a) Typical voltage–composition profile of $\text{Na}_3\text{V}_2(\text{PO}_4)_2\text{F}_3$ at 0.02 C (per exchanged ion). Inset: corresponding inverse derivative (dQ/dV)⁻¹ curve where several pairs of redox couples can be identified. (b) *In situ* XRD patterns in the 17–17.8° angular 2θ range for the $\text{Na}_3\text{V}_2(\text{PO}_4)_2\text{F}_3$ electrode. (c) Potential–composition electrochemical curves for $\text{Na}_3\text{V}_2(\text{PO}_4)_2\text{F}_3$ vs. Na/Na⁺ with marks for different single-phase compositions upon Na⁺ extraction. Reproduced with permission [178]. Copyright 2015, American Chemical Society. Ex *situ* ²³Na ssNMR spectra (d) and ³¹P spectra ssNMR (e) of $\text{Na}_3\text{V}_2(\text{PO}_4)_2\text{F}_3$ electrodes at various states of charge. Reproduced with permission [179]. Copyright 2014, American Chemical Society. (f) Schematic illustration of the geometric model for Na-ion migrations in $\text{Na}_3\text{V}_2(\text{PO}_4)_2\text{F}_3$ along x-, y-, z-axes directions. The green spheres represent the Na ions at Na1 sites whereas the purple spheres describe the Na ions at Na2 sites. Reproduced with permission [180]. Copyright 2014, American Chemical Society.

(V^{3+}/V^{4+} or V^{4+}/V^{5+}), Na^+-Na^+ ordering, and F/O distribution resulted in distinct voltage–composition curves, according to the Na (de)intercalation mechanisms for the $\text{Na}_3\text{V}_2\text{O}_{2-2x}(\text{PO}_4)_2\text{F}_{1+2x}$ family (Fig. 9a). As one of them, $\text{Na}_3\text{V}_2\text{O}_{1.6}(\text{PO}_4)_2\text{F}_{1.4}$ exhibited high energy density of approximately 600 Wh kg⁻¹, attributed to a redox reaction of 1.2 electrons transfer (Fig. 9b) [186]. As shown in Fig. 9c, such high energy density exceeds that of any other reported cathodes for SIBs. Encouragingly, according to the DFT calculations, the energy density can be further improved to 758 Wh kg⁻¹ with the replacement of O^{2-} with Cl^- to form $\text{Na}_3\text{V}_2\text{Cl}_2(\text{PO}_4)_2\text{F}$ due to its extraordinary theoretical capacity of 188 mAh g⁻¹ (Fig. 9d) [188].

2.1.5. Sulfates

Benefited from the inductive effect of the polyanionic groups in polyanion-type materials, higher operation potential can be realized by substituting a phosphate PO_4^{3-} unit by a SO_4^{2-} group owing to its higher electronegativity. Sulfates are also considered promising polyanionic cathode materials taking advantages of the economic Na–Fe–S–O elemental constitution. Alluaudite-type $\text{Na}_3\text{Fe}_2(\text{SO}_4)_2$ is of particular interests, first reported by Yamada's group for SIB applications [189,190], which possesses a 3D framework structure forming by edge-sharing Fe_2O_{10} dimers in turn bridged with SO_4 units. Highest-ever operating potential at 3.8 V (vs. Na/Na^+) based on the $\text{Fe}^{3+}/\text{Fe}^{2+}$ redox couple was initially found among all known Fe-based oxides and oxyanionic insertion compounds. Thus, the theoretical energy density by full utilization

of inherent Na-ions of $\text{Na}_3\text{Fe}_2(\text{SO}_4)_2$ can reach extremely high value of 540 Wh kg⁻¹, even higher than those of LiMn_2O_4 (430 Wh kg⁻¹) and LiFePO_4 (500 Wh kg⁻¹), indicating promising applications for SIBs competitive with state-of-the-art LIBs. Definite efforts to further improve the electrochemical performance through structural engineering and/or surface modification have been extensively done [191–194]. For example, freestanding and flexible $\text{Na}_{2+2x}\text{Fe}_{2-x}(\text{SO}_4)_3@\text{porous carbon nanofiber}$ hybrid films demonstrated a capacity of 97 mAh g⁻¹ at 1 C and superior cycling stability without observable capacity fading after 500 cycles [191]. High-rate performance of $\text{Na}_{2+2x}\text{Fe}_{2-x}(\text{SO}_4)_3@\text{rGO}$ was achieved with a high capacity of 78 mAh g⁻¹ at 60 C and 80.8% of capacity retention after 2000 cycles at 30 C [193].

2.1.6. Silicates

Due to the environmental sustainability, low cost, and possibility of multiple electrons reaction per unit formula, transition metal orthosilicates, Na_2MSiO_4 ($\text{M} = \text{Fe}, \text{Co}, \text{Mn}$), are also considered promising cathode materials for SIB applications. As the first reported material of this class used for sodium-storage, $\text{Na}_2\text{CoSiO}_4$ showed promise at a suitable operation potential of 3.3 V (vs. Na/Na^+) with a reversible capacity of 100 mAh g⁻¹ at a current rate of 5 mA g⁻¹ [195]. Corner-sharing alternate cobalt and silicate tetrahedral units built up the main skeleton of the crystalline structure, with sodium atoms stuffed into the tetrahedral vacant-sites. Two polymorphs, corresponding to monoclinic Si/Co ordered *Pc* and

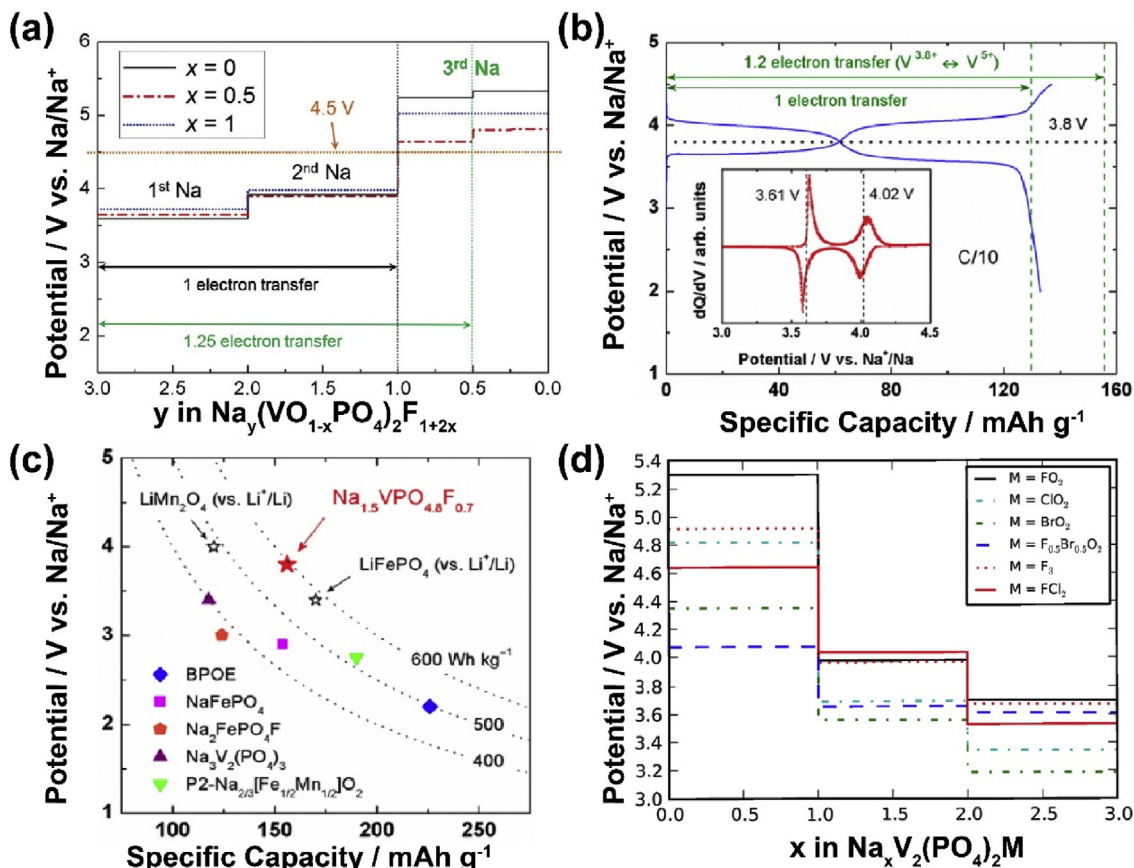


Fig. 9. (a) Potential–composition curves for $\text{Na}_y\text{V}_2(\text{PO}_4)_2\text{O}_{2-2x}\text{F}_{1+2x}$ ($0 \leq x \leq 1; 0 \leq y \leq 1$) materials on the basis of DFT calculations. Reproduced with permission [185]. Copyright 2014, Wiley-VCH. (b) Voltage–capacity curve for the $\text{Na}_3\text{V}_2\text{O}_{1.6}(\text{PO}_4)_2\text{F}_{1.4}$ electrode cycled at 0.1 C between 2.0 and 4.5 V vs. Na/Na^+ . The inset presents the corresponding dQ/dV profile. (c) Comparisons of energy density of different cathode materials for LIBs and SIBs. Reproduced with permission [186]. Copyright 2013, American Chemical Society. (d) Comparisons of voltage profiles of $\text{Na}_x\text{V}_2(\text{PO}_4)_2\text{M}$ ($0 \leq x \leq 3$) electrodes with different anion M substitution from first-principle calculations. Reproduced with permission [187]. Copyright 2014, American Chemical Society.

orthorhombic Co/Si disordered *Pbca* space groups, were identified. Na^+ diffusion in $\text{Na}_2\text{CoSiO}_4$ favors 3D network of pathways with low activation barriers, which suggest fast Na^+ insertion kinetics. Monoclinic-structured $\text{Na}_2\text{CoSiO}_4$ with *Pn* space group was also experimentally obtained by Rangasamy et al. through a facile solvothermal method [196]. Regardless of the enhanced electrochemical properties with incorporation of multiwalled carbon nanotubes, redox reaction mechanisms and the corresponding structural evolution process are still unknown and require more research efforts.

Manganese-based $\text{Na}_2\text{MnSiO}_4$, first reported as a precursor to prepare $\text{Li}_2\text{MnSiO}_4$ through ion-exchange, can be crystallized into monoclinic *Pn* structure and possesses polyanionic framework constituted by corner-sharing MnO_4 and SiO_4 tetrahedra [197]. More than 1 mol of Na ions intercalation per $\text{Na}_2\text{MnSiO}_4$ molecule was first realized in the $\text{Na}_2\text{MnSiO}_4/\text{C}/\text{rGo}$ composite with a particle size of 30–40 nm [198]. Due to intrinsic electronical insulation nature of silicates, however, the high initial discharge capacity of 182 mAh g^{-1} was hardly maintained during the following tens of cycles. Law et al. reported the highest-ever reversible capacity of 210 mAh g^{-1} of $\text{Na}_2\text{MnSiO}_4$ electrode among the polyanion-type compounds, as achieved via the interdependent effect of both the structural features of $\text{Na}_2\text{MnSiO}_4$ and the optimized electrolyte and additive mixture [199]. $\text{Mn}^{2+}/\text{Mn}^{3+}/\text{Mn}^{4+}$ was demonstrated as the active redox species during the charge/discharge process, involving 1.5 electrons transferring reaction. The electrolyte additive of vinylene carbonate (VC) could form a meta-stable passivation film on the surface of the $\text{Na}_2\text{MnSiO}_4$ electrode to reduce manganese dissolution, leading to the good electrochemical reversibility. Zhang et al. demonstrated a similar ion diffusion mechanism in $\text{Na}_2\text{MnSiO}_4$ and $\text{Li}_2\text{MnSiO}_4$ whatever the migratory ions choice of Na^+ or Li^+ based on the first-principles calculations. It was noted that faster Na^+ diffusion rate in $\text{Na}_2\text{MnSiO}_4$ than that of Li^+ in Li analog was identified, which was ascribed to the wider diffusion channels in $\text{Na}_2\text{MnSiO}_4$ than that in $\text{Li}_2\text{MnSiO}_4$ [200].

Similar to $\text{Li}_2\text{FeSiO}_4$ as the cathode material for LIB applications, $\text{Na}_2\text{FeSiO}_4$ has also gained extensive attentions as a novel electrode material for SIBs, because of the possibility of multi-electrons exchange with high theoretical capacity. $\text{Na}_2\text{FeSiO}_4$ was first obtained through electrochemical Li–Na ion-exchange from the Li counterpart, which showed a capacity as high as 330 mAh g^{-1} (calculated based on $\text{Li}_2\text{FeSiO}_4$) in the voltage range of 1.2–4.5 V [201]. A new cubic polymorph of $\text{Na}_2\text{FeSiO}_4$ with *F43m* space group, first synthesized by Yang's group through a sol–gel method, delivered a reversible capacity of 106 mAh g^{-1} within 1.5–4.0 V in a Na-ion cell [202]. This material demonstrated no appreciable cell volume change during the electrochemical reaction process due to its robust structural stability, as verified by the combination of *ex-situ* XRD and first-principles calculations. Better electrochemical results were gained for the carbon-coated $\text{Na}_2\text{FeSiO}_4$ with a particle size of 20–50 nm [203]. $\text{Na}_2\text{FeSiO}_4/\text{C}$ delivered a high discharge capacity of 181 mAh g^{-1} at a current rate of 27.6 mA g^{-1} with a stable cycling performance of 88% capacity retention after 100 cycles. Despite the satisfactory reversible capacity, the energy density of this kind of material is not supposed to be exceptionally high, resulting from the relatively low operation plateau at ~1.9 V corresponded to the $\text{Fe}^{2+}/\text{Fe}^{3+}$ redox reaction.

2.1.7. Amorphous polyanion compounds

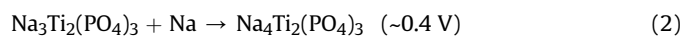
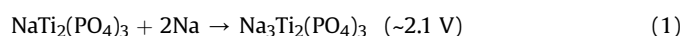
Compared to the crystalline electrodes, materials with amorphous structure are likely to provide improved structural stability and redox kinetic performance, owing to the less lattice limitation during Na^+ insertion/extraction and more facile diffusion paths in the disordered structure [204]. However, exploring suitable amorphous electrode materials for sodium-ion storage is still facing an

arduous challenge. Of particular interest is amorphous FePO_4 material, which promises a high theoretical capacity of 175 mAh g^{-1} . Shiratsuchi et al. first revealed the feasibility of Li and Na storage in both amorphous and crystalline FePO_4 using $\text{Fe}^{2+}/\text{Fe}^{3+}$ redox reaction [205]. Besides, amorphous FePO_4 was demonstrated as potential host for various charge carrier ions including cations like monovalent cations $\text{Li}^+/\text{Na}^+/\text{K}^+$, divalent cations $\text{Mg}^{2+}/\text{Zn}^{2+}$, or trivalent cations Al^{3+} . A combination of *ex situ* studies revealed the existence of a reversible disordered-to-ordered transformation induced by the electrochemical insertion/extraction, which appeared to contribute to the impressive sodium and potassium storage performance of amorphous FePO_4 [206]. Challenges of low electronic conductivity and sluggish ionic diffusion of amorphous FePO_4 are being addressed with various strategies such as conductive materials incorporation, nanoengineering, and morphology control [207–211]. Meanwhile, the detailed redox reaction mechanisms are still unclear, further research efforts need to be conducted to study the reaction characteristics using more sophisticated and convincing characteristic techniques.

2.2. Polyanion compounds as anode materials

2.2.1. NASICON $\text{NaTi}_2(\text{PO}_4)_3$

As another typical representative NASICON-type compound, $\text{NaTi}_2(\text{PO}_4)_3$, has attracted broad attention as the anode material for SIBs due to its attractive sodium-ion storage performance. As shown in Fig. 10a, rhombohedral $\text{NaTi}_2(\text{PO}_4)_3$ is characterized with $\text{R}\bar{3}\text{c}$ space group, exhibiting a 3D open framework via NASICON structure. Two TiO_6 octahedra interconnected with three PO_4 tetrahedra by corner-sharing all the oxygen atoms to form the strongly bonded “lantern” structural units $[\text{Ti}_2(\text{PO}_4)_3]$, leading to large interstitial positions for sodium ions. Two crystallographic sites to accommodate sodium ions: Na1 sites with 6-fold coordination located between every two TiO_6 octahedra along the *c*-axis, fully occupied; Na2 sites with 8-fold coordination with an occupancy of 2/3, corresponding to 6b (0,0,0) and 18e (x,0,1/4) Wyckoff position, respectively. At low Na contents in the lattice, sodium-ions could preferably occupy the Na1 sites; whereas during the electrochemical (de)intercalation of Na^+ ions in $\text{NaTi}_2(\text{PO}_4)_3$, sodium-ions actually occupy the octahedra Na2 sites [213]. Delmas et al. first introduced the feasibility of alkali-ion storage properties in $\text{ATi}_2(\text{PO}_4)_3$ (*A* = Li or Na) [214–216]. $\text{NaTi}_2(\text{PO}_4)_3$ presents a well-defined redox plateau at ~2.1 V (vs. Na/Na^+) with two Na^+ -ions reversible insertion/extraction through a two-phasic transition between $\text{NaTi}_2(\text{PO}_4)_3$ and $\text{Na}_3\text{Ti}_2(\text{PO}_4)_3$, delivering a theoretical capacity of 133 mAh g^{-1} . Most titanium-based NASICON-type materials operate on the $\text{Ti}^{4+}/\text{Ti}^{3+}$ redox reaction; however, Sengutuvan et al. proved the possibility of developing an electrode material based on the $\text{Ti}^{3+}/\text{Ti}^{2+}$ redox couple [212]. Triclinic $\text{Na}_3\text{Ti}_2(\text{PO}_4)_3$ not only can be oxidized into $\text{Na}_1\text{Ti}_2(\text{PO}_4)_3$, but also can be reduced to $\text{Na}_4\text{Ti}_2(\text{PO}_4)_3$, both being rhombohedral in structure, exhibiting two distinct redox plateaus at ~2.1 and ~0.4 V (vs. Na/Na^+), respectively (Fig. 10b). Enlarging the electrochemical window to the range of 0–3 V, a theoretical capacity as high as 200 mAh g^{-1} was achieved. The report showed two-step redox reactions expressed in Eqs. (1) and (2).



Compared to other anode materials for SIBs, such as hard carbon, transition-metal oxides, and chalcogenides, one of the highlights of $\text{NaTi}_2(\text{PO}_4)_3$ is being used as the electrode material for aqueous SIBs [217–219]. Park et al., in 2011 first reported the

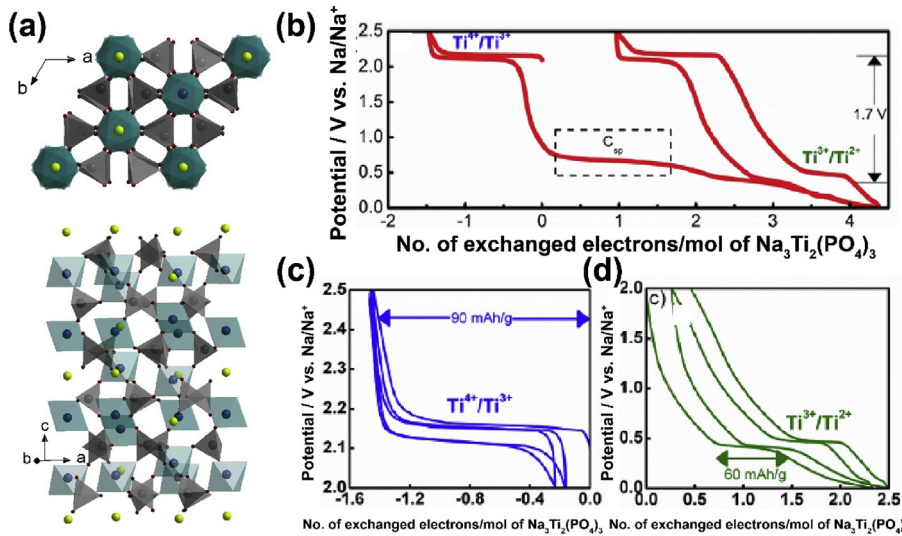


Fig. 10. (a) Crystal structure illustration of NASICON-type NaTi₂(PO₄)₃ viewing from different directions. Galvanostatic charge–discharge profiles of Na₃Ti₂(PO₄)₃ at C/25 between 0 and 2.5 V (b), 2.0–2.5 V (c), and 0–2.0 V (d) vs. Na/Na⁺, respectively. Reproduced with permission [212]. Copyright 2013, American Chemical Society.

electrochemical properties of NaTi₂(PO₄)₃ anode for rechargeable aqueous SIBs assembled with Zn, delivering a high capacity of 123 mAh g⁻¹ and exhibiting good cycling stability and rate performance [220]. NaTi₂(PO₄)₃ in aqueous systems shows fast ion diffusion and slight volume variation and is of low cost with environmental friendliness, all of which contribute to its potential commercialization. Though pioneering works have demonstrated various advantages of NaTi₂(PO₄)₃ in the field of aqueous and non-aqueous SIBs, the practical applications NaTi₂(PO₄)₃ are still limited by its poor rate capacity due to the low intrinsic electrical conductivity commonly found in phosphates.

2.2.2. Others

More interestingly, Na₃V₂(PO₄)₃ can serve as both cathode and anode material for SIBs, due to the unique structural feature of being capable of accepting a wide range of Na contents in the host framework. Variable valences in vanadium endows a series of redox couples: V⁵⁺/V⁴⁺, V⁴⁺/V³⁺, and V³⁺/V²⁺, which allows multi-electrons transfer in vanadium-based material. The redox reactions of V⁵⁺/V⁴⁺ and V⁴⁺/V³⁺ result in high voltage plateaus, whereas the potential of V³⁺/V²⁺ is relatively low that can be used for the cathodic process. Okada's and Yamada's group in 2010 introduced Na₃V₂(PO₄)₃ as the symmetrical electrode for a full Na-ion cell with ionic liquid electrolyte [221]. Jian et al. first reported that the carbon-coated Na₃V₂(PO₄)₃ electrode exhibited two flat potential plateaus at 3.4 V and 1.6 V vs. Na/Na⁺ in an organic electrolyte system, corresponding to the V⁴⁺/V³⁺ and V³⁺/V²⁺ redox couples, respectively [213]. Focusing on the cathodic process in the electrochemical window of 1.0–3.0 V, Na₃V₂(PO₄)₃ as an anode delivered a specific capacity of 93 mAh g⁻¹, corresponding to one more Na⁺ cation inserted into the Na₃V₂(PO₄)₃ lattice to form Na₄V₂(PO₄)₃. During a deep sodiation process by decreasing the voltage to 0.01 V, however, a new low-voltage plateau at ~0.3 V was shown up, indicating the fifth Na⁺-ion insertion into the Na₃V₂(PO₄)₃ lattice [222]. CV curves and the typical charge–discharge profiles are shown in Fig. 11a and b. Two well-defined redox couples for the cathodic reactions enabled Na₃V₂(PO₄)₃ anode delivering a specific capacity of ~150 mAh g⁻¹ (including the capacity contributions from the carbonaceous material, and the theoretical capacity is 117.6 mAh g⁻¹), indicating Na₃V₂(PO₄)₃ is a promising anode material for SIBs.

Jiao and his co-workers first reported NASICON-type NaZr₂(PO₄)₃ synthesized by a solid-phase method and demonstrated the possibility of Na⁺-ion-storage behavior of NaZr₂(PO₄)₃ for SIBs [223]. Similar to NaTi₂(PO₄)₃, the NaZr₂(PO₄)₃ framework consists of [Zr₂(PO₄)₃] lanterns built by ZrO₆ octahedra corner-sharing with PO₄ tetrahedra, and the Na⁺-ions distributed in the holes between ZrO₆ octahedra along the *c*-axis. Like other NASICON-type compounds, the 3D open and highly covalent-bonded structure leads to high Na⁺-ionic conductivity and strong structural stability. NaZr₂(PO₄)₃ delivered a discharge capacity of ~150 mAh g⁻¹ at 20 mA g⁻¹, attributed to approximately 2.8 mol Na ions reversibly inserted/extracted per NaZr₂(PO₄)₃ formula unit during the charge–discharge process, demonstrating the relevance of NaZr₂(PO₄)₃ as anode material for SIBs with fast redox kinetics and stable cycling performance (Fig. 11c).

Furthermore, other polyanion-type materials with low redox potentials, such as Na₂VTi(PO₄)₃ [224–226], Na₃VTi(PO₄)₃ [227], and Na₃MnTi(PO₄)₃ [228–230] are worthy of mention. NASICON-structured Na₂VTi(PO₄)₃ was introduced by Mason et al. and its electrochemical properties were evaluated in aqueous SIBs firstly [225]. Unfortunately, the working voltage and specific capacity were unsatisfied due to the redox limitation in aqueous system with only one Na⁺-ion per formula unit transport. Following that, Wang et al. demonstrated sodium-storage behavior in organic electrolyte system of carbon-coated Na₂VTi(PO₄)₃ synthesized by a sol–gel method [224]. As displayed in Fig. 11d, a stable specific capacity of ~150 mAh g⁻¹ was achieved between 1.5 and 4.5 V (vs. Na/Na⁺) at the current rate of 0.1 C. The initial discharging profile was featured by three step phase transition processes at 3.4, 2.1, and 1.6 V, owing to the stepwise reduction reaction of V⁴⁺/V³⁺, Ti⁴⁺/Ti³⁺, and V³⁺/V²⁺ redox couples, respectively. The low redox potential allows Na₂VTi(PO₄)₃ being capable of serving as both anode and cathode material for SIBs.

3. Na-ion full-cells fabrication with polyanion materials

By combining analysis of the crystal structure, electrochemical properties, and the sodium-storage mechanisms, polyanion-type compounds have been considered the potential high-performance electrode materials for SIBs because they are capable of providing stable structure during long cycling and fast

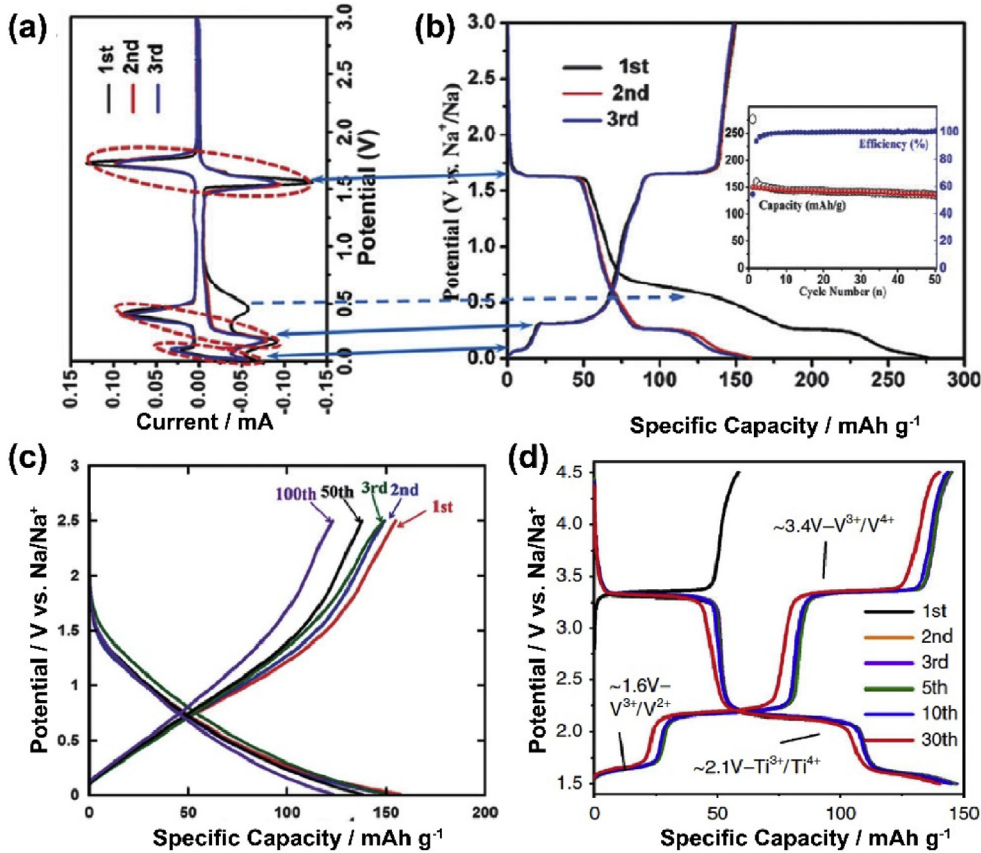


Fig. 11. CV curves (a) and typical charge–discharge profiles (b) of Na₃V₂(PO₄)₃ at 0.1 C in the voltage range of 0–3 V vs. Na/Na⁺. Inset of (b) shows the corresponding cycling performance. Reproduced with permission [222]. Copyright 2015, The Royal Society of Chemistry. (c) Charge–discharge profiles of NaZr₂(PO₄)₃ at a rate of 20 mA g⁻¹ between 0 and 2.5 V. Reproduced with permission [223]. Copyright 2014, The Royal Society of Chemistry. (d) Galvanostatic charge/discharge profiles of Na₂VTi(PO₄)₃ between 1.5 and 4.5 V vs. Na/Na⁺ at 0.1 C. Reproduced with permission [224]. Copyright 2017, Nature.

Na⁺ migration. Serving as cathode materials, they exhibit excellent cycling stability and relatively high operation potential. In the meantime, the major problem coming from the huge volume expansion haunted the anode materials, which can be feasibly solved by implementing the polyanion-type anodes owing to the negligible volume exchange during (de)insertion of Na⁺-ions. Polyanion-type materials offer good choices of cathode or anode materials for fabrication of Na-ion full-cells (NIFCs). In the next section, a brief summary about NIFCs constructed by polyanionic compounds as cathode or/and anode will be collected and analyzed, and some of the achievements are summarized in Table 2.

3.1. Na₃V₂(PO₄)₃ as the cathode material in Na-ion full-cells

NASICON-type Na₃V₂(PO₄)₃ (NVP) is famous for its fantastic electrochemical properties, thermal and structural stability, and relatively high voltage plateau (~3.4 V) for sodium-ion half-cells. To further explore the feasibility for practical applications of NVP cathodes, a wide variety of anode materials (e.g. carbonaceous materials, alloys, metal oxides, metal sulfides, etc.) matching with NVP were investigated in NIFCs. Particularly, hard carbon materials are promising anode materials because of their low cost, easy preparation, superior conductivity, and so on. For example, Ren et al. [232] reported a NIFC assembled with Na₃V₂(PO₄)₃ nanocomposite (NVP-NP) as cathode and poorly-graphitized hard carbon (HC) as anode (Fig. 12a–c). The NVP-NP//HC full-cell displayed a high average voltage of 3.3 V and the specific gravimetric energy reached up to 350 Wh kg⁻¹ based on the mass of cathode (258 Wh

kg⁻¹ based on the mass of both cathode and anode). Moreover, good cycling performance was obtained with a specific capacity of 60 mAh g⁻¹ after 100 cycles at 0.5 C, corresponding to 0.43% capacity decay per cycle. To further improve the electrochemical performance, Cao et al. [240] presented a new NIFC configuration, using graphene-encapsulated NVP nanoflakes arrays (NVP-NFs) as the cathode and 3D graphene-like material as the anode (Fig. 12d). The NVP-NFs//3D graphene cages full-cell delivered a high specific capacity of 109.2 mAh g⁻¹ at 0.1 A g⁻¹ with an average operating potential of 2.7 V (Fig. 12e) and maintained a good cycling stability (77.1% capacity retention over 200 cycles at 0.1 A g⁻¹).

In addition to carbonaceous materials, alloys-based anodes for SIBs are attracting more and more attention because of their high theoretical capacity, such as Sb delivering a high theoretical capacity of 660 mAh g⁻¹, and low potential relative to Na. Yang et al. [243] successfully assembled a NIFC coupling double-walled Sb@amorphous TiO_{2-x} nanotubes anode with NVP-C cathode, which showed outstanding electrochemical performance. It presented a capacity of 310 mAh g⁻¹ (based on the mass of anode) at 6.6 A g⁻¹ with an average working voltage of 2.5 V, and delivered energy density of 151 W h kg⁻¹ at 21 W kg⁻¹, even 61 W h kg⁻¹ at 1.83 kW kg⁻¹. Moreover, a graphene-scaffolded NVP microspheres//Sb–C full-cell delivered a high energy density of 242 Wh kg⁻¹ (based on the total mass of cathode and anode) at 0.1 C and showed excellent rate performance (power density of 4.56 kW kg⁻¹ at a high rate of 20 C) [247].

It should be noted that the insertion of Na⁺ into alloy-based anodes causes large volume expansion, which leads to the

Table 2

A summary of the electrochemical performance of the recently reported sodium-ion full-cells.

Full-cells (anode//cathode)	Voltage (V)	Energy density (Wh kg ⁻¹)	Electrolyte	Performance (current density, cycle, capacity retention)	Ref.
Hard carbon//NVP	~3	329	1 M NaClO ₄ /EC:PC(1:1 vol)+5%FEC	100 mA g ⁻¹ , 100, 67%	[231]
Hard carbon//NVP	3.3	258	1 M NaClO ₄ /EC:DMC(1:1 W)+5%FEC	0.5 C, 100, 57%	[232]
Hard carbon spheres//NVP/C nanocomposites	2.7	—	1 M NaFSI/PC	0.1 C, 80, 93%	[109]
Three-dimensional hard carbon matrix//NVP/C	1.6	—	1 M NaClO ₄ /PC	—, 50, 77.9%	[233]
N,O-codoped hard carbon//NVP	-2	53	1 M NaClO ₄ /EC:DEC(1:1 vol)+5wt%FEC	0.2 A g ⁻¹ , 800, —	[234]
Nitrogen-rich hierarchically porous carbon//NVP/C	—	—	1 M NaClO ₄ /EC:DMC(1:1 vol)	100 mA g ⁻¹ , 100, 95.3%	[235]
N, S co-doped porous carbon microtubes//NVP	—	—	1 M NaClO ₄ /EC:PC+5wt%FEC	50 mA g ⁻¹ , 50, —	[236]
Nitrogen-doped carbon sheets//NVP	3.5	—	1 M NaClO ₄ /EC:DEC(1:1 vol)+5%FEC	1.5 C, 200, 60.6%	[237]
2D ultrathin carbon nanosheets//NVP/C	—	—	1 M NaClO ₄ /EC:DEC(1:1 vol)+5%FEC	0.1 A g ⁻¹ , 100, —	[238]
Graphite//NVP	2.2	—	1 M NaCF ₃ SO ₃ /TGM	200 mA g ⁻¹ , 400, 80%	[239]
3D graphene//NVP	2.7	—	1 M NaClO ₄ /PC+5%FEC	0.1 A g ⁻¹ , 200, 77%	[240]
Porous graphite//NVP	2.54	130.7	1 M NaPF ₆ /DEC	100 mA g ⁻¹ , 500, 92%	[241]
Juglone/RGO//NVP	1.3	—	1 M NaClO ₄ /EC:DC(1:1 vol)	0.1 A g ⁻¹ , 100, —	[242]
Sb@TiO _{2-x} //NVP	2.5	151	1 M NaClO ₄ /EC:DEC(1:1 vol) or 1 M NaClO ₄ /PC+appropriate amount of FEC	100 mA g ⁻¹ , 20, —	[243]
Sb-C//NVP	2.6	—	0.6 M NaPF ₆ /EC:DMC(3:7 vol)	0.1 C, 50, 80%	[244]
Sb-O-G//NVP	2.7	160	1 M NaClO ₄ /EC:PC(1:1 vol)+5%FEC	1.5 C, 50, 77.8%	[245]
Sb/rGO//NVP/rGO	—	—	1 M NaClO ₄ /EC:DC(1:1 W)+5wt%FEC	—, 100, 83%	[246]
Sb/C//NVP@rGO	2.6	242	1 M NaClO ₄ /EC:DEC(1:1 vol)	0.5 C, 40, 78%	[247]
Sn//NVP/carbon nanotubes composites	-3.2	253.4	1 M NaPF ₆ /DEGDME	400 mA g ⁻¹ , 180, 96.1%	[248]
NiO-Ni//NVP	-2	—	1 M NaPF ₆ /EC:DEC:DMC(1:1:1)+5%FEC	200 mA g ⁻¹ , 50, —	[249]
Sb ₂ O ₃ @Sb//NVP	2.5	—	1 M NaClO ₄ /PC+5wt%FEC	0.5 A g ⁻¹ , 100, 93%	[250]
Fe ₂ O ₃ -alginate//NVP	1.6	—	1 M NaClO ₄ /PC	0.2 C, 20, 65%	[251]
MoO ₃ //NVP	1.4	—	1 M NaClO ₄ /EC:PC	—, —, —	[252]
2NiO//Fe ₂ O ₃ //NVP	1.8	150	1 M NaClO ₄ /PC+2%FEC	—, 30, —	[253]
V ₂ O ₃ //NVP@C	—	—	1 M NaClO ₄ /PC	—, 150, 52%	[254]
C@TiO ₂ //NVP	2	440	1 M NaPF ₆ /DGM	50 mA g ⁻¹ , 35, 67%	[255]
Nb ₂ O ₅ //NVP	—	—	1 M NaClO ₄ /EC:PC(1:1 vol)+5%FEC	10 C, 500, —	[256]
Mesoporous Nb ₂ O ₅ nanosheets//NVP	—	—	1 M NaClO ₄ /EC:DMC(1:1 vol)+5%FEC	50 mA g ⁻¹ , 30, —	[257]
Ni ₃ S ₂ /C//NVP	1.7	—	1 M NaClO ₄ /EC:DEC:FEC(1:1:0.05 vol)	0.5 A g ⁻¹ , 30, 60%	[258]
Fe ₃ S ₄ //NVP@C@rGO	1.7	—	1 M NaClO ₄ /PC+5%FEC	100 mA g ⁻¹ , —, —	[259]
VS ₂ stacked nanosheets//NVP	1.5	—	1 M NaSO ₃ CF ₃ /DGM	0.2 A g ⁻¹ , 50, —	[260]
CoS@rGO//NVP@C	-2	92	1 M NaSO ₃ CF ₃ /EC:DEC or 1 M NaSO ₃ CF ₃ /PC	0.5 A g ⁻¹ , 100, 76%	[261]
7-CoS/C//NVP	—	—	NaSO ₃ CF ₃ /DGM	0.5 A g ⁻¹ , 100, 95.6%	[262]
NiS-Ni//NVP	—	—	1 M NaPF ₆ /EC:DEC:DMC(1:1:1 vol)+5%FEC	50 mA g ⁻¹ , 100, —	[263]
Bi ₂ S ₃ //NVP	1.6	—	1 M NaClO ₄ /PC+5%FEC	—, —, —	[264]
SnS ₂ //NVP	~1.6	—	1 M NaClO ₄ /PC+5%FEC	—, 12, 66.9%	[265]
Co _{0.5} Fe _{0.5} S ₂ //NVP	1.6	—	NaCF ₃ SO ₃ /DGM	—, 100, 90.2%	[266]
MoS ₃ //NVP	1.8	—	1 M NaClO ₄ /EC:DEC(1:1 vol)+8 vol%FEC	0.83 C, 100, 84%	[267]
CoS@ bowl-like hollow carbon spheres//NVP	—	136	1 M NaCF ₃ SO ₃ /DGM	500 mA g ⁻¹ , 70, 90%	[268]
SnS/C fibers//NVP/C	—	223	1 M NaClO ₄ /PC+5%FEC	200 mA g ⁻¹ , 500, 74.6%	[269]
MoS ₂ /carbon framework//NVP	—	52	1 M NaCF ₃ SO ₃ /DGM	0.5 A g ⁻¹ , 40, —	[270]
MoSe ₂ /N,P-rGO//NVP	~1.8	114	1 M NaClO ₄ /EC:DEC(1:1 vol)+5wt%FEC	0.5 A g ⁻¹ , 200, 80%	[271]
FeSe ₂ //NVP	1.7	—	1 M NaSO ₃ CF ₃ /DEGDME	1 A g ⁻¹ , 200, 81%	[272]
CoSe ₂ //NVP	1.1	—	1 M NaSO ₃ CF ₃ /DEGDME	—, 50, 80.7%	[273]
ZnSe@hollow carbon nanospheres//NVP	—	—	1 M NaSO ₃ CF ₃ /DEGDME	0.5 A g ⁻¹ , 100, —	[274]
FeP nanorod arrays/Ti//NVP	—	185	1 M NaClO ₄ /EC:DEC(1:1 vol)	1 C, 200, —	[275]
GeP ₃ /C//NVP	2.65	—	1 M NaClO ₄ /EC:DEC(1:1 vol)	—, 60, ~80%	[276]
Cu ₃ P nanowire//NVP	—	104.5	1 M NaClO ₄ /EC:DC+5%FEC	600 mA g ⁻¹ , 200, —	[277]
Three-dimensional (3D) porous Cu//NVP	—	—	1 M NaPF ₆ /DEGDME	1 C, 100, 90.1%	[278]
Na ₄ V ₂ (PO ₄) ₃ //NVP	3	138	1 M NaClO ₄ /EC:DC(1:1 W)+5%FEC	40 mA g ⁻¹ , 100, 87%	[279]
Carbon//NVPF	—	451	1 M NaPF ₆ /PC	0.1 C, 100, 95%	[280]
RHHC-1300//NVPF/C	3.4	185	1 M NaClO ₄ /EC:DC(1:1 vol)	100 mA g ⁻¹ , 100, 85%	[281]
SnSb alloy//NVPF	~3.2	—	1 M NaPF ₆ /EC:DEC(1:1 vol)	—, 100, 70%	[282]
SnS/G + C//NVPF	—	—	1 M NaPF ₆ /EC:DEC(1:1 vol)	0.2 mA cm ⁻² , 100, —	[283]
Ni _{1.5} CoSe ₃ @NC@rGO//Na ₃ V ₂ (PO ₄) ₂ O ₂ F	294	—	1 M NaClO ₄ /EC:PC+5wt%FEC	0.5 A g ⁻¹ , 35, 94.4%	[284]
Red P@C//NVPF/C	~ 3.65	161.8	1 M NaClO ₄ /PC+5 vol%FEC	1000 mA g ⁻¹ , 100, 82.3%	[285]
Naphthalene-based dicarboxylate//Na ₃ V ₂ O ₂ (PO ₄) ₂ F/ rGO	3.2	—	1 M NaClO ₄ /PC	—, 20, —	[286]
NTP//Ni _{0.3} Co _{0.7} [Fe(CN) ₆] Prussian blue analogues	—	—	1 M NaClO ₄ /EC:DC(1:1 vol)+2wt%FEC	150 mA g ⁻¹ , 300, —	[287]
F-doped NTP/C//nickel hexacyanoferrate	—	—	1 M NaClO ₄ /EC:DEC(1:1 vol)+2wt%FEC	1330 mA g ⁻¹ , 1000, ~70%	[288]
NTP//Ag	—	—	1 M NaCl in DI water	1000 mA g ⁻¹ , 200, —	[289]
NTP//Ag	—	49.9	1 M NaCl aqueous	10 C, 1500, 70%	[290]
NTP//Na _{0.66} [Mn _{0.66} Ti _{0.34}]O ₂	1.2	—	1 M Na ₂ SO ₄ in DI water	2 C, 300, 89%	[291]
NVP//NVP	1.8	—	Solid electrolyte Na ₃ Zr ₂ Si ₂ PO ₁₂	1.2 μA cm ⁻² , —, 58%	[292]
NVP//NVP	1.8	1.87 × 10 ⁻³ Wh cm ⁻²	Solid electrolyte Na ₃ Zr ₂ Si ₂ PO ₁₂	0.1 C, —, 85%	[293]
NVP//NVP	1.75	185.5	1 M NaClO ₄ /EC:DMC(1:2 W)	1 C, 200, —	[261]
Porous NVP coated with carbon//porous NVP coated with carbon	—	—	1 M NaClO ₄ /PC+2%FEC	5 C, 500, 61%	[294]
NVP@C//NVP@C	1.7	155	1 M NaClO ₄ /PC	2 C, 50, 81%	[295]
NVP/C nanofiber//NVP/C nanofiber	1.5	92	1 M NaClO ₄ /EC:PC(1:1 vol)	100 mA g ⁻¹ , 300, 44%	[296]

Table 2 (continued)

Full-cells (anode//cathode)	Voltage (V)	Energy density (Wh kg ⁻¹)	Electrolyte	Performance (current density, cycle, capacity retention)	Ref.
NVP:rGO-CNT//NVP:rGO-CNT	1.7	150	1 M NaClO ₄ /PC+5%FEC	10 C, 100, 77%	[297]
NVP/elastic carbon foam//NVP/elastic carbon foam	1.8	162	1 M NaClO ₄ /EC:DC(1:1 W)+5wt%FEC	2 C, 280, 81%	[298]
NTP//NVP	~1.25	90	1 M NaClO ₄ /EC:DMC(1:1 W)+5%FEC	5 C, 300, 97%	[299]
NTP//NVP	—	—	1 M NaClO ₄ /EC:PC(1:1 vol)	5 C, —, —	[300]
NTP@C//NVP	~1.3	94	1 M NaClO ₄ /EC:DMC(1:1 vol)+5wt%FEC	1 C, 100, 90%	[301]
NTP/carbon nanotube fabrics//NVP/carbon nanotube fabrics	1.3	—	1 M NaPF ₆ /EC:PC(1:1 vol)	20 C, 4000, 74.5%	[302]
NTP–multiwalled carbon nanotube//NVPF-single walled carbon nanotube	1.92	150	1 M NaPF ₆ /PC+5 vol%FEC and 17 M NaClO ₄ aqueous	1 C, 20, 74%	[303]
NTP@GO//NVP/C	1.2	73	1 M NaClO ₄ /EC:DEC(1:1 vol)	10 C, 1000, 80%	[304]
NTP@C//NVPF@C	—	—	1 M NaClO ₄ /EC:PC(1:1 vol)+5%FEC	10 C, 1000, 71%	[305]
NTP//Na ₃ V ₂ O ₂ (PO ₄) ₂ F	1.7	—	1 M NaClO ₄ /PC+2%FEC	2 C, 1800, —	[306]

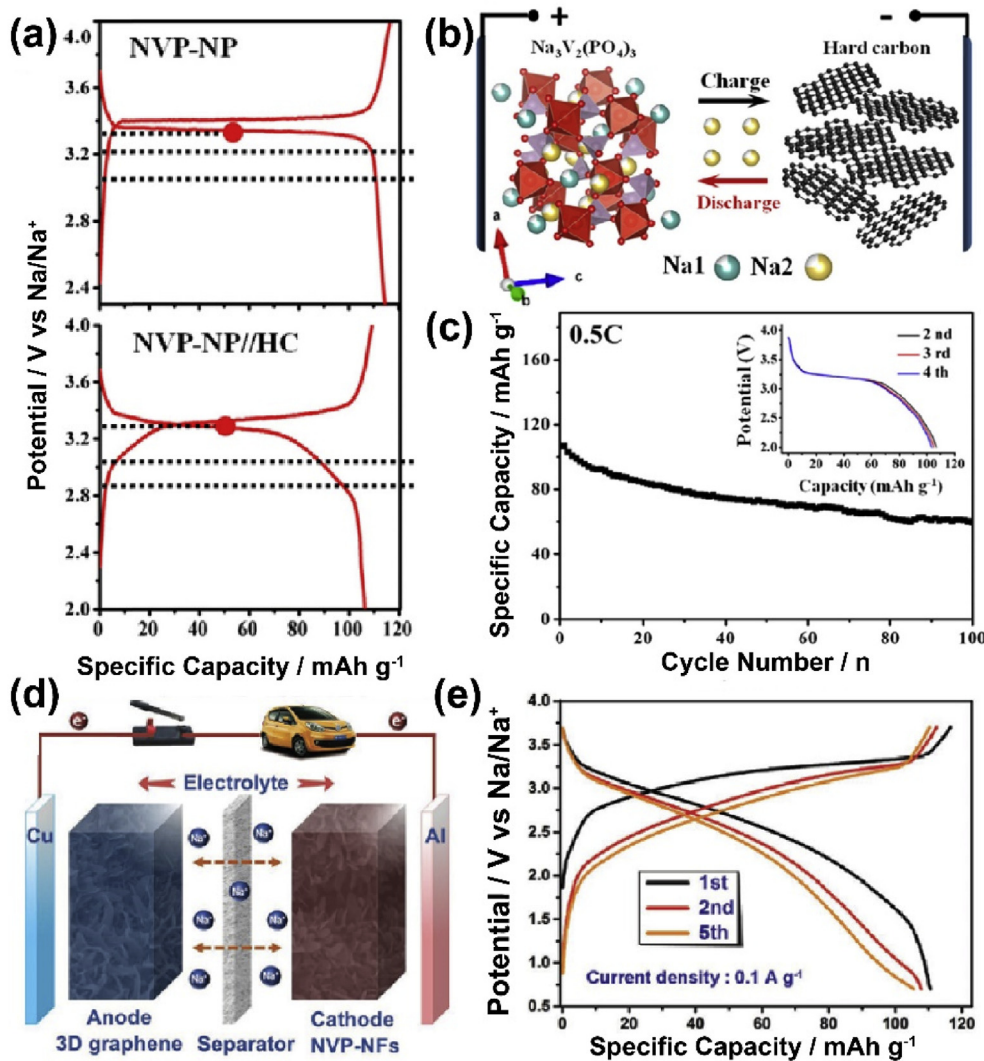


Fig. 12. (a) The second charge/discharge curves of NVP-NP and NVP-NP//HC at 0.2 C. Schematic diagram (b) and the cycling performance at 0.5 C (c) of the NVP-NP//HC NIFC. Reproduced with permission [232]. Copyright 2016, Elsevier. Schematic illustration (d) and galvanostatic charge/discharge profiles between 0.7 and 3.7 V at 0.1 A g⁻¹ (e) of the NVP-NFs//3D graphene cages NIFC. Reproduced with permission [240]. Copyright 2017, Wiley-VCH.

pulverization of electrode materials and rapid deteriorations of anodic performances. Considering this, metal oxides have emerged as potential candidates of SIB anodes. A novel NVP//Nb₂O₅ NIFC showed favorable electrochemical properties with a stable capacity

of 105 mAh g⁻¹ after 500 cycles at 10 C (based on the weight of anode) between 1.2 and 3.5 V [256]. Besides, mesoporous Nb₂O₅ nanosheets as an anode material for SIBs was scalably fabricated via a simple nanocasting approach and then applied for the NIFC. The

designed NVP//mesoporous Nb_2O_5 nanosheets NIFC displayed a relatively high reversible capacity of 244 mAh g^{-1} at 50 mA g^{-1} and nice high-rate capability [257]. In addition, titanium dioxide (TiO_2) possesses combined merits of good chemical stability, negligible strain during electrochemical cycling, low cost, and environment friendliness and thus has been extensively studied recently for SIB applications. Gregorio et al. [255] demonstrated a high-energy NIFC consisting of TiO_2 anode coupling with a NVP cathode. The NVP// TiO_2 NIFC delivered an average potential voltage at 2.0 V with a reversible capacity of 220 mAh g^{-1} , featuring the energy density as high as 440 Wh kg^{-1} .

Among various anode materials for SIBs, transition metal sulfides/selenides have emerged as promising candidates because of their earth abundance, low cost, and high theoretical capacities. High-performance Fe_3S_4 nanosheet anode coupling with NVP@C@rGO cathode (NVP@C@rGO// Fe_3S_4 NIFC) exhibited a highly reversible capacity of $\sim 305 \text{ mAh g}^{-1}$ (based on the weight of anode) at a current density of 100 mA g^{-1} with an average output voltage of about 1.7 V [259]. With comparison of hard carbon as the anode material assembled NVP@C@rGO//HC NIFC, NVP@C@rGO// Fe_3S_4 NIFC showed higher reversible capacity and much better rate capability, indicating more superior potential of NVP@C@rGO// Fe_3S_4 NIFC for practical applications. FeSe_2 microspheres assembled by numerous nanoctahedra used as the anode material were paired with NVP cathode [272]. A high discharge capacity of 366 mAh g^{-1} (based on the anode mass) at 1 A g^{-1} was achieved for the NVP// FeSe_2 NIFC with an output voltage of about 1.7 V . It also demonstrated good cycling stability, remaining 81.4% of capacity retention after 200 cycles. Many creative strategies were explored to further improve the electronic conductivities of the transition metal chalcogenides, such as carbon coating, surface engineering, and lattice doping. Mai's group [262] fabricated ultrafine CoS nanoparticles embedded in porous carbon nanorods (denoted as 7-CoS/C) via *in-situ* carbonization and sulfidation of Co-metal organic frameworks (Co-MOF). After being coupled with NVP, the NVP//7-CoS/C NIFC delivered a high reversible capacity of 368 mAh g^{-1} at 0.5 A g^{-1} (based on the mass of 7-CoS/C) (Fig. 13a). After 100 cycles, the discharge capacity maintained 352 mAh g^{-1} with the capacity retention of 95.6% , exhibiting excellent cycling performance (Fig. 13b). Peng et al. [261] developed a NIFC based on CoS@rGO hybrid anode and electrospun NVP@C cathode, displaying initial charge/discharge capacities of 498 and 381 mAh g^{-1} (based on the mass of anode) and delivering the energy density of 92 Wh kg^{-1} . A NiS–Ni freestanding anode matching with the NVP cathode, the NVP//NiS–Ni NIFC showed excellent cycling performance with charge and discharge capacities of 172.8 and 163.5 mAh g^{-1} after 100 cycles at a current density of 0.05 A g^{-1} [263]. Furthermore, Niu et al. [271] assembled NVP/C cathode with MoSe₂-covered N,P-doped carbon nanosheet (MoSe₂/N,P-rGO) anode, which showed a capacity of 276 mAh g^{-1} after 200 cycles at 0.5 A g^{-1} , corresponding to a capacity retention of 80% . The NVP/C//MoSe₂/N,P-rGO NIFC demonstrated high rate capability (Fig. 13c) and high energy density (113.6 Wh kg^{-1} total at 0.1 kW kg^{-1} , even 57.6 Wh kg^{-1} total still achieved at 1.68 kW kg^{-1}) (Fig. 13d).

Based on the above results, it is not hard to find that the energy density of NIFCs based on metal oxides and metal sulfides/selenides is strongly limited by their high operation voltage and huge initial capacity irreversibility, thus further hindering their practical applications for large-scale energy storage.

3.2. $\text{Na}_3\text{V}_2(\text{PO}_4)_2\text{F}_3/\text{Na}_3\text{V}_2\text{O}_2(\text{PO}_4)_2\text{F}$ as the cathode material in Na-ion full-cells

Compared with $\text{Na}_3\text{V}_2(\text{PO}_4)_3$, fluorophosphates $\text{Na}_3\text{V}_2(\text{PO}_4)_2\text{F}_3/\text{Na}_3\text{V}_2\text{O}_2(\text{PO}_4)_2\text{F}$ show higher redox potentials for de-/sodiation

owing to the lattice adoption of electronegative atoms of F [307] and therefore improve the energy density of the NIFCs mentioned above. Okada et al. [283] confirmed the feasibility of $\text{Na}_3\text{V}_2(\text{PO}_4)_2\text{F}_3$ cathode in a NIFC configuration using SnS/G + C as the anode. The $\text{Na}_3\text{V}_2(\text{PO}_4)_2\text{F}_3/\text{SnS/G} + \text{C}$ NIFC showed good electrochemical performance with high initial charge/discharge capacities of $504/319 \text{ mAh g}^{-1}$ and high output potential over 2.5 V . Furthermore, Liu et al. [285] synthesized the $\text{Na}_3\text{V}_2(\text{PO}_4)_2\text{F}_3/\text{C}/\text{red P@C}$ NIFC, which delivered an initial reversible capacity of 847.8 mAh g^{-1} based on the mass of anode red P@C at 1 A g^{-1} and showed a high average output voltage of $\sim 3.65 \text{ V}$. An outstanding energy density was achieved as high as 161.8 Wh kg^{-1} (Fig. 14a) based on the total mass of the battery. After 100 cycles, the reversible capacity remained 698.2 mAh g^{-1} at 1000 mA g^{-1} , showing a high capacity retention (82.3%) with high CE above 99% (Fig. 14b). Wang et al. [281] presented that $\text{Na}_3\text{V}_2(\text{PO}_4)_2\text{F}_3/\text{C}/\text{rice husk-derived hard carbons (RHHCs)}$ NIFC exhibited a stable capacity of 258 mAh g^{-1} after the activation cycles and an average output voltage of 3.4 V at 25 mA g^{-1} between 1.6 and 4.3 V . It also demonstrated good rate capability with a high specific capacity of 173 mAh g^{-1} even at 100 mA g^{-1} and remarkable cycling stability with a 85% capacity retention after 100 cycles. The energy density of this NIFC based on the total mass of cathode and anode active materials was calculated to be 185 Wh kg^{-1} . Moreover, Wang et al. [308] reported a NIFC consisting of amorphous selenium coated on 3D reduced graphene oxide (3DSG) as the anode and $\text{Na}_3\text{V}_2(\text{PO}_4)_2\text{O}_2\text{F}$ as the cathode (Fig. 14c), which delivered a high energy density of up to 313 Wh kg^{-1} at a power density of 51 W kg^{-1} and showed an outstanding rate performance owing to the fast electrochemical reaction kinetics of both cathode and anode in the whole current density range from 0.02 to 4 A g^{-1} (Fig. 14d). Wu et al. [284] presented a NIFC configuration consisting of double transition metal selenide $\text{Ni}_{1.5}\text{CoSe}_5$ nanoaggregates in 3D N-doped carbon network (abbreviated as $\text{Ni}_{1.5}\text{CoSe}_5@\text{NC@rGO}$) anode with $\text{Na}_3\text{V}_2(\text{PO}_4)_2\text{O}_2\text{F}$, which delivered a high energy density of up to 294 Wh kg^{-1} at 49.8 W kg^{-1} and capacity retention of above 94.4% after 35 cycles at 0.5 A g^{-1} .

3.3. $\text{NaTi}_2(\text{PO}_4)_3$ as the anode material in Na-ion full-cells

Due to the suitable theoretical capacity (133 mAh g^{-1}), high Na^+ ion conductivity, negligible volume change during cycling, as well as safety, low cost, and environmental benignity characteristics, NASICON-type $\text{NaTi}_2(\text{PO}_4)_3$ (NTP) with a sodium insertion reaction mechanism has attracted much attention as anode for SIBs. The electrochemical studies of NTP served as the anodes in NIFCs systems were widely conducted in last few years. Han's [287] group presented a NIFC consisting of high-quality $\text{Ni}_{0.3}\text{Co}_{0.7}[\text{Fe}(\text{CN})_6]$ Prussian blue analogues (PBAs) (HQ-NiCoFe) as the cathode and NTP as the anode, which showed a high initial discharge capacity of 125.6 mAh g^{-1} at a current density of 15 mA g^{-1} (calculated on the mass of HQ-NiCoFe electrode) and excellent rate performance (the specific capacities remained nearly 90 and 60 mAh g^{-1} at 750 and 1500 mA g^{-1} , respectively). Meanwhile, the NIFC showed good cyclability without noticeable capacity fading over 300 cycles under a current density of 150 mA g^{-1} . The nickel hexacyanoferrate//F-doped $\text{NaTi}_2(\text{PO}_4)_3/\text{C}$ NIFC [288] also demonstrated exciting electrochemical behaviors, exhibiting suitable discharge capacities of $\sim 116 \text{ mAh g}^{-1}$ at a current density of 66.5 mA g^{-1} , outstanding rate capability (remained high reversible capacity of 96.98 mAh g^{-1} even at a current density of 1330 mA g^{-1}) and stable cycling performance (maintained $\sim 70\%$ capacity retention).

Compared with non-aqueous SIBs, aqueous SIBs also have attracted much attention due to lower cost and lower toxicity. Chen et al. [289] fabricated an aqueous sodium-ion full-cell (ANIFC)

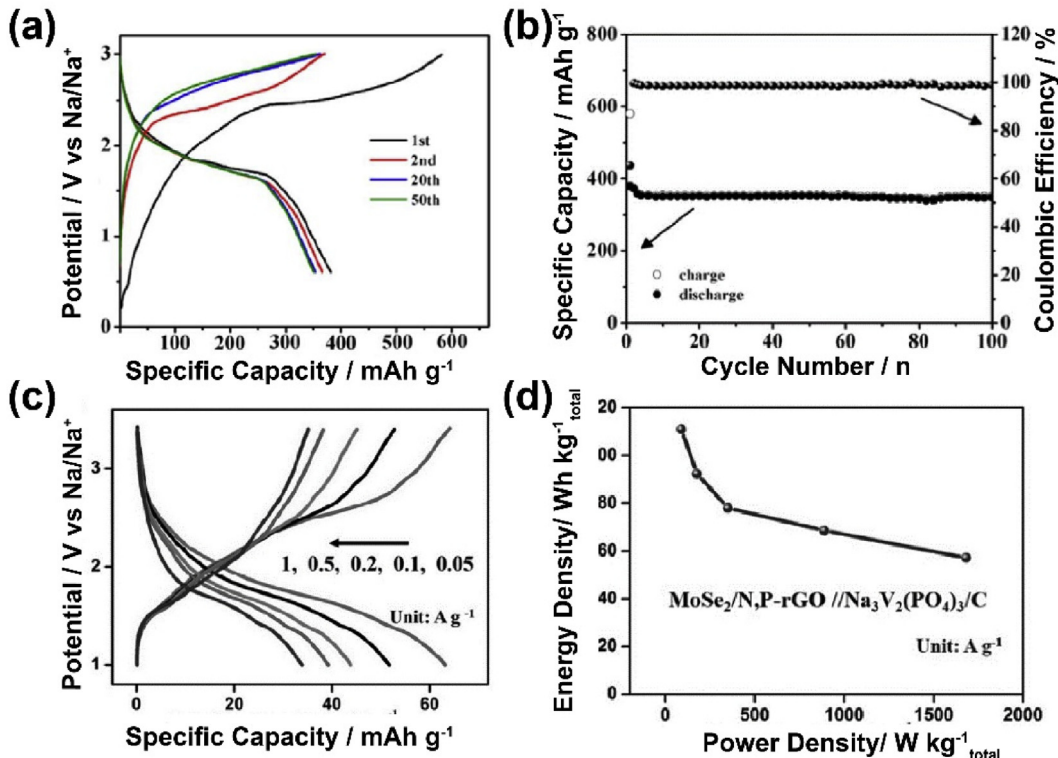


Fig. 13. The charge/discharge curves (a) and cycling performance (b) of NVP//7-CoS/C NIFC at 0.5 A g^{-1} . Reproduced with permission [262]. Copyright 2017, Elsevier. The charge/discharge curves at different rates (c) and the corresponding power and energy densities (d) of the NVP/C//MoSe₂/N,P-rGO NIFC. Reproduced with permission [271]. Copyright 2017, Wiley-VCH.

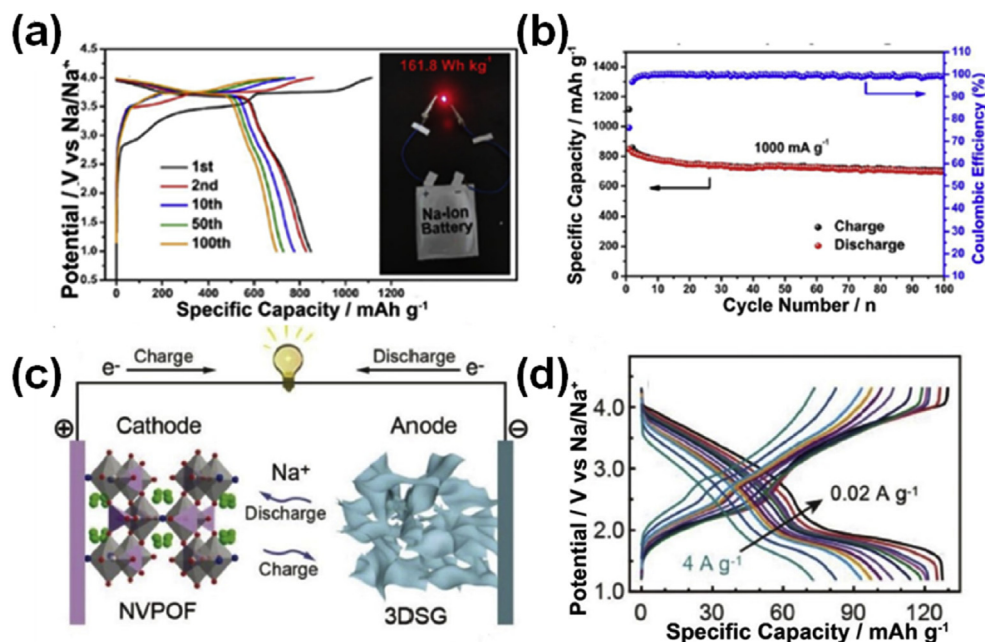


Fig. 14. The charge/discharge curves (a) and cycling performance (b) of Al-plastic film soft package NIFC with red P@C and Na₃V₂(PO₄)₂F₃/C electrodes (inset) tested in the voltage window of 1.0–4.0 V at 1 A g^{-1} . Reproduced with permission [285]. Copyright 2017, Elsevier. The schematic diagram (c) and galvanostatic charge–discharge curves (d) of the NVPOF//3DSG NIFC. Reproduced with permission [308]. Copyright 2018, Wiley-VCH.

constructed by NTP anode, silver cathode, and 1 M NaCl solution as an aqueous electrolyte in an open environment. The obtained ANIFC exhibited a reversible capacity of 37.4 mAh g^{-1} at a current

density of 1000 mA g^{-1} and maintained excellent cycling stability for 200 cycles without obvious capacity decay. The NaTi₂(PO₄)₃//Na_{0.66}[Mn_{0.66}Ti_{0.34}]O₂ ANIFC, reported by Hu et al. [291],

demonstrated an outstanding reversible capacity of $\sim 76 \text{ mAh g}^{-1}$ at a current rate of 2 C with an average operating voltage of 1.2 V, which is the highest-ever among all reported positive electrodes for aqueous SIBs till then. Furthermore, the full-cell exhibited excellent rate performance with high specific capacity of $\sim 54 \text{ mAh g}^{-1}$ at 10 C and stable cycling behaviors over 300 cycles with capacity retention of 89% at a current rate of 2 C.

3.4. Symmetric NASICON-type Na-ion full-cells

The symmetric NIFCs, using the same active materials for both the cathode and anode, are very attractive and promising from a commercial application point of view, processing several important merits in terms of being capable of buffering large volume expansion, tolerant of cell overcharge to some extent, cost saving, and simplifying the manufacturing process. As illustrated in Sections 2.1.2 and 2.2.2, NVP shows unique structural characteristics of being capable of acting both as cathode and anode materials owing to the versatility of vanadium redox couples. At the beginning of the study on NVP, one more Na^+ ion was found to be reversibly inserted/extracted into/from the NVP lattice, exhibiting a voltage plateau at around 1.6 V vs. Na^+/Na based on the redox couple of $\text{V}^{3+}/\text{V}^{2+}$. The electrochemical performance of the symmetric NVP//NVP NIFC was firstly evaluated by Mai's group [309]. As expected from the respective of 1.6 V and 3.4 V, the combination of NVP/AC as both anode and cathode gave rise to a NIFC operating around 1.75 V. Moreover, the symmetric NVP//NVP NIFC exhibited a long cycle life with approximately 80% of capacity retention after 200 cycles at 1 C. According to the calculation on the basis of the cathode, the specific energy of this symmetric NVP//NVP NIFC achieved as high as 185.5 Wh kg^{-1} , and remarkably, it could deliver a specific power of $\sim 5000 \text{ W kg}^{-1}$.

The demonstrated symmetric NVP//NVP NIFC performance provides great opportunities to outclass other competitor systems for operating in the fields of energy storage and transition and thus triggers intensive research interests in this battery system. Zhang et al. [298] employed $\text{Na}_3\text{V}_2(\text{PO}_4)_3$ /elastic carbon foam (NVP/ECF) to construct a symmetric full-cell with a discharge capacity of 107.8 mAh g^{-1} at a voltage plateau at 1.79 V, corresponding to the energy density of 162 Wh kg^{-1} based on the total mass of the electrodes. To further improve the electrochemical performance, Yu's group [297] constructed the symmetric NIFC using 3D tricontinuous NVP:rGO-CNT material, delivering a high rate capability with a reversible capacity of $\approx 90 \text{ mA h g}^{-1}$ at 10 C.

However, the intercalation of the fourth Na^+ -ion strongly limits on the capacity utilization of the NVP anode and the working voltage window of the symmetric NIFC. Encouragingly, the fifth Na^+ -ion insertion into the NVP lattice produced a lower redox potential at $\sim 0.3 \text{ V}$, doubling the theoretical capacity of the NVP anode to 117.6 mAh g^{-1} . Zhao et al. [310] firstly reported a symmetric NIFC with Ca-doped $\text{Na}_3\text{V}_{1.95}\text{Ca}_{0.05}(\text{PO}_4)_3@\text{C}$ as both electrodes exhibiting a high output voltage over 3 V (Fig. 15a and b). Through controlling of the electrochemical window of 1–4 V, the low sodiation voltage potential could be fully utilized and therefore greatly enhanced the energy density of the battery. The $\text{Na}_3\text{V}_{1.95}\text{Ca}_{0.05}(\text{PO}_4)_3@\text{C}/\text{Na}_3\text{V}_{1.95}\text{Ca}_{0.05}(\text{PO}_4)_3@\text{C}$ NIFC delivered a high gravimetric energy of 166 Wh kg^{-1} at 0.5 C (based on the total weights of both cathode and anode), and maintained 73% of energy density at a high rate of 20 C. Moreover, benefited from the stable lattice structure owing to Ca-doping, the symmetric NIFC manifested outstanding rate performance (Fig. 15c) and very high cycling stability (0.02% capacity decay per cycle for 2000 cycles at 10 C, Fig. 15d), outputting all of the NVP-based and metal oxides-based electrodes symmetric NIFCs.

On the other hand, Noguchi et al. [292] assembled an all solid-state Na-ion symmetrical battery with NVP as the electrodes and $\text{Na}_3\text{Zr}_2\text{Si}_2\text{PO}_{12}$ (NASICON) as the solid electrolyte. The fabricated symmetric battery examined at room temperature offered a relatively flat discharge voltage of 1.8 V and 80% of the discharge capacity for the equivalent liquid symmetric cell. Furthermore, all solid-state NVP| $\text{Na}_3\text{Zr}_2\text{Si}_2\text{PO}_{12}$ |NVP NIFC operated at high temperature (200°C) demonstrated high electrochemical reversibility, showing 85% of the theoretical capacity at C/10 at 1.8 V, with an overall energy density of $1.87 \times 10^{-3} \text{ Wh cm}^{-2}$ and a capacity of 1.04 mAh cm^{-2} [293].

3.5. Two kinds of polyanionic compounds as anode and cathode materials in Na-ion full-cells

To further explore the practical applications of NASICON-type full-cells, different materials as cathode and anode were assembled to obtain high-performance and high-energy Na-ion full batteries. For example, Mai's group [299] reported a full-cell consisting of three-dimensional $\text{Na}_3\text{V}_2(\text{PO}_4)_3$ nanofiber as cathode and $\text{NaTi}_2(\text{PO}_4)_3$ as anode, which showed outstanding cycling stability (96.9% capacity retention over 300 cycles at 5 C) and superior rate capability (80 mAh g^{-1} at 50 C). More importantly, the energy density reached up to 90 Wh kg^{-1} at a power density as high as 6 kW kg^{-1} , which is ascribed to the 3D nanofiber network structure providing multichannel ionic diffusion pathway, continuous electronic conduction, and improved structural integrity. A full-cell consisting of $\text{NaTi}_2(\text{PO}_4)_3@\text{C}$ as the anode and $\text{Na}_3\text{V}_2(\text{PO}_4)_3@\text{C}$ on carbon cloth as the cathode was reported by Cao's group [301]. This full-cell showed outstanding sodium storage performance, such as the initial discharge capacity is 104.7 mAh g^{-1} based on the cathode mass, with an initial Coulombic efficiency as high as 90.2% with the voltage window in the range of 0.7–2.4 V at 1 C. Furthermore, even at an ultrahigh rate of 50 C, the power density (based on the mass of NVP@C) is as high as 8.4 kW kg^{-1} with an energy density of 94 Wh kg^{-1} . In particular, it exhibited an energy density as high as 396 Wh kg^{-1} at a power density as high as 97 kW kg^{-1} with high mass loading of the NVP@C-CC electrode. Yu et al. [302] presented a full-cell of $\text{NaTi}_2(\text{PO}_4)_3$ /carbon nanotube fabrics (NTP/CNFs) as anode and a $\text{Na}_3\text{V}_2(\text{PO}_4)_3$ /carbon nanotube fabrics (NVP/CNFs) as cathode, which exhibited a potential plateau around 1.3 V with a discharge capacity of 126 mAh g^{-1} ; more importantly, it showed a capacity retention of 91% after 1000 cycles at 1 C, even at a high current rate of 20 C, it still maintained, a reversible capacity of greater than 90 mAh g^{-1} , corresponded to a capacity retention of 74.5%, with high Coulombic efficiency after cycling 4000 times, which is attributed to the novel morphology and stable structure of the electrodes. Moreover, Liu et al. [303] assembled the $\text{Na}_3\text{V}_2(\text{PO}_4)_2\text{F}_3$ -single walled carbon nanotube(cathode)// $\text{NaTi}_2(\text{PO}_4)_3$ -multiwalled carbon nanotube(anode) aqueous full-cell, which can deliver a high energy density of 150 Wh kg^{-1} in 17 M NaClO_4 electrolyte. More importantly, the full-cell showed the voltage of 1.92 V, which is one of the highest voltages obtained by using intercalation anode and cathode materials in aqueous electrolyte for aqueous rechargeable SIBs.

4. Summary and perspectives

Ambient-temperature SIBs are considered one of the most promising electrochemical power sources for grid-scale energy storage applications due to their competitive cost, sustainable Na-resources supply, and relatively high energy density. The studies on Na-ion intercalation electrochemistry began at 1980s, and the last decade of concerted efforts in the SIB technologies and relevant material science have borne fruit. Advanced electrode materials

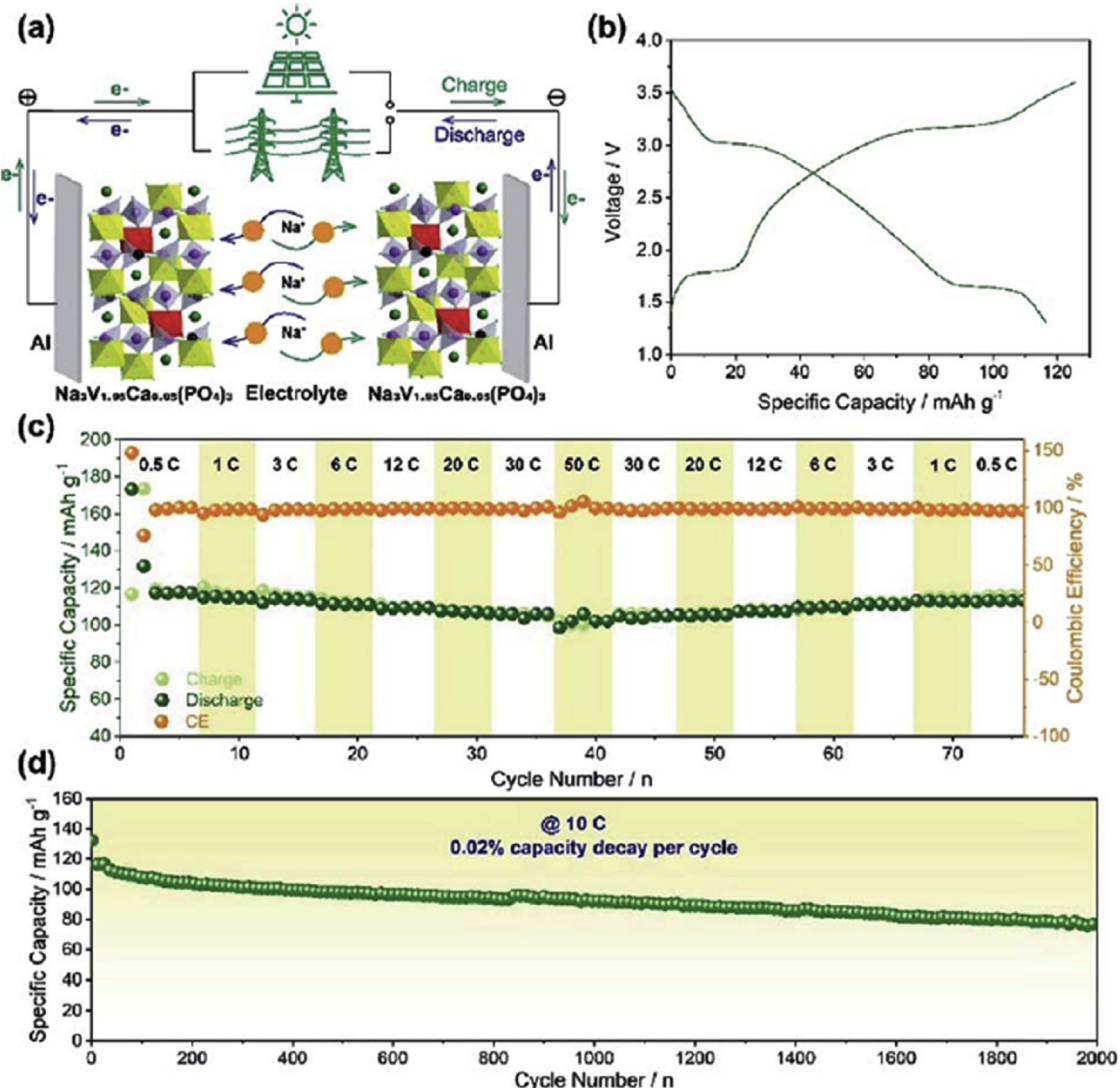


Fig. 15. Schematic illustration of internal structure and operation principle (a); charge/discharge curves at 0.5 C in the voltage window of 1.0–4.0 V (b); rate capability (c); cycling performance at 10 C for 2000 cycles (d) of Ca-doped NVP@C symmetric NIFC. Reproduced with permission [310]. Copyright 2019, The Royal Society of Chemistry.

with high capacity, excellent rate capability, and stable cycling performance are still the bottlenecks for boosting the practical realization of sodium-ion technologies. Among various electrode materials proposed for SIBs system, sodium-based polyanionic compounds, such as phosphates, pyrophosphates, fluorophosphates, orthosilicates, sulfates, and so on have attracted intense research attention.

This review focuses on the recent research progress with polyanionic compounds for room-temperature SIBs. It points out that this novel class of electrode materials is capable of providing robust structural framework that favors promising Na^+ mobility and electrochemical activity. They offer a myriad of crystal structures, owing to the size/type effect of the transition metal and great adaptability of various kinds of polyanion units. It makes an easy way to design and optimize new structures and new material chemistries by tuning the $\text{M}^{n+}/\text{M}^{(n-1)+}$ redox couples or selecting of anionic groups. In this contribution, a high specific energy can be possibly realized by lowering the energy level of 3d band of the transition metal through cationic doping or anionic substitution. On the other hand, excellent reversibility and fast Na-ionic

diffusion in polyanion-type electrode materials have been demonstrated over long cycling tests, which are benefited from the stable and open framework structure of this class of materials.

Among them, $\text{Na}_3\text{V}_2(\text{PO}_4)_3/\text{C}$ and $\text{NaTi}_2(\text{PO}_4)_3/\text{C}$ stand out as the most viable system (cathode and anode, respectively) showing remarkable cycling performance with almost 100% capacity retention after cycling more than 1000 cycles. In pursuing advanced cathode materials with high voltage potential and high specific capacity, recently intensive research enthusiasms were turned to the mixed polyanion cathode systems. By modulating the compositions of the polyanionic groups, such as F/O ratios in $\text{Na}_3\text{V}_{2-x}(\text{PO}_4)_{2x}\text{F}_{1+2x}$ ($0 \leq x \leq 1$), redox potentials can be improved by the inductive effect. Comparatively close value in energy density to the mature electrodes for LIBs was obtained in $\text{Na}_3\text{V}_2(\text{PO}_4)_2\text{O}_2\text{F}$ fluorophosphate, attributed to the high theoretical capacity of 130 mAh g^{-1} based on the $\text{V}^{4+}/\text{V}^{3+}$ redox reaction at high operating plateau of around 3.6 and 4.0 V vs. Na/Na^+ , respectively. In addition, optimizing the composition makes the multiple electrons redox reaction feasibly realized so as to compensate the capacity loss caused by the large molecular weights of polyanion units. Owing to the

achievement of 1.2 electrons transfer, the energy density of 600 Wh kg⁻¹ in Na₃V₂O_{1.6}(PO₄)₂F_{1.4} was successfully obtained. What's more, mixed phosphates Na₄M₃(PO₄)₂P₂O₇ theoretically reach three electrons redox reactions and deliver high-voltage operating over 4.5 V, indicating the promising prospects for application in SIBs.

Before practical application, a full-cell perspective is an essential bridge set up between the sodium-ion half-cell and the commercial battery. Most recent advances of various prototypes of sodium-ion full-cells built with polyanion-type electrode materials and the electrochemistry development are reviewed. The working potentials and specific capacities of representative sodium-ion full-cells are summarized in Fig. 16. As can be seen, most systems exhibit the voltages distributed in a wide range of 1.5–3.5 V, and their energy density range from 150 Wh kg⁻¹ to 250 Wh kg⁻¹ (based on the total weights of cathode and anode), indicating potential applications of high energy density SIBs. It is noteworthy that, the practice capacities of some of the polyanion-type electrodes are far lower than those of their theoretical values, implying there is plenty of room for enhancement of the reversible capacities of these polyanionic materials.

In order to highlight the correspondences between chemistries and electrochemical features of various cathode materials for SIBs, a considerable number of recent reports proposing sodium-ion full-cell set-ups are thoroughly collected and the most significant contributions are specifically sorted. A 3D plot illustrates the average voltage, specific capacity, as well as the energy density of SIFC prototypes in Fig. 17. Three important types of positive electrode materials, including layered metal oxides (green diamond), polyanion compounds (orange ball), and Prussian blue analogues (blue cube) are compared [232,234,243,245,247,248,253,271,279,281,285,304,311–326]. Particularly, the collected energy densities normalization has been made according to the total mass of anode and cathode. Ultimately, high specific capacity was mostly observed in SIFC assemblies constructed by layered metal oxides while the polyanion-type compounds can attain a desirably high working potential. A wide range of operating potential and capacity can be obtained by the material families of Prussian blue analogues. The achievable energy densities among the different cathode materials are encouraging, in

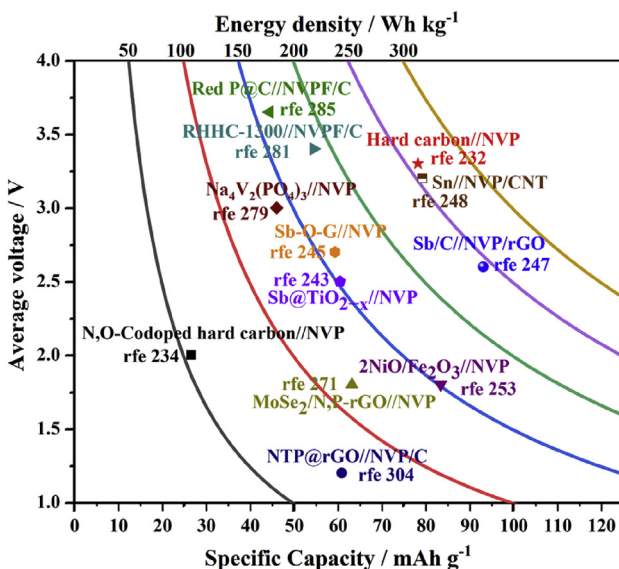


Fig. 16. Average voltage vs. the storage capacity of recent reported Na-ion full-cells composing of polyanion-type electrode materials.

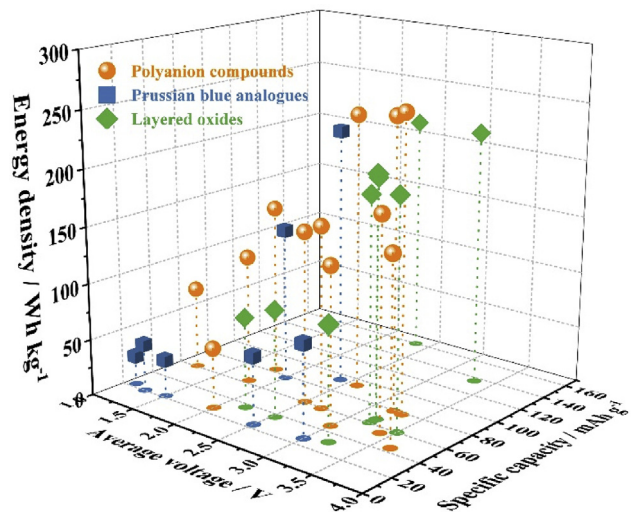


Fig. 17. 3D plot of average potential vs. specific capacity and energy density (normalized by the total mass of anode and cathode materials) of sodium-ion full-cell set-ups.

the range of 100–200 Wh kg⁻¹, proving industry competition actual strength to LIBs. Notably, in some cases among the ones taken in consideration in this review, the polyanionic compound//hard carbon SIFCs, both operation voltage and energy density are considerably higher than those of the average. However, the practical challenges of advanced cathode materials are typically associated with high specific energy, excellent cycling stability, high rate performance, and good safety. The fundamental difficulties in the reversible sodiation/desodiation required for the high-capacity transitional-metal oxides are their insufficient cycling stability, which is related to the complicated multiphase transition reactions and corresponding large structural stress that are inevitable, and intrinsic characteristics of a layered-type cathode. In addition, the air-stability is still one of the key issues for layered oxide cathodes, thus moisture-free process during the material and battery preparation is needed. Owing to the zeolitic water molecules and numerous defects in the host lattice of Prussian blue analogues, their cycling life is also relatively short and stability remains problematic. With respect to the cycling performance, polyanion-type cathode materials hold promise. They are generally less susceptible to the lattice variation associated with Na insertion/extraction owing to the nature of the open crystal framework. Many reports have already demonstrated the excellent cycling stability of over several thousands of cycles. Nevertheless, the presence of heavy polyanionic species depresses the energy density of polyanion-based materials. The modifications to reduce the weight of the polyanionic groups and exploration of new crystal structures are highly required.

Despite the achievements obtained from the current designed polyanion-based compounds, the practical applications of polyanion-based compounds are still severely hindered by their poor rate capability owing to their intrinsic low electronic conductivity. The electrochemical activity of the polyanionic systems can be greatly improved by the well-known strategies including surface engineering with carbon or other conductive compounds, designing and optimizing micro-/nanostructures, modulating the compositions with concentration-gradient regulation or lattice doping. Rational combinations of different modification methods are necessary for the development of advanced electrode materials and maximization of the overall electrochemical performance of the whole battery. Therefore, in order to accelerate the practical

applications of polyanion materials, some issues should be properly addressed such as (1) exploring and optimizing suitable Na^+ ion intercalation structures providing high working voltage and reversible capacity by the means of computational simulations and material chemistry; (2) succeeding high specific capacity with high Coulombic efficiency under high power density through rational strategies of electrode modification; (3) controlling the structural and microstructural parameters and increasing the active material loading which may lead to high energy/volume energy density; and (4) developing safe electrolytes to match the high-operating potentials of cathode materials. Besides efforts on the fundamental research, continuous, incremental improvements on engineering work should be overlooked, as a crucial step to industrial-scale production of SIBs. Polyanion-type materials as cathode or anode provide new opportunities for achieving high-energy and cost-effective SIBs for large-scale energy storage applications.

Declaration of Competing Interest

The authors declare that they have no known competing financial interests or personal relationships that could have appeared to influence the work reported in this paper.

Acknowledgements

This work was supported by the National Key R&D Program of China (2016YFA0200102) and NSFC (U1637202, 51631001, 51590882, and 51672010).

References

- [1] Q. Zhang, E. Uchaker, S.L. Candelaria, G. Cao, *Chem. Soc. Rev.* 42 (2013) 3127–3171.
- [2] B. Kang, G. Ceder, *Nature* 458 (2009) 190–193.
- [3] M.I. Hoffert, K. Caldeira, G. Benford, D.R. Criswell, C. Green, H. Herzog, A.K. Jain, H.S. Kheshgi, K.S. Lackner, J.S. Lewis, H.D. Lightfoot, W. Manheimer, J.C. Mankins, M.E. Mael, L.J. Perkins, M.E. Schlesinger, T. Volk, T.M.L. Wigley, *Science* 298 (2002) 981–987.
- [4] J.M. Tarascon, M. Armand, *Nature* 414 (2011) 171–179.
- [5] J.M. Tarascon, M. Armand, *Nature* 451 (2008) 652–657.
- [6] Z. Yang, J. Zhang, M.C. Kintner-Meyer, X. Lu, D. Choi, J.P. Lemmon, J. Liu, *Chem. Rev.* 111 (2011) 3577–3613.
- [7] L. Lu, X. Han, J. Li, J. Huo, M. Ouyang, *J. Power Sources* 226 (2013) 272–288.
- [8] J. Sun, H.W. Lee, M. Pasta, H. Yuan, G. Zheng, Y. Sun, Y. Li, Y. Cui, *Nat. Nanotechnol.* 10 (2015) 980–985.
- [9] A. Ponrouch, R. Dedryvère, D. Monti, A.E. Demet, J.M. Ateba Mba, L. Croguennec, C. Masquelier, P. Johansson, M.R. Palacín, *Energy Environ. Sci.* 6 (2013) 2361–2369.
- [10] V. Palomares, P. Serras, I. Villaluenga, K.B. Hueso, J. Carretero-González, T. Rojo, *Energy Environ. Sci.* 5 (2012) 5884–5901.
- [11] J. Peters, D. Buchholz, S. Passerini, M. Weil, *Energy Environ. Sci.* 9 (2016) 1744–1751.
- [12] M.S. Islam, C.A. Fisher, *Chem. Soc. Rev.* 43 (2014) 185–204.
- [13] D. Kundu, E. Talaie, V. Duffort, L.F. Nazar, *Angew. Chem. Int. Ed.* 54 (2015) 3431–3448.
- [14] P. Barpanda, S.-i. Nishimura, A. Yamada, *Adv. Energy Mater.* 2 (2012) 841–859.
- [15] H. Kim, H. Kim, Z. Ding, M.H. Lee, K. Lim, G. Yoon, K. Kang, *Adv. Energy Mater.* 6 (2016) 1600943–1600980.
- [16] Z. Jian, Y.S. Hu, X. Ji, W. Chen, *Adv. Mater.* 29 (2017) 1601925–1601940.
- [17] X. Xiang, K. Zhang, J. Chen, *Adv. Mater.* 27 (2015) 5343–5364.
- [18] M.D. Slater, D. Kim, E. Lee, C.S. Johnson, *Adv. Funct. Mater.* 23 (2013) 947–958.
- [19] Y. Cao, L. Xiao, W. Wang, D. Choi, Z. Nie, J. Yu, L.V. Saraf, Z. Yang, J. Liu, *Adv. Mater.* 23 (2011) 3155–3160.
- [20] Y. Fang, X.-Y. Yu, X.W. Lou, *Angew. Chem. Int. Ed.* 56 (2017) 5801–5805.
- [21] Y. Fang, J. Zhang, L. Xiao, X. Ai, Y. Cao, H. Yang, *Adv. Sci.* 4 (2017) 1600392–1600412.
- [22] K. Kaliyappan, J. Liu, B. Xiao, A. Lushington, R. Li, T.-K. Sham, X. Sun, *Adv. Funct. Mater.* 27 (2017) 1701870–1701877.
- [23] D. Tie, G. Gao, F. Xia, R. Yue, Q. Wang, R. Qi, B. Wang, Y. Zhao, *ACS Appl. Mater. Interfaces* 11 (2019) 6978–6985.
- [24] L. Zhao, H. Zhao, Z. Du, N. Chen, X. Chang, Z. Zhang, F. Gao, A. Trenczek-Zajac, K. Świerczek, *Electrochim. Acta* 282 (2018) 510–519.
- [25] L. Zhao, H. Zhao, X. Long, Z. Li, Z. Du, *ACS Appl. Mater. Interfaces* 10 (2018) 35963–35971.
- [26] H.W. Lee, R.Y. Wang, M. Pasta, S. Woo Lee, N. Liu, Y. Cui, *Nat. Commun.* 5 (2014) 5280–5285.
- [27] Y. Liu, Y. Qiao, W. Zhang, Z. Li, X. Ji, L. Miao, L. Yuan, X. Hu, Y. Huang, *Nano Energy* 12 (2015) 386–393.
- [28] M. Pasta, C.D. Wessells, N. Liu, J. Nelson, M.T. McDowell, R.A. Huggins, M.F. Toney, Y. Cui, *Nat. Commun.* 5 (2014) 3007–3015.
- [29] C.D. Wessells, R.A. Huggins, Y. Cui, *Nat. Commun.* 2 (2011) 550–554.
- [30] X. Wu, Y. Luo, M. Sun, J. Qian, Y. Cao, X. Ai, H. Yang, *Nano Energy* 13 (2015) 117–123.
- [31] Y. Cao, L. Xiao, M.L. Sushko, W. Wang, B. Schwenzer, J. Xiao, Z. Nie, L.V. Saraf, Z. Yang, J. Liu, *Nano Lett.* 12 (2012) 3783–3787.
- [32] L. Xiao, Y. Cao, W.A. Henderson, M.L. Sushko, Y. Shao, J. Xiao, W. Wang, M.H. Engelhard, Z. Nie, J. Liu, *Nano Energy* 19 (2016) 279–288.
- [33] H. Hou, X. Qiu, W. Wei, Y. Zhang, X. Ji, *Adv. Energy Mater.* 7 (2017) 1602898–1602927.
- [34] S. Huang, Z. Li, B. Wang, J. Zhang, Z. Peng, R. Qi, J. Wang, Y. Zhao, *Adv. Funct. Mater.* 28 (2018) 1706294–1706303.
- [35] L. Wu, X. Hu, J. Qian, F. Pei, F. Wu, R. Mao, X. Ai, H. Yang, Y. Cao, *Energy Environ. Sci.* 7 (2014) 323–328.
- [36] J. Qian, X. Wu, Y. Cao, X. Ai, H. Yang, *Angew. Chem. Int. Ed.* 52 (2013) 4633–4636.
- [37] L. Xiao, Y. Cao, J. Xiao, W. Wang, L. Kovarik, Z. Nie, J. Liu, *Chem. Commun.* 48 (2012) 3321–3323.
- [38] S. Shi, Z. Li, Y. Sun, B. Wang, Q. Liu, Y. Hou, S. Huang, J. Huang, Y. Zhao, *Nano Energy* 48 (2018) 510–517.
- [39] Z. Ali, M. Asif, X. Huang, T. Tang, Y. Hou, *Adv. Mater.* 30 (2018) 1802745–1802753.
- [40] Z. Ali, M. Asif, T. Zhang, X. Huang, Y. Hou, *Small* 15 (2019) 1901995–1902004.
- [41] Z. Ali, T. Tang, X. Huang, Y. Wang, M. Asif, Y. Hou, *Energy Stor. Mater.* 13 (2018) 19–28.
- [42] S. Huang, M. Wang, P. Jia, B. Wang, J. Zhang, Y. Zhao, *Energy Stor. Mater.* 20 (2019) 225–233.
- [43] D. Yuan, X. Liang, L. Wu, Y. Cao, X. Ai, J. Feng, H. Yang, *Adv. Mater.* 26 (2014) 6301–6306.
- [44] H. Pan, Y.-S. Hu, L. Chen, *Energy Environ. Sci.* 6 (2013) 2338–2360.
- [45] Y. You, X.-L. Wu, Y.-X. Yin, Y.-G. Guo, *Energy Environ. Sci.* 7 (2014) 1643–1647.
- [46] L. Wang, J. Song, R. Qiao, L.A. Wray, M.A. Hossain, Y.-D. Chuang, W. Yang, Y. Lu, D. Evans, J.-J. Lee, S. Vail, X. Zhao, M. Nishijima, S. Kakimoto, J.B. Goodenough, *J. Am. Chem. Soc.* 137 (2015) 2548–2554.
- [47] J.W. Wang, X.H. Liu, S.X. Mao, J.Y. Huang, *Nano Lett.* 12 (2012) 5897–5902.
- [48] J. Zhou, Z. Jiang, S. Niu, S. Zhu, J. Zhou, Y. Zhu, J. Liang, D. Han, K. Xu, L. Zhu, X. Liu, G. Wang, Y. Qian, *Chem* 4 (2018) 372–385.
- [49] S. Liu, J. Feng, X. Bian, J. Liu, H. Xu, Y. An, *Energy Environ. Sci.* 10 (2017) 1222–1233.
- [50] P. Moreau, D. Guyomard, J. Gaubicher, F. Boucher, *Chem. Mater.* 22 (2010) 4126–4128.
- [51] J.N. Bridson, S.E. Quinlan, P.R. Tremaine, *Chem. Mater.* 10 (1998) 763–768.
- [52] I.V. Zatovsky, *Acta Crystallogr. Sect. E Struct. Rep. Online* 66 (2010) i12–i21.
- [53] M. Gabelica-robert, M. Goreaud, P. Labbe, B. Raveau, *J. Solid State Chem.* 45 (1982), 3898–3939.
- [54] T. Moya-Pizarro, R. Salmon, L. Fournes, G. Le Flem, B. Wanklyn, P. Hagenmuller, *J. Solid State Chem.* 53 (1984) 387–397.
- [55] A. Leclaire, A. Benmoussa, M.M. Borel, A. Grandin, B. Raveau, *J. Solid State Chem.* 77 (1988) 299–305.
- [56] Y.P. Wang, K.H. Lii, S.L. Wang, *Acta Crystallogr. Sect. C Cryst. Struct. Commun.* 445 (1989) 1417–1418.
- [57] F. Sanz, C. Parada, J.M. Rojo, C. Ruiz-Valero, R. Saez-Puche, *J. Solid State Chem.* 145 (1990) 611–616.
- [58] F. Erragh, A. Boukhari, B. Elouadi, E.M. Holt, *J. Crystallogr. Spectrosc. Res.* 21 (1991) 321–326.
- [59] P. Barpanda, T. Ye, S.-i. Nishimura, S.-C. Chung, Y. Yamada, M. Okubo, H. Zhou, A. Yamada, *Electrochim. Commun.* 24 (2012) 116–119.
- [60] Q. Huang, S.-J. Hwu, *Inorg. Chem.* 37 (1998) 5869–5874.
- [61] K.M.S. Etheredge, S.-J. Hwu, *Inorg. Chem.* 34 (1995) 1495–1499.
- [62] F. Erragh, A. Boukhari, F. Abraham, B. Elouadi, *J. Solid State Chem.* 120 (1995) 23–31.
- [63] F. Erragh, A. Boukhari, A. Sadel, E.M. Holt, *Acta Crystallogr. Sect. C Cryst. Struct. Commun.* 54 (1998) 1373–1376.
- [64] L. Benhamada, A. Grandin, M.M. Borel, A. Leclaire, B. Raveau, *J. Solid State Chem.* 101 (1992) 154–160.
- [65] A. Daidouh, M.L. Veiga, C. Pico, *Solid State Ion.* 106 (1998) 103–113.
- [66] H. Kim, I. Park, D.-H. Seo, S. Lee, S.-W. Kim, W.J. Kwon, Y.-U. Park, C.S. Kim, S. Jeon, K. Kang, *J. Am. Chem. Soc.* 134 (2012) 10369–10372.
- [67] F. Sanz, C. Parada, U. Amador, M.A. Monge, C.R. Valero, *J. Solid State Chem.* 123 (1996) 129–139.
- [68] F. Sanz, C. Parada, J.M. Rojo, C. Ruiz-Valero, *Chem. Mater.* 13 (2001) 1334–1340.
- [69] J. Barker, M.Y. Saidi, J.L. Swoyer, *J. Electrochem. Soc.* 151 (2004) A1670–A1677.
- [70] Ю.К. Кабалов, М.А. Симонов, Н.В. Белов, *Российская академия наук* 215 (1974) 850–853.

- [71] J.M. Le Meins, M.P. Crosnier-Lopez, A. Hemon-Ribaud, G. Courbion, *J. Solid State Chem.* 148 (1999) 260–277.
- [72] F. Sauvage, E. Quarez, J.M. Tarascon, E. Baudrin, *Solid State Sci.* 8 (2006) 1215–1221.
- [73] A.A. Tsirlin, R. Nath, A.M. Abakumov, Y. Furukawa, D.C. Johnston, M. Hemmida, H.-A.K. v. Nidda, A. Loidl, C. Geibel, H. Rosner, *Phys. Rev. B* 84 (2011), 014429–014443.
- [74] C. Wu, P. Kopolid, Y.-L. Ding, P.A.V. Aken, J. Maier, Y. Yu, *ACS Nano* 9 (2015) 6610–6618.
- [75] S. Chen, C. Wu, L. Shen, C. Zhu, Y. Huang, K. Xi, J. Maier, Y. Yu, *Adv. Mater.* 29 (2017) 1700431–1700451.
- [76] Z. Gong, Y. Yang, *Energy Environ. Sci.* 4 (2011) 3223–3242.
- [77] B. Senthilkumar, C. Murugesan, L. Sharma, S. Lochab, P. Barpanda, *Small Methods* 3 (2018) 1800253–1800275.
- [78] J.B. Goodenough, H.Y.P. Hong, J.A. Kafalas, *Mater. Res. Bull.* 11 (1976) 203–220.
- [79] A.K. Padhi, K.S. Nanjundaswamy, J.B. Goodenough, *J. Electrochem. Soc.* 144 (1997) 1188–1194.
- [80] A.K. Padhi, K.S. Nanjundaswamy, C. Masquelier, S. Okada, J.B. Goodenough, *J. Electrochem. Soc.* 144 (1997) 1609–1613.
- [81] M. Casas-Cabanas, V.V. Roddatis, D. Saurel, P. Kubiaik, J. Carretero-González, V. Palomares, P. Serras, T. Rojo, *J. Mater. Chem.* 22 (2012) 17421–17423.
- [82] Y. Fang, Q. Liu, L. Xiao, X. Ai, H. Yang, Y. Cao, *ACS Appl. Mater. Interfaces* 7 (2015) 17977–17984.
- [83] J. Lu, S.C. Chung, S.-i. Nishimura, A. Yamada, *Chem. Mater.* 25 (2013) 4557–4565.
- [84] M. Galceran, V. Roddatis, F.J. Zúñiga, J.M. Pérez-Mato, B. Acebedo, R. Arenal, I. Peral, T. Rojo, M. Casas-Cabanas, *Chem. Mater.* 26 (2014) 3289–3294.
- [85] J. Kim, D.-H. Seo, H. Kim, I. Park, J.-K. Yoo, S.-K. Jung, Y.-U. Park, W.A. Goddard III, K. Kang, *Energy Environ. Sci.* 8 (2015) 540–545.
- [86] Y. Zhu, Y. Xu, Y. Liu, C. Luo, C. Wang, *Nanoscale* 5 (2013) 780–787.
- [87] N. Le Poule, *Solid State Ion.* 159 (2003) 149–158.
- [88] N. Wongitharom, T.-C. Lee, C.-H. Wang, Y.-C. Wang, J.-K. Chang, *J. Mater. Chem.* 2 (2014) 5655–5661.
- [89] S.-M. Oh, S.-T. Myung, J. Hassoun, B. Scrosati, Y.-K. Sun, *Electrochem. Commun.* 22 (2012) 149–152.
- [90] M. Galceran, D. Saurel, B. Acebedo, V.V. Roddatis, E. Martin, T. Rojo, M. Casas-Cabanas, *Phys. Chem. Chem. Phys.* 16 (2014) 8837–8842.
- [91] F. Boucher, J. Gaubicher, M. Cuisinier, D. Guyomard, P. Moreau, *J. Am. Chem. Soc.* 136 (2014) 9144–9157.
- [92] A. Saracibar, J. Carrasco, D. Saurel, M. Galceran, B. Acebedo, H. Anne, M. Lepoittevin, T. Rojo, M. Casas-Cabanas, *Phys. Chem. Chem. Phys.* 18 (2016) 13045–13051.
- [93] S.J. Tracy, L. Mauger, H.L. Smith, H.J. Tan, J.E. Herriman, Y. Xiao, B. Fultz, *Chem. Mater.* 28 (2016) 3051–3059.
- [94] J. Sugiyama, H. Nozaki, M. Harada, Y. Higuchi, J.H. Brewer, E.J. Ansaldi, G. Kobayashi, R. Kanno, *Phys. Rev. B* 90 (2014), 014426–014435.
- [95] Y. Liu, N. Zhang, F. Wang, X. Liu, L. Jiao, L.-Z. Fan, *Adv. Funct. Mater.* 28 (2018) 1801917–1801925.
- [96] F. Xiong, Q. An, L. Xia, Y. Zhao, L. Mai, H. Tao, Y. Yue, *Nano Energy* 57 (2019) 608–615.
- [97] S. Sevinc, B. Tekin, A. Ata, M. Morcrette, H. Perrot, O. Sel, R. Demir-Cakan, *J. Power Sources* 412 (2019) 55–62.
- [98] S. Jeong, B.H. Kim, Y.D. Park, C.Y. Lee, J. Mun, A. Tron, *J. Alloy. Comp.* 784 (2019) 720–726.
- [99] X. Ma, J. Xia, X. Wu, Z. Pan, P.K. Shen, *Carbon* 146 (2019) 78–87.
- [100] M.M. Rahman, I. Sultana, S. Mateti, J. Liu, N. Sharma, Y. Chen, *J. Mater. Chem.* 5 (2017) 16616–16621.
- [101] J. Hwang, K. Matsumoto, Y. Orikasa, M. Katayama, Y. Inada, T. Nohira, R. Hagiwara, *J. Power Sources* 377 (2018) 80–86.
- [102] C. Heubner, S. Heiden, M. Schneider, A. Michaelis, *Electrochim. Acta* 233 (2017) 78–84.
- [103] X. Song, T. Liu, J. Amine, Y. Duan, J. Zheng, Y. Lin, F. Pan, *Nano Energy* 37 (2017) 90–97.
- [104] H.Y.-P. Hong, *Mater. Res. Bull.* 11 (1976) 173–182.
- [105] C. Delmas, A. Nadiri, J.L. Soubeyroux, *Solid State Ion.* 28 (1988) 419–423.
- [106] J. Gopalakrishnan, K.K. Rangan, *Chem. Mater.* 4 (1992) 745–747.
- [107] F. d'Yvoire, M. Pintard-Scrépel, E. Bretey, M. De la Rochere, *Solid State Ion.* 9 (1983) 851–857.
- [108] Z. Jian, L. Zhao, H. Pan, Y.-S. Hu, H. Li, W. Chen, L. Chen, *Electrochim. Commun.* 14 (2012) 86–89.
- [109] Z. Jian, W. Han, X. Lu, H. Yang, Y.-S. Hu, J. Zhou, Z. Zhou, J. Li, W. Chen, D. Chen, L. Chen, *Adv. Energy Mater.* 3 (2013) 156–160.
- [110] Z. Jian, C. Yuan, W. Han, X. Lu, L. Gu, X. Xi, Y.-S. Hu, H. Li, W. Chen, D. Chen, Y. Ikuhara, L. Chen, *Adv. Funct. Mater.* 24 (2014) 4265–4272.
- [111] W. Song, X. Ji, Z. Wu, Y. Zhu, Y. Yang, J. Chen, M. Jing, F. Li, C.E. Banks, *J. Mater. Chem.* 2 (2014) 5358–5362.
- [112] K.M. Bui, V.A. Dinh, S. Okada, T. Ohno, *Phys. Chem. Chem. Phys.* 17 (2015) 30433–30439.
- [113] Y. Uebou, T. Kiyabu, S. Okada, J. I. Yamaki, (2002) 1–5.
- [114] K. Saravanan, C.W. Mason, A. Rudola, K.H. Wong, P. Balaya, *Adv. Energy Mater.* 3 (2013) 444–450.
- [115] W. Song, X. Cao, Z. Wu, J. Chen, K. Huangfu, X. Wang, Y. Huang, X. Ji, *Phys. Chem. Chem. Phys.* 16 (2014) 17681–17687.
- [116] X. Wei, M.S. Wang, Y. Bando, D. Golberg, *J. Am. Chem. Soc.* 132 (2010) 13592–13593.
- [117] H. Zhou, S. Upadhyay, N.A. Chernova, G. Hautier, G. Ceder, M.S. Whittingham, *Chem. Mater.* 23 (2011) 293–300.
- [118] N. Yabuuchi, K. Kubota, M. Dahbi, S. Komaba, *Chem. Rev.* 114 (2014) 11632–11682.
- [119] M. Gabelica-Robert, M. Goreaud, P. Labbe, B. Raveau, *J. Solid State Chem.* 45 (1982) 389–395.
- [120] A. Leclaire, M.M. Borel, A. Grandin, B. Raveau, *J. Solid State Chem.* 76 (1988) 131–135.
- [121] Y. Kee, N. Dimov, A. Staikov, P. Barpanda, Y.C. Lu, K. Minami, S. Okada, *RSC Adv.* 5 (2015) 64991–64996.
- [122] J.M. Clark, P. Barpanda, A. Yamada, M.S. Islam, *J. Mater. Chem.* 2 (2014) 11807–11812.
- [123] C.-Y. Chen, K. Matsumoto, T. Nohira, C. Ding, T. Yamamoto, R. Hagiwara, *Electrochim. Acta* 133 (2014) 583–588.
- [124] P. Barpanda, T. Ye, M. Avdeev, S.-C. Chunga, A. Yamada, *J. Mater. Chem.* 1 (2013) 4194–4197.
- [125] N.K. Lokanath, M.A. Sridhar, J.S. Prasad, G.S. Gopalakrishna, K.G. Ashamanjari, *Bull. Mater. Sci.* 23 (2000) 175–178.
- [126] S.M. Wood, C. Eames, E. Kendrick, M.S. Islam, *J. Phys. Chem. C* 119 (2015) 15935–15941.
- [127] D.A. Aksyonov, S.S. Fedotov, K.J. Stevenson, A. Zhugayevych, *Comput. Mater. Sci.* 154 (2018) 449–458.
- [128] M. Nose, H. Nakayama, K. Nobuhara, H. Yamaguchi, S. Nakanishi, H. Iba, *J. Power Sources* 234 (2013) 175–179.
- [129] B. Senthilkumar, G. Ananya, S. Ramaprabhu, *Electrochim. Acta* 169 (2015), 477–455.
- [130] H.N. Ng, C. Calvo, *Can. J. Chem.* 51 (1973) 2613–2620.
- [131] E. Antipov, A.M. Abakumov, K. Stevenson, D.A. Aksyonov, A. Alekseeva, I. Tertov, O. Drozhzhin, *Chem. Mater.* 31 (2019) 7463–7469.
- [132] H. Kim, R.A. Shakoor, C. Park, S.Y. Lim, J.-S. Kim, Y.N. Jo, W. Cho, K. Miyasaka, R. Kahraman, Y. Jung, J.W. Choi, *Adv. Funct. Mater.* 23 (2013) 1147–1155.
- [133] C.S. Park, H. Kim, R.A. Shakoor, E. Yang, S.Y. Lim, R. Kahraman, Y. Jung, J.W. Choi, *J. Am. Chem. Soc.* 135 (2013) 2787–2792.
- [134] H. Kim, C.S. Park, J.W. Choi, Y. Jung, *Angew. Chem. Int. Ed.* 55 (2016) 6662–6666.
- [135] M.J. Mahesh, G.S. Gopalakrishna, Ashamanjari, *Mater. Char.* 57 (2006) 30–35.
- [136] P. Barpanda, M. Avdeev, C.D. Ling, J. Lu, A. Yamada, *Inorg. Chem.* 52 (2012) 395–401.
- [137] P. Barpanda, G. Liu, C.D. Ling, M. Tamaru, M. Avdeev, S.-C. Chung, Y. Yamada, A. Yamada, *Chem. Mater.* 25 (2013) 3480–3487.
- [138] L. Beaury, J. Derouet, L. Binet, F. Sanz, C. Ruiz-Valero, *J. Solid State Chem.* 177 (2004) 1437–1443.
- [139] A.C. Keates, Q. Wang, M.T. Weller, *J. Solid State Chem.* 210 (2014) 10–14.
- [140] J. Bennazah, A. Boukharia, E.M. Holtb, *Acta Crystallogr. Sect. C Cryst. Struct. Commun.* 58 (2002) i87–i89.
- [141] I. Belharouak, P. Gravereau, C. Parent, J.P. Chaminade, E. Lebraud, G.L. Flem, *J. Solid State Chem.* 152 (2000) 466–473.
- [142] R.A. Shakoor, C.S. Park, A.A. Raju, J. Shin, R. Kahraman, *Phys. Chem. Chem. Phys.* 18 (2016) 3929–3935.
- [143] V. Venckutė, A. Dindune, D. Valdniece, A. Maneikis, S. Daugėla, T. Šalkus, A. Krumina, M. Lelis, V. Jasulaitienė, A. Kežionis, A.F. Orliukas, *Lithuanian J. Phys.* 57 (2017) 183–193.
- [144] P. Barpanda, J. Lu, T. Ye, M. Kajiyama, S.-C. Chung, N. Yabuuchi, S. Komaba, A. Yamada, *RSC Adv.* 3 (2013) 3857–3860.
- [145] A.K. Padhi, K.S. Nanjundaswamy, J.B. Goodenough, *J. Electrochem. Soc.* 144 (1997) 1188–1194.
- [146] A.K. Padhi, V. Manivannan, J.B. Goodenough, *J. Electrochem. Soc.* 145 (1998) 1518–1520.
- [147] H. Kim, I. Park, S. Lee, H. Kim, K.-Y. Park, Y.-U. Park, H. Kim, J. Kim, H.-D. Lim, W.-S. Yoon, K. Kang, *Chem. Mater.* 25 (2013) 3614–3622.
- [148] M. Zarzabeitia, MaríaJáuregui, N. Sharma, J.C. Pramudita, M. Casas-Cabanas, *Chem. Mater.* 31 (2019) 5152–5159.
- [149] J. Barker, M.Y. Saidi, J.L. Swoyer, *Electrochim. Solid State Lett.* 6 (2003) A1–A4.
- [150] C. Chang, Y. Li, W. He, G. Li, W. Guo, P. Zhu, M. Yao, J. Feng, *Mater. Lett.* 209 (2017) 82–85.
- [151] M. Law, P. Balaya, *Energy Stor. Mater.* 10 (2018) 102–113.
- [152] M. Xu, C.-J. Cheng, Q.-Q. Sun, S.-J. Bao, Y.-B. Niu, H. He, Y. Lic, J. Song, *RSC Adv.* 5 (2015) 40065–40069.
- [153] Y. Lu, S. Zhang, Y. Li, L. Xue, G. Xu, X. Zhang, *J. Power Sources* 247 (2014) 770–777.
- [154] Y.-L. Ruan, K. Wang, S.-D. Song, X. Han, B.-W. Cheng, *Electrochim. Acta* 160 (2015) 330–336.
- [155] H. Zhuo, X. Wang, A. Tang, Z. Liu, S. Gamboa, P.J. Sebastian, *J. Power Sources* 160 (2006) 698–703.
- [156] X. Deng, W. Shi, J. Sunarso, M. Liu, Z. Shao, *ACS Appl. Mater. Interfaces* 9 (2017) 16280–16287.
- [157] Q. Li, Z. Liu, F. Zheng, R. Liu, J. Lee, G.L. Xu, G. Zhong, X. Hou, R. Fu, Z. Chen, K. Amine, J. Mi, S. Wu, C.P. Grey, Y. Yang, *Angew. Chem. Int. Ed.* 57 (2018) 11918–11923.
- [158] B.L. Ellis, W.R. Makahnouk, Y. Makimura, K. Toghill, L.F. Nazar, *Nat. Mater.* 6 (2007) 749–753.

- [159] N. Recham, J.-N. Chotard, L. Dupont, K. Djellab, M. Armand, J.-M. Tarascon, *J. Electrochem. Soc.* 156 (2009) A933–A999.
- [160] A. Langrock, Y. Xu, Y. Liu, S. Ehrman, A. Manivannan, C. Wang, *J. Power Sources* 233 (2013) 62–67.
- [161] D.L. Smiley, G.R. Goward, *Chem. Mater.* 28 (2016) 7645–7656.
- [162] Y. Kawabe, N. Yabuuchi, M. Kajiyama, N. Fukuhara, T. Inamasu, R. Okuyama, I. Nakai, S. Komaba, *Electrochem. Commun.* 13 (2011) 1225–1228.
- [163] J. Yan, X. Liu, B. Li, *Electrochem. Commun.* 56 (2015) 46–50.
- [164] M. Brisbois, N. Krins, R.P. Hermann, A. Schrijnemakers, R. Cloots, B. Vertruyen, F. Boschini, *Mater. Lett.* 130 (2014) 263–266.
- [165] R. Ling, S. Cai, S. Shen, X. Hu, D. Xie, F. Zhang, X. Sun, N. Yu, F. Wang, *J. Alloy. Comp.* 704 (2017) 631–640.
- [166] F. Wang, N. Zhang, X. Zhao, L. Wang, J. Zhang, T. Wang, F. Liu, Y. Liu, L.Z. Fan, *Adv. Sci.* 6 (2019) 1900649–1900653.
- [167] R. Tripathi, S.M. Wood, M.S. Islam, L.F. Nazar, *Energy Environ. Sci.* 6 (2013) 2257–2264.
- [168] J.-Z. Guo, Y. Yang, D.-S. Liu, X.-L. Wu, B.-H. Hou, W.-L. Pang, K.-C. Huang, J.-P. Zhang, Z.-M. Su, *Adv. Energy Mater.* 8 (2018) 1702504–1702510.
- [169] J. Xu, J. Chen, L. Tao, Z. Tian, S. Zhou, N. Zhao, C.-P. Wong, *Nano Energy* 60 (2019) 510–519.
- [170] C. Li, M. Shen, X. Lou, B. Hu, *J. Phys. Chem. C* 122 (2018) 27224–27232.
- [171] Y. Cai, X. Cao, Z. Luo, G. Fang, F. Liu, J. Zhou, A. Pan, S. Liang, *Adv. Sci.* 5 (2018) 1800680–1800689.
- [172] Y. Qi, Z. Tong, J. Zhao, L. Ma, T. Wu, H. Liu, C. Yang, J. Lu, Y.-S. Hu, *Joule* 2 (2018) 2348–2363.
- [173] M. Bianchini, N. Brisset, F. Fauth, F. Weill, E. Elkaim, E. Suard, C. Masquelier, L. Croguennec, *Chem. Mater.* 26 (2014) 4238–4247.
- [174] J. Barker, R.K.B. Gover, P. Burns, A.J. Bryan, *Electrochem. Solid State Lett.* 9 (2006) A190–A192.
- [175] R. Gover, A. Bryan, P. Burns, J. Barker, *Solid State Ion.* 177 (2006) 1495–1500.
- [176] R.A. Shakoor, D.-H. Seo, H. Kim, Y.-U. Park, J. Kim, S.-W. Kim, H. Gwon, S. Lee, K. Kang, *J. Mater. Chem.* 22 (2012) 20535–20541.
- [177] J. Barker, R.K.B. Gover, P. Burns, A.J. Bryan, *J. Electrochem. Soc.* 154 (2007) A882–A887.
- [178] M. Bianchini, F. Fauth, N. Brisset, F. Weill, E. Suard, C. Masquelier, L. Croguennec, *Chem. Mater.* 27 (2015) 3009–3020.
- [179] Z. Liu, Y.-Y. Hu, M.T. Dunstan, H. Huo, X. Hao, H. Zou, G. Zhong, Y. Yang, C.P. Grey, *Chem. Mater.* 26 (2014) 2513–2521.
- [180] W. Song, X. Cao, Z. Wu, J. Chen, Y. Zhu, H. Hou, Q. Lan, X. Ji, *Langmuir* 30 (2014) 12438–12446.
- [181] G. Deng, D. Chao, Y. Guo, Z. Chen, H. Wang, S.V. Savilov, J. Lin, Z.X. Shen, *Energy Stor. Mater.* 5 (2016) 198–204.
- [182] Y. Qi, L. Mu, J. Zhao, Y.S. Hu, H. Liu, S. Dai, *Angew. Chem. Int. Ed.* 54 (2015) 9911–9916.
- [183] W. Massa, O.V. Yakubovich, O.V. Dimitrova, *Solid State Sci.* 4 (2002) 495–501.
- [184] N. Sharma, P. Serras, V. Palomares, H.E.A. Brand, J. Alonso, P. Kubiak, M.L. Fdez-Gubieda, T. Rojo, *Chem. Mater.* 26 (2014) 3391–3402.
- [185] Y.-U. Park, D.-H. Seo, H. Kim, J. Kim, S. Lee, B. Kim, K. Kang, *Adv. Funct. Mater.* 24 (2014) 4603–4614.
- [186] Y.U. Park, D.H. Seo, H.S. Kwon, B. Kim, J. Kim, H. Kim, I. Kim, H.I. Yoo, K. Kang, *J. Am. Chem. Soc.* 135 (2013) 13870–13878.
- [187] M. Xu, P. Xiao, S. Stauffer, J. Song, G. Henkelman, J.B. Goodenough, *Chem. Mater.* 26 (2014) 3089–3097.
- [188] W. Song, X. Ji, Z. Wu, Y. Yang, Z. Zhou, F. Li, Q. Chen, C.E. Banks, *J. Power Sources* 256 (2014) 258–263.
- [189] P. Barpanda, G. Oyama, S. Nishimura, S.C. Chung, A. Yamada, *Nat. Commun.* 5 (2014) 4358–4365.
- [190] G. Oyama, S.-i. Nishimura, Y. Suzuki, M. Okubo, A. Yamada, *ChemElectroChem* 2 (2015) 1019–1023.
- [191] T. Yu, B. Lin, Q. Li, X. Wang, W. Qu, S. Zhang, C. Deng, *Phys. Chem. Chem. Phys.* 18 (2016) 26933–26941.
- [192] Y. Meng, T. Yu, S. Zhang, C. Deng, *J. Mater. Chem.* 4 (2016) 1624–1631.
- [193] X. Liu, L. Tang, Q. Xu, H. Liu, Y. Wang, *Electrochim. Acta* 296 (2019) 345–354.
- [194] P. Singh, K. Shiva, H. Celio, J.B. Goodenough, *Energy Environ. Sci.* 8 (2015) 3000–3005.
- [195] J.C. Treacher, S.M. Wood, M.S. Islam, E. Kendrick, *Phys. Chem. Chem. Phys.* 18 (2016) 32744–32752.
- [196] V.S. Rangasamy, S. Thayumanasundaram, J.-P. Locquet, *Electrochim. Acta* 276 (2018) 102–110.
- [197] H. Duncan, A. Kondamreddy, P.H.J. Mercier, Y. Le Page, Y. Abu-Lebdeh, M. Couillard, P.S. Whitfield, I.J. Davidson, *Chem. Mater.* 23 (2011) 5446–5456.
- [198] H. Zhu, J. Wang, X. Liu, X. Zhu, *RSC Adv.* 7 (2017) 14145–14151.
- [199] M. Law, V. Ramar, P. Balaya, *J. Power Sources* 359 (2017) 277–284.
- [200] P. Zhang, Y. Xu, F. Zheng, S.Q. Wu, Y. Yang, Z.-Z. Zhu, *CrystEngComm* 17 (2015) 2123–2128.
- [201] Y. Zhang, H. Yu, H. Zhou, *J. Mater. Chem.* 2 (2014) 11574–11577.
- [202] S. Li, J. Guo, Z. Ye, X. Zhao, S. Wu, J.X. Mi, C.Z. Wang, Z. Gong, M.J. McDonald, Z. Zhu, K.M. Ho, Y. Yang, *ACS Appl. Mater. Interfaces* 8 (2016) 17233–17238.
- [203] W. Guan, B. Pan, P. Zhou, J. Mi, D. Zhang, J. Xu, Y. Jiang, *ACS Appl. Mater. Interfaces* 9 (2017) 22369–22377.
- [204] J. Lee, A. Urban, X. Li, D. Su, G. Hautier, G. Ceder, *Science* 343 (2014) 519–522.
- [205] T. Shiratsuchi, S. Okada, J. Yamaki, T. Nishida, *J. Power Sources* 159 (2006) 268–271.
- [206] V. Mathew, S. Kim, J. Kang, J. Gim, J. Song, J.P. Baboo, W. Park, D. Ahn, J. Han, L. Gu, Y. Wang, Y.-S. Hu, Y.-K. Sun, J. Kim, *NPG Asia Mater.* 6 (2014) e138–e138.
- [207] G. Yang, B. Ding, J. Wang, P. Nie, H. Dou, X. Zhang, *Nanoscale* 8 (2016) 8495–8499.
- [208] T. Liu, Y. Duan, G. Zhang, M. Li, Y. Feng, J. Hu, J. Zheng, J. Chen, F. Pan, *J. Mater. Chem.* 4 (2016) 4479–4484.
- [209] Y. Liu, S. Xu, S. Zhang, J. Zhang, J. Fan, Y. Zhou, *J. Mater. Chem.* 3 (2015) 5501–5508.
- [210] S. Xu, S. Zhang, J. Zhang, T. Tan, Y. Liu, *J. Mater. Chem.* 2 (2014) 7221–7228.
- [211] Y. Fang, L. Xiao, J. Qian, X. Ai, H. Yang, Y. Cao, *Nano Lett.* 14 (2014) 3539–3543.
- [212] P. Senguttuvan, G. Rousse, M.E. Arroyo y de Dompablo, H. Vezin, J.M. Tarascon, M.R. Palacin, *J. Am. Chem. Soc.* 135 (2013) 3897–3903.
- [213] L. Wang, B. Wang, G. Liu, T. Liu, T. Gao, D. Wang, *RSC Adv.* 6 (2016) 70277–70283.
- [214] C. Delmas, F. Cherkaoui, A. Nadiri, P. Hagenmuller, *Mater. Res. Bull.* 22 (1987) 631–639.
- [215] C. Delmas, A. Nadiri, J.L. Soubeyroux, *Solid State Ion.* 28 (1988) 419–423.
- [216] C. Delmas, A. Nadiri, *Mater. Res. Bull.* 23 (1988) 65–72.
- [217] W. Wu, S. Shabbag, J. Chang, A. Rutt, J.F. Whitacre, *J. Electrochem. Soc.* 162 (2015) A803–A808.
- [218] A.I. Mohamed, N.J. Sansone, B. Kuei, N.R. Washburn, J.F. Whitacre, *J. Electrochem. Soc.* 162 (2015) A2201–A2207.
- [219] M. Vujković, M. Mitić, S. Mentus, *J. Power Sources* 288 (2015) 176–186.
- [220] S.I. Park, I. Gocheva, S. Okada, J.-i. Yamaki, *J. Electrochem. Soc.* 158 (2011) A1067–A1070.
- [221] L.S. Plashnitsa, E. Kobayashi, Y. Noguchi, S. Okada, J.I. Yamaki, *J. Electrochem. Soc.* 157 (2010) A536–A543.
- [222] Z. Jian, Y. Sun, X. Ji, *Chem. Commun.* 51 (2015) 6381–6383.
- [223] W. Wang, B. Jiang, L. Hu, S. Jiao, *J. Mater. Chem.* 2 (2014) 1341–1345.
- [224] D. Wang, X. Bie, Q. Fu, D. Dixon, N. Bramnik, Y.S. Hu, F. Fauth, Y. Wei, H. Ehrenberg, G. Chen, F. Du, *Nat. Commun.* 8 (2017) 15888–15894.
- [225] C.W. Mason, F. Lange, *ECS Electrochem. Lett.* 4 (2015) A79–A82.
- [226] H. Wang, T. Zhang, C. Chen, M. Ling, Z. Lin, S. Zhang, F. Pan, C. Liang, *Nano Res.* 11 (2017) 490–498.
- [227] W. Gao, R. Zhan, M.K. Aslam, D. Liu, J. Jiang, M. Xu, *Energy Stor.* 1 (2019) 74–81.
- [228] H. Gao, J.B. Goodenough, *Angew. Chem. Int. Ed.* 55 (2016) 12768–12772.
- [229] T. Zhu, P. Hu, X. Wang, Z. Liu, W. Luo, K.A. Owusu, W. Cao, C. Shi, J. Li, L. Zhou, L. Mai, *Adv. Energy Mater.* 9 (2019) 1803436–1803441.
- [230] H. Gao, Y. Li, K. Park, J.B. Goodenough, *Chem. Mater.* 28 (2016) 6553–6559.
- [231] X. Liang, X. Ou, F. Zheng, Q. Pan, X. Xiong, R. Hu, C. Yang, M. Liu, *ACS Appl. Mater. Interfaces* 9 (2017) 13151–13162.
- [232] W. Ren, X. Yao, C. Niu, Z. Zheng, K. Zhao, Q. An, Q. Wei, M. Yan, L. Zhang, L. Mai, *Nano Energy* 28 (2016) 216–223.
- [233] Z. Yuan, L. Si, X. Zhu, *J. Mater. Chem.* 3 (2015) 23403–23411.
- [234] M. Huang, B. Xi, Z. Feng, J. Liu, J. Feng, Y. Qian, S. Xiong, *J. Mater. Chem.* 6 (2018) 16465–16474.
- [235] X. Hu, X. Sun, S.J. Yoo, B. Evanko, F. Fan, S. Cai, C. Zheng, W. Hu, G.D. Stucky, *Nano Energy* 56 (2019) 828–839.
- [236] J. Li, L. Han, D. Zhang, J. Li, T. Lu, X. Wang, L. Pan, *Inorg. Chem. Front.* 6 (2019) 2104–2111.
- [237] T. Yang, T. Qian, M. Wang, X. Shen, N. Xu, Z. Sun, C. Yan, *Adv. Mater.* 28 (2016) 539–545.
- [238] L. Gao, J. Ma, S. Li, D. Liu, D. Xu, J. Cai, L. Chen, J. Xie, L. Zhang, *Nanoscale* 11 (2019) 12626–12636.
- [239] Z. Zhu, F. Cheng, Z. Hu, Z. Niu, J. Chen, *J. Power Sources* 293 (2015) 626–634.
- [240] X.X. Cao, A.Q. Pan, S.N. Liu, J. Zhou, S.T. Li, G.Z. Cao, J. Liu, S.Q. Liang, *Adv. Energy Mater.* 7 (2017) 1700797–1700806.
- [241] P. Han, X. Han, J. Yao, Z. Liu, X. Cao, G. Cui, *Electrochem. Commun.* 61 (2015) 84–88.
- [242] H. Wang, P. Hu, J. Yang, G. Gong, L. Guo, X. Chen, *Adv. Mater.* 27 (2015) 2348–2354.
- [243] N. Wang, Z. Bai, Y. Qian, J. Yang, *Adv. Mater.* 28 (2016) 4126–4133.
- [244] X.M. Pham, D.T. Ngo, H.T.T. Le, P.N. Didwala, R. Verma, C.W. Min, C.N. Park, C.J. Park, *Nanoscale* 10 (2018) 19399–19408.
- [245] F. Wan, J.Z. Guo, X.H. Zhang, J.P. Zhang, H.Z. Sun, Q. Yan, D.X. Han, L. Niu, X.L. Wu, *ACS Appl. Mater. Interfaces* 8 (2016) 7790–7799.
- [246] W. Zhang, Y. Liu, C. Chen, Z. Li, Y. Huang, X. Hu, *Small* 11 (2015) 3822–3829.
- [247] J. Zhang, Y. Fang, L. Xiao, J. Qian, Y. Cao, X. Ai, H. Yang, *ACS Appl. Mater. Interfaces* 9 (2017) 7177–7184.
- [248] M. Song, C. Wang, D. Du, F. Li, J. Chen, *Sci. China Chem.* 62 (2019) 616–621.
- [249] J. Tang, S. Ni, Q. Chen, W. Han, X. Yang, L. Zhang, *Mater. Lett.* 195 (2017) 127–130.
- [250] W. Ma, J. Wang, H. Gao, J. Niu, F. Luo, Z. Peng, Z. Zhang, *Energy Stor. Mater.* 13 (2018) 247–256.
- [251] P.R. Kumar, Y.H. Jung, K.K. Bharathi, C.H. Lim, D.K. Kim, *Electrochim. Acta* 146 (2014) 503–510.
- [252] S. Hariharan, K. Saravanan, P. Balaya, *Electrochim. Commun.* 31 (2013) 5–9.
- [253] M.C. Lopez, M.J. Aragon, G.F. Ortiz, P. Lavela, R. Alcantara, J.L. Tirado, *Chemistry* 21 (2015) 14879–14885.
- [254] A. Moretti, M. Secchiarioli, D. Buchholz, G. Giuli, R. Marassi, S. Passerini, *J. Electrochem. Soc.* 162 (2015) A2723–A2728.

- [255] S. Rubio, R.R. Maça, M.J. Aragón, M. Cabello, M. Castillo-Rodríguez, P. Lavela, J.L. Tirado, V. Etacheri, G.F. Ortiz, *J. Power Sources* 432 (2019) 82–91.
- [256] H. Yang, R. Xu, Y. Gong, Y. Yao, L. Gu, Y. Yu, *Nano Energy* 48 (2018) 448–455.
- [257] L. Wang, X. Bi, S. Yang, *Adv. Mater.* 28 (2016) 7672–7679.
- [258] X. Zhao, H.-E. Wang, R.C. Massé, J. Cao, J. Sui, J. Li, W. Cai, G. Cao, *J. Mater. Chem. 5* (2017) 7394–7402.
- [259] X. Rui, W. Sun, C. Wu, Y. Yu, Q. Yan, *Adv. Mater.* 27 (2015) 6670–6676.
- [260] R. Sun, Q. Wei, J. Sheng, C. Shi, Q. An, S. Liu, L. Mai, *Nano Energy* 35 (2017) 396–404.
- [261] S. Peng, X. Han, L. Li, Z. Zhu, F. Cheng, M. Srinivansan, S. Adams, S. Ramakrishna, *Small* 12 (2016) 1359–1368.
- [262] L. Zhou, K. Zhang, J. Sheng, Q. An, Z. Tao, Y.-M. Kang, J. Chen, L. Mai, *Nano Energy* 35 (2017) 281–289.
- [263] Q. Chen, S. Ni, J. Tang, T. Li, T. Kang, X. Yang, *Mater. Lett.* 213 (2018) 193–196.
- [264] W. Sun, X. Rui, D. Zhang, Y. Jiang, Z. Sun, H. Liu, S. Dou, *J. Power Sources* 309 (2016) 135–140.
- [265] W.P. Sun, X.H. Rui, D. Yang, Z.Q. Sun, B. Li, W.Y. Zhang, Y. Zong, S. Madhavi, S.X. Dou, Q.Y. Yan, *ACS Nano* 9 (2015) 11371–11381.
- [266] K. Zhang, M. Park, L. Zhou, G.H. Lee, J. Shin, Z. Hu, S.L. Chou, J. Chen, Y.M. Kang, *Angew. Chem. Int. Ed.* 55 (2016) 12822–12826.
- [267] H. Ye, L. Wang, S. Deng, X. Zeng, K. Nie, P.N. Duchesne, B. Wang, S. Liu, J. Zhou, F. Zhao, N. Han, P. Zhang, J. Zhong, X. Sun, Y. Li, Y. Li, J. Lu, *Adv. Energy Mater.* 7 (2017) 1601602–1601610.
- [268] S. Chen, J. Zhao, Y. Pang, S. Ding, *Nanotechnology* 30 (2019) 425402–425411.
- [269] X. Cao, A. Pan, B. Yin, G. Fang, Y. Wang, X. Kong, T. Zhu, J. Zhou, G. Cao, S. Liang, *Nano Energy* 60 (2019) 312–323.
- [270] Z.-H. Zhao, X.-D. Hu, H. Wang, M.-Y. Ye, Z.-Y. Sang, H.-M. Ji, X.-L. Li, Y. Dai, *Nano Energy* 48 (2018) 526–535.
- [271] F. Niu, J. Yang, N. Wang, D. Zhang, W. Fan, J. Yang, Y. Qian, *Adv. Funct. Mater.* 27 (2017) 1700522–1700532.
- [272] K. Zhang, Z. Hu, X. Liu, Z. Tao, J. Chen, *Adv. Mater.* 27 (2015) 3305–3309.
- [273] K. Zhang, M. Park, L. Zhou, G.-H. Lee, W. Li, Y.-M. Kang, J. Chen, *Adv. Funct. Mater.* 26 (2016) 6728–6735.
- [274] S. Lu, T. Zhu, H. Wu, Y. Wang, J. Li, A. Abdelkader, K. Xi, W. Wang, Y. Li, S. Ding, G. Gao, R.V. Kumar, *Nano Energy* 59 (2019) 762–772.
- [275] L. Wang, X. Zhao, S. Dai, Y. Shen, M. Wang, *Electrochim. Acta* 314 (2019) 142–150.
- [276] W. Li, L. Ke, Y. Wei, S. Guo, L. Gan, H. Li, T. Zhai, H. Zhou, *J. Mater. Chem. 5* (2017) 4413–4420.
- [277] M. Fan, Y. Chen, Y. Xie, T. Yang, X. Shen, N. Xu, H. Yu, C. Yan, *Adv. Funct. Mater.* 26 (2016) 5019–5027.
- [278] J. Sun, C. Guo, Y. Cai, J. Li, X. Sun, W. Shi, S. Ai, C. Chen, F. Jiang, *Electrochim. Acta* 309 (2019) 18–24.
- [279] X. Yao, Z. Zhu, Q. Li, X. Wang, X. Xu, J. Meng, W. Ren, X. Zhang, Y. Huang, L. Mai, *ACS Appl. Mater. Interfaces* 10 (2018) 10022–10028.
- [280] G. Yan, S. Mariyappan, G. Rousse, Q. Jacquet, M. Deschamps, R. David, B. Mirvieux, J.W. Freeland, J.M. Tarascon, *Nat. Commun.* 10 (2019) 585–596.
- [281] Q. Wang, X. Zhu, Y. Liu, Y. Fang, X. Zhou, J. Bao, *Carbon* 127 (2018) 658–666.
- [282] Y. Lu, N. Dimov, S. Okada, T. Bui, *Energies* 11 (2018) 1614–1623.
- [283] Y.C. Lu, C. Ma, J. Alvarado, N. Dimov, Y.S. Meng, S. Okada, *J. Mater. Chem. 3* (2015) 16971–16977.
- [284] Y.-Y. Wang, H. Fan, B.-H. Hou, X.-H. Rui, Q.-L. Ning, Z. Cui, J.-Z. Guo, Y. Yang, X.-L. Wu, *J. Mater. Chem. 6* (2018) 22966–22975.
- [285] Y. Liu, N. Zhang, X. Liu, C. Chen, L.-Z. Fan, L. Jiao, *Energy Stor. Mater.* 9 (2017) 170–178.
- [286] V. Medabalmi, N. Kuanr, K. Ramanujam, *J. Electrochem. Soc.* 165 (2018) A175–A180.
- [287] J. Peng, J. Wang, H. Yi, W. Hu, Y. Yu, J. Yin, Y. Shen, Y. Liu, J. Luo, Y. Xu, P. Wei, Y. Li, Y. Jin, Y. Ding, L. Miao, J. Jiang, J. Han, Y. Huang, *Adv. Energy Mater.* 8 (2018) 1702856–1702864.
- [288] P. Wei, Y. Liu, Y. Su, L. Miao, Y. Huang, Y. Liu, Y. Qiu, Y. Li, X. Zhang, Y. Xu, X. Sun, C. Fang, Q. Li, J. Han, Y. Huang, *ACS Appl. Mater. Interfaces* 11 (2019) 3116–3124.
- [289] F. Chen, Y. Huang, D. Kong, M. Ding, S. Huang, H.Y. Yang, *FlatChem* 8 (2018) 9–16.
- [290] L. Wang, C. Mu, H. Li, F. Li, *Inorg. Chem. Front.* 5 (2018) 2522–2526.
- [291] Y. Wang, L. Mu, J. Liu, Z. Yang, X. Yu, L. Gu, Y.-S. Hu, H. Li, X.-Q. Yang, L. Chen, X. Huang, *Adv. Energy Mater.* 5 (2015) 1501005–1501012.
- [292] Y. Noguchi, E. Kobayashi, L.S. Plashnitsa, S. Okada, J.-i. Yamaki, *Electrochim. Acta* 101 (2013) 59–65.
- [293] F. Lalère, J.B. Leriche, M. County, S. Boulineau, V. Viallet, C. Masquelier, V. Seznec, *J. Power Sources* 247 (2014) 975–980.
- [294] P.N. Didwal, R. Verma, C.-W. Min, C.-J. Park, *J. Power Sources* 413 (2019) 1–10.
- [295] W. Duan, Z. Zhu, H. Li, Z. Hu, K. Zhang, F. Cheng, J. Chen, *J. Mater. Chem. 2* (2014) 8668–8675.
- [296] Q. Zhu, B. Nan, Y. Shi, Y. Zhu, S. Wu, L. He, Y. Deng, L. Wang, Q. Chen, Z. Lu, *J. Solid State Electrochem.* 21 (2017) 2985–2995.
- [297] C. Zhu, P. Kopold, P.A. van Aken, J. Maier, Y. Yu, *Adv. Mater.* 28 (2016) 2409–2416.
- [298] Y. Zhang, H. Zhao, Y. Du, *J. Mater. Chem. 4* (2016) 7155–7159.
- [299] W. Ren, Z. Zheng, C. Xu, C. Niu, Q. Wei, Q. An, K. Zhao, M. Yan, M. Qin, L. Mai, *Nano Energy* 25 (2016) 145–153.
- [300] A. Rudola, D. Aurbach, P. Balaya, *Electrochim. Commun.* 46 (2014) 56–59.
- [301] D. Guo, J. Qin, Z. Yin, J. Bai, Y.-K. Sun, M. Cao, *Nano Energy* 45 (2018) 136–147.
- [302] S. Yu, Z. Liu, H. Tempel, H. Kunzl, R.-A. Eichel, *J. Mater. Chem. 6* (2018) 18304–18317.
- [303] S. Liu, L. Wang, J. Liu, M. Zhou, Q. Nian, Y. Feng, Z. Tao, L. Shao, *J. Mater. Chem. 7* (2019) 248–256.
- [304] Y. Fang, L. Xiao, J. Qian, Y. Cao, X. Ai, Y. Huang, H. Yang, *Adv. Energy Mater.* 6 (2016) 1502197–1502204.
- [305] Q. Liu, X. Meng, Z. Wei, D. Wang, Y. Gao, Y. Wei, F. Du, G. Chen, *ACS Appl. Mater. Interfaces* 8 (2016) 31709–31715.
- [306] P.R. Kumar, Y.H. Jung, J.E. Wang, D.K. Kim, *J. Power Sources* 324 (2016) 421–427.
- [307] W. Song, X. Ji, Z. Wu, Y. Zhu, F. Li, Y. Yao, C.E. Banks, *RSC Adv.* 4 (2014) 11375–11383.
- [308] Y.-Y. Wang, B.-H. Hou, J.-Z. Guo, Q.-L. Ning, W.-L. Pang, J. Wang, C.-L. Lü, X.-L. Wu, *Adv. Energy Mater.* 8 (2018) 1703252–1703259.
- [309] S. Li, Y. Dong, L. Xu, X. Xu, L. He, L. Mai, *Adv. Mater.* 26 (2014) 3545–3553.
- [310] L. Zhao, H. Zhao, Z. Du, J. Wang, X. Long, Z. Li, K. Swierczek, *J. Mater. Chem. 7* (2019) 9807–9814.
- [311] A. Firouzi, R. Qiao, S. Motallebi, C.W. Valencia, H.S. Israel, M. Fujimoto, L.A. Wray, Y.D. Chuang, W. Yang, C.D. Wessells, *Nat. Commun.* 9 (2018) 861–870.
- [312] Y. Huang, M. Xie, Z. Wang, Y. Jiang, Q. Huang, X. Bai, L. Li, F. Wu, R. Chen, *Nano Energy* 60 (2019) 294–304.
- [313] D.J. Kim, Y.H. Jung, K.K. Bharathi, S.H. Je, D.K. Kim, A. Coskun, J.W. Choi, *Adv. Energy Mater.* 4 (2014) 1400133–1400139.
- [314] W. Ren, Z. Zhu, M. Qin, S. Chen, X. Yao, Q. Li, X. Xu, Q. Wei, L. Mai, C. Zhao, *Adv. Funct. Mater.* 29 (2019) 1806405–1806414.
- [315] X. Wu, Y. Cao, X. Ai, J. Qian, H. Yang, *Electrochim. Commun.* 31 (2013) 145–148.
- [316] D. Yang, J. Xu, X.Z. Liao, Y.S. He, H. Liu, Z.F. Ma, *Chem. Commun.* 50 (2014) 13377–13380.
- [317] H. Ye, Y. Wang, F. Zhao, W. Huang, N. Han, J. Zhou, M. Zeng, Y. Li, *J. Mater. Chem. 4* (2016) 1754–1761.
- [318] Y. Li, Y.-S. Hu, H. Li, L. Chen, X. Huang, J. Mater. Chem. 4 (2016) 96–104.
- [319] Y. Li, Y.-S. Hu, X. Qi, X. Rong, H. Li, X. Huang, L. Chen, *Energy Stor. Mater.* 5 (2016) 191–197.
- [320] Y. Li, L. Mu, Y.-S. Hu, H. Li, L. Chen, X. Huang, *Energy Stor. Mater.* 2 (2016) 139–145.
- [321] Y. Li, S. Xu, X. Wu, J. Yu, Y. Wang, Y.-S. Hu, H. Li, L. Chen, X. Huang, *J. Mater. Chem. 3* (2015) 71–77.
- [322] Y. Liu, Q. Shen, X. Zhao, J. Zhang, X. Liu, T. Wang, N. Zhang, L. Jiao, J. Chen, L.Z. Fan, *Adv. Funct. Mater.* (2019) 1907837–1907847.
- [323] L. Mu, S. Xu, Y. Li, Y.S. Hu, H. Li, L. Chen, X. Huang, *Adv. Mater.* 27 (2015) 6928–6933.
- [324] Y. Wang, R. Xiao, Y.S. Hu, M. Avdeev, L. Chen, *Nat. Commun.* 6 (2015) 6954–6962.
- [325] S. Xu, Y. Wang, L. Ben, Y. Lyu, N. Song, Z. Yang, Y. Li, L. Mu, H.-T. Yang, L. Gu, Y.-S. Hu, H. Li, Z.-H. Cheng, L. Chen, X. Huang, *Adv. Energy Mater.* 5 (2015) 1501156–1501164.
- [326] D.Y. Yu, P.V. Prikhodchenko, C.W. Mason, S.K. Batabyal, J. Gun, S. Sladkevich, A.G. Medvedev, O. Lev, *Nat. Commun.* 4 (2013) 2922–2928.